Femtosecond Sources at 1.5 microns and Their Application for Time-Resolved Spectroscopic Studies of Semiconductor Devices

by

Gadi Lenz

B.Sc., Technion - Israel Institute of Technology
(1988)

M.Sc., Technion - Israel Institute of Technology
(1990)

Submitted to the
Department of Electrical Engineering and Computer Science
in partial fulfillment of the
requirements for the degree of

Doctor of Philosophy

at the

Massachusetts Institute of Technology

December 1995

Signature of Author _

Department of Electrical Engineering and Computer Science
December 1, 1995

Certified by ___

Erich P. Ippen
Thesis Advisor

Accepted by ___

ederic R. Morgenthaler
e on Graduate Students

Femtosecond Sources at 1.5 microns and Their Application for Time-Resolved Spectroscopic Studies of Semiconductor Devices

by

Gadi Lenz

Abstract

Optical communication systems require optoelectronic devices and components that operate at a wavelength of 1.5 µm, where standard optical fibers have a minimum transmission loss. Investigating the performance of these devices and understanding the underlying physics requires good sources at this wavelength. In particular, the investigation of their ultrafast nonlinear response, which will ultimately limit the switching speed and modulation characteristics, requires good femtosecond sources at 1.5 µm.

A broadband femtosecond source is ideal for variable wavelength pump-probe experiments, which are the standard tool for time-resolved spectroscopy. To this end, a stretched-pulse additive pulse modelocked erbium-doped fiber ring laser was used as a seeding laser for a solid-state color center amplifier, which was pumped by a 1 kHz Q-switched Nd:YAG laser. The seeding pulse train was matched in repetition rate and synchronized to the pump laser. The seeding pulse was passed twice through the gain medium to be amplified by a factor of ~ 10000. The resulting 10 µJ pulses were recompressed to 250 fs duration and focused onto a nonlinear material, yielding an extremely broadband femtosecond continuum. This femtosecond continuum was then passed through a spectral slicer to demonstrate variable-bandwidth tunable femtosecond pulses.

In a separate experiment, an additive pulse modelocked color center laser was used to investigate the nonlinear femtosecond dynamics of a polarization insensitive semiconductor optical amplifier. By mixing quantum wells with compressive and tensile strain, both TE- and TM-polarized light are equally amplified. This useful device has been introduced as an integrated optics device to act as an amplifier independent of the polarization state of its input. Although this device has isotropic gain by design, it showed a nonlinear dynamic anisotropy. A heterodyne pump-probe technique was used to resolve the polarization dependence of the dynamic nonlinear response of the gain as well as the index. The cooling time of the carriers following optical excitation showed a dependence on the pump polarization. When the pump and probe are both TE-polarized the cooling time is ~ 900 fs, but for all other TE and TM combinations for pump and probe the cooling time is only ~ 700 fs. Calculations showed that in this experiment the measurement is sensitive mainly to hole dynamics. Further band structure calculations show that the states of interest are heavy hole states with light effective mass in the compressive strain well, and light hole states with a heavy effective mass in the tensile strain well. The different cooling time is attributed to this mass difference. The anisotropy is attributed to the polarization dependence of the heating mechanism, dominated by intervalence band absorption. To further investigate the dynamic anisotropy, a technique was devised to measure the induced anisotropy directly. This

2

measurement contains both the induced birefringence and induced dichroism. The measurement results showed a new ~ 7 ps time constant, not apparent in the previous measurements. This longer time constant is attributed to interwell coupling or transport. A residual long-time anisotropy in the measurement, indicates a polarization dependence of the CW saturation of the device.

Thesis Advisor: Erich P. Ippen

Title: Elihu Thomson Professor of Electrical Engineering

To my parents who started me on this path

and to my wife and kids who saw me through it

Acknowledgments

First, I would like to thank my advisor Professor Erich Ippen, for his guidance, patience and support for the past five years. I have learned many invaluable lessons from him and have greatly benefited from his many physical insights. I would also like to thank Professor Haus for many suggestions and advice over the years.

Katie Hall was my mentor when I started out, she showed me the ropes and taught me a lot about experimental work in the lab. She put up with my listening to WZLX and I put up with her neuroses (not all blue glowing crystals are radioactive and clean rooms are in general....clean). Charlie Hultgren deserves special thanks for keeping me laughing and showing me his happy-sad face and a lot of advice on pump-probe lore. Thanks to Keren Bergman, the eternal cheerful person, for all her help over the years. Dave Dougherty and Siegfried Fleischer, my partners in crime, have shared many a coffee with me...I will miss the daily ritual. I have learned a great deal from them through hours of discussions and arguments. A special thanks goes to Dave for exposing me to the John Spencer Blues Explosion. I have enjoyed working with Kohichi Tamura and Lynn Nelson in the lab, they taught me all about fiber lasers. Thanks Lynn for suffering through my Poincaré sphere ramblings. It was a pleasure working together with John Moores and Farzana Khatri, much of what I know about APM comes from them. Thanks to Steve Cheng for introducing me to the MIT TKD club and actually dragging me there when I was being lazy. Nick Ulman, a recent Led Zep convert and honorary coffee club member - thanks for the boring Grateful Dead anecdotes. Kazunori Naganuma, scientist extraordinaire, has taught me much about femtosecond optics and Japanese culture. Antonio Mecozzi and Franz Kärtner were good friends and great partners in discussions about quantum mechanics, Schrödinger's cat and the meaning of life. Jérôme Paye was a visiting a scientist who worked with me for a year and introduced me to the problem of pulse measurement and taught me about details in pulse amplification and continuum generation. Many thanks to Brett Bouma for many random helpful suggestions and advice. Ali Darwish shared the lab with me for a long time - thanks for giving me lab time when I needed it and thanks for the many souvenirs from Egypt. Thanks to all my other Optics Group colleagues: David Jones, Dr. Brent Little, Dr. Shu Namiki, Jerry Chen, Luc Boivin, Gary Tearney, Igor Bilinsky, Boris Golubovic, Steve Boppart, Jay Damask, Costas Tziligakis, William Wong, Erik Thoen and Matthew Grein. Cindy Kopf, super secretary, thanks for those great New

Contents

3 Nonlinear dynamic anisotropy in 1.5 µm semiconductor optical amplifiers 51

List of Figures

12

List of Tables

13

Chapter 1

Introduction

1.1 The importance of 1.5 μm radiation

Glass fiber has become the enabling technology for optical communication. Standard fiber has minimum loss at a wavelength of 1.55 μm [1]. Standard glass fiber also has a minimum of dispersion at a wavelength 1.3 μm, however by optimizing the index profile, the material dispersion may be balanced by the waveguide dispersion to achieve zero dispersion at 1.55 μm [1]. For these reasons the wavelength region of 1.55 μm is of great importance and interest.

Since most of optical communication will be based in the 1.55 μm spectral region, the building blocks of this optical network must be well understood. Components such as semiconductor lasers, amplifiers and detectors as well as integrated optics devices (e.g., switches, filters, routers, etc.) must be investigated. In fact the fiber itself, being the transmission medium, has to be studied. To study and understand the physics of all of these devices and components and design new ones, necessitates 1.55 μm sources and various spectroscopic tools.

1.2 Why do we need femtosecond sources?

1.2.1 Spectroscopic tool

One of the main requirements of communication networks is speed, the transmission of information in as little time as possible. The response of the network components to high-speed modulation must be characterized. Modelocked laser sources with picosecond and sub-picosecond duration pulses are therefore ideally suited for probing these characteristics.

Femtosecond sources may be used as spectroscopic tools to resolve the ultrafast response of different materials and devices. Techniques such as pump-probe experiments, let us excite a material with a strong pump pulse and probe its response with a weak probe

pulse, which is delayed with respect to the pump pulse. From this we can learn about the high-speed dynamics and the underlying physics of these materials. These in turn, will tell us the fundamental limits to high-speed modulation and maybe suggest new ways to overcome these limits.

1.2.2 Nonlinear optics

Another use of femtosecond pulses is in applications that require high peak powers. In particular all nonlinear optical techniques rely on high peak powers [2]. The nonlinear interaction scales as some power of the intensity (depending on the particular nonlinearity), so that higher peak intensities make the observation of these effects easier. By going from a given continuous wave (CW) average power to a pulsed laser with the same average power, the peak power increase is approximately the inverse of the product of the pulsewidth and the repetition rate. Shorter pulses and lower repetition rates result in higher peak powers.

An inherent feature of nonlinear optical interactions is the generation of new frequencies [2]. Since the generated new fields are proportional to products of the input fields, they will contain sums and differences of the input frequencies. This is of interest to optical communication employing wavelength division multiplexing (WDM), where frequency shifters are needed [3]. This is also of interest to time-resolved spectroscopy in techniques such as continuum generation (extreme spectral broadening through self phase modulation (SPM)), which may result in a femtosecond white light source [4].

1.3 The aim of this thesis

1.3.1 Development of new 1.5 μm femtosecond sources

Because of the importance of femtosecond studies at 1.55 μm, as outlined above, good reliable femtosecond sources operating at this wavelength have to be available. Until very recently the only available sources were additive pulse modelocked (APM) color center lasers, in particular the $KCl:Tl^+$ and the $NaCl:OH^-$ [5] [6]. More recently a few alternative sources were developed - the erbium fiber laser [7], the $Cr^{4+}:YAG$ [8] and the femtosecond optical parametric oscillators (OPO's) [9].

In order to use these sources effectively in experiments, their characteristics and performance have to be evaluated. Characteristics such as pulse duration, optical spectrum, stability, starting conditions, amplitude and phase noise (timing jitter), must be investi-

gated. In this thesis one specific laser systems will be studied: A diode-pumped mode-locked erbium fiber laser.

Since erbium-doped fibers were shown to be an excellent gain medium at the 1.55 μm spectral region [10] [11], there has been great interest in using them as lasers, and more importantly for optical communication purposes, as amplifiers. More recently modelocking these fiber lasers became of interest, and several configurations were investigated [7] [12] [13]. One of the best performers in terms of output power and pulse duration is the stretched pulse APM (SP-APM) erbium-doped fiber ring laser [14]. This laser was limited in terms of output power and amplitude noise mainly by the pump source - an argon ion pumped Ti:Sapphire laser. The commercial availability of master oscillator power amplifier (MOPA) diodes operating at 980 nm (one of the main absorption bands of erbium) [15] [16], made it possible to replace the complex pumping system with a much simpler one. The high power, single longitudinal mode operation and low noise of these MOPA's made them an ideal pump source for the fiber laser.

In section 2.1 the performance of these laser systems in terms of their pulse duration and chirp, output power, and amplitude noise, will be described. Their excellent performance makes them an ideal source for seeding a solid-state amplifier. Their low-noise characteristics should also enhance the signal-to-noise ratio in experiments such as pump-probe, resulting in higher sensitivity (relative to the color center lasers, for example).

1.3.2 Amplification 1.5 μm femtosecond pulses and continuum generation

As mentioned earlier (section 1.2.2) nonlinear optics applications require high peak power, in particular continuum generation requires high peak intensities to spectrally broaden the input pulse. Thus, a very broad band femtosecond source can be produced, and subsequent spectral filtering applied to yield a tunable femtosecond source. This is important for pump-probe experiments where the pump and probe need to be at the different wavelengths, or for probing very broad distributions with the broad spectrum.

To create such a source at 1.55 μm requires an amplifier and hence a gain medium, which has its peak around this wavelength. One of the obvious choices for a gain medium would be a color center crystal. In section 2.2 an amplifier system based on the KCl:Tl$^+$ color center crystal will be investigated. The seeding laser is the modelocked erbium doped fiber laser discussed earlier (section 1.3.1). The output pulse train from this laser is passed through a pulse selector to match the 1 kHz repetition rate of the Q-switched Nd:YAG, which pumps the color center amplifier crystal. The selected pulses are synchronized with

16

the pump pulses and experience a single pass gain of ~1000. After 2 passes through the amplifier the pulse energy is ~10 μJ for a net energy gain of ~10000. Compression of these pulses to ~250 fs results in peak powers of ~10^7 W, and by focusing to spot sizes of a few tens of microns we can get peak intensities on the order of 10^{11}-10^{12} W/cm^2. With these peak intensities continuum may be generated, and in sections 2.3.6-2.3.9 a few different materials will be investigated in terms of their ability to generate wide spectrum. Spectral slicing of this broad continuum will also be demonstrated, to make this an excellent spectroscopic tool.

1.3.3 Investigation of the ultrafast response of semiconductor devices operating at 1.5 μm

As was discussed earlier (section 1.1), optoelectronic devices operating at 1.55 μm are of great interest for optical communication, and therefore their characteristics, physics and performance have to be investigated and quantified. In particular, for applications such as high speed modulation and all optical switching, the ultrafast response of these devices has to be investigated. This thesis will concentrate on the investigation of one specific device, namely the polarization insensitive semiconductor optical amplifier (PI-SOA).

PI-SOA's have been recently introduced as amplifiers of optical signals coming from optical fibers, where typically the state of polarization is arbitrary. By alternating compressive and tensile strained quantum wells in the active region of the device, the gain for TE polarized light and TM polarized light may be tailored to be approximately equal. This is a result of different selection rules for conduction band to heavy hole transitions (in the compressive well) and conduction band to light hole transitions (in the tensile well, where the light hole band is above the heavy hole band because of the tensile strain). These devices have been demonstrated at different wavelengths, and show equal gain for the TE and TM polarized light to within 1-2 dB. They will be described in more detail in chapter 3.

Although the linear gain response has been tailored to be isotropic, the nonlinear response may show anisotropy. Chapter 3 will deal with the investigation of this nonlinear anisotropy in the gain as well as in the index response. The experimental technique used for this investigation is called heterodyne pump-probe and allows polarization-resolved as well as time-resolved measurement of the induced gain and phase change in these devices. A novel variation in this technique allows the direct measurement of the induced anisotropy, by projecting the induced polarization changes on the heterodyne reference beam. Theoretical modeling of these devices shows that the measurement is sensitive primarily to hole dynamics in the valence bands. The anisotropy in the response is explained mainly by

the very different hole masses in the different wells (a consequence of strain induced band warping). The effect of interwell coupling or transport is also investigated.

1.3.4 Possible designs of semiconductor microstructures to achieve intersubband transitions at 1.5 μm

The appendix to this thesis (chapter 5) will discuss several possible microstructures that will make 1.55 μm intersubband transitions possible. This means a large potential discontinuity in the conduction or the valence band, on the order of 1 eV. Intersubband transitions are desirable because of their large oscillator strength (especially on the $1 \rightarrow 2$ transition) and fast relaxation time (on the order of 1 ps). This means a large, fast nonlinearity, which is ideal for all optical switching. Three different structures will be examined and compared.

Chapter 2

Development of new 1.5 μm femtosecond sources

This chapter will describe a new high-power femtosecond source operating at 1.5 μm, based on a diode-pumped fiber laser oscillator followed by a color center amplifier. The seeding laser is a modelocked fiber laser pumped by a high-power diode and is shown to be an excellent source for amplification. Section 2.1 will describe the characteristics of this source. The pulses from the fiber laser are amplified in a KCl:Tl$^+$ color center pumped by a 1 kHz Q-switched Nd:YAG laser. The pulse energy is amplified by a factor of ~ 10^4 in only 2 passes through the amplifier. The resulting ~ 10 μJ pulses are then compressed to ~ 250 fs. This peak power, the excellent beam profile of the amplified pulse train and the high stability of the seeding laser, are ideal for continuum generation. Sections 0 through 2.2.9 describe the investigation of a variety of materials for continuum generation. Finally, section 2.2.10 describes spectral slicing of the generated continuum to demonstrate that this is a tunable femtosecond source, making it an extremely useful spectroscopic tool for the 1.5 μm wavelength range.

2.1 Erbium doped fiber lasers

Doping fibers with rare earth atoms (such as erbium, thulium, etc.) allows amplification of optical signals, when pumped with the appropriate wavelength. The recent maturity of this technology, in particular the erbium-doped fiber, has given rise to a new type of amplifier and laser at 1.5 μm. When pumped at 980 nm or 1480 nm, the erbium-doped fiber will supply gain in a 40 nm band centered at 1530 nm. These fibers may be diode-pumped to yield very compact amplifier and laser systems, which is particularly attractive for repeaters in optical communication systems. Erbium-doped fiber lasers have been demonstrated in linear cavity as well as ring cavity configurations. Recent efforts in modelocking

these fiber lasers have resulted in a variety of techniques, and have yielded sub-picosecond pulses.

2.1.1 The MOPA-pumped stretched pulse APM erbium doped fiber laser

Typically, passively modelocked fiber lasers operate in the soliton regime and are therefore inherently limited to low output energies. The stretched-pulse APM technique was introduced in order to avoid some of the difficulties associated with the soliton systems. In this technique the fiber laser has erbium-doped sections and undoped sections. The doped sections have positive GVD and the undoped sections have negative GVD, such that the net GVD is approximately zero. In this system solitons are not supported and the associated difficulties are avoided. High-energy ultrashort pulses were demonstrated by using the so-called APM rejection port for output.

To date, the higher pumping powers required for such stretched-pulse operation has necessitated use of an Argon-laser-pumped Ti:Sapphire-laser pump, tuned to 980 nm. However, recent advances in high-power diode technology have resulted in a commercial Master Oscillator Power Amplifier (MOPA) diode operating at 980 nm with a CW output of ~1 W, making this a lower cost and more compact pump source for the fiber laser.

The MOPA diode is a small, commercially-available laser made by Spectra Diode Labs (SDL). It contains an oscillator section operating single longitudinal mode at 982 nm and a power amplifier section. It also contains bulk optics to correct the spatial mode and to produce a diffraction limited beam. The laser chip is mounted on a thermo-electric cooler, and may be temperature-tuned to some extent (0.07 nm/°C). In our experiments the temperature was kept fixed at 25 °C. The driver applied 200 mA to the oscillator section and 2500 mA to the amplifier section for a total output power ~ 900 mW of CW power. Typically ~70% of this power is coupled into a fiber and then coupled to the fiber laser by means of a WDM coupler. The fiber-coupled power is monitored with a 2% fiber coupler and a silicon photodiode.

2.1.2 High output power single-pulse operation

The design of the fiber laser was described in detail in [14] and the experimental setup is shown in Figure 2.1. When pumped with maximum power from the MOPA, it produces, from the high-power port, a modelocked train of pulses at 39.6 Mhz with up to 90 mW of average power, and an energy of 2.25 nJ per pulse. The threshold for modelocked operation is ~160 mW of pump power and the output average power at this pumping level is 20 mW. At an output power level of 90 mW the pulsewidth of the chirped output pulses
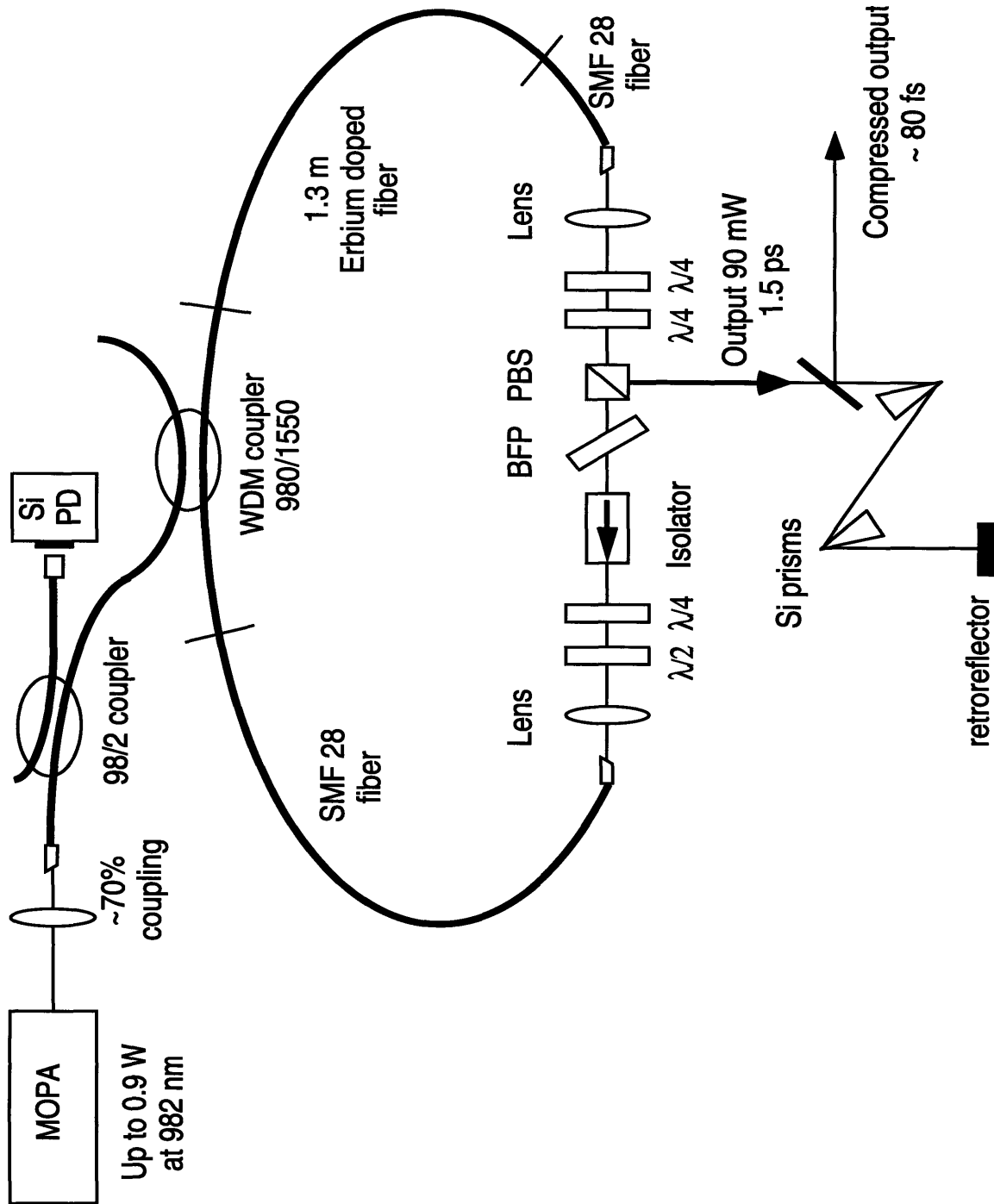
Figure 2.1:   Experimental setup of MOPA-pumped SP-APM erbium-doped fiber laser
with silicon prism pulse compressor

is typically 1-1.5 ps but the optical spectrum is 50-60 nm wide. At these pumping powers
the fiber laser self-starts easily and produces a

very stable output pulse train. The pulsewidth, spectrum and the average power are very reproducible.

Since this laser has operating regimes where multiple-pulsing is possible (trailing pulses separated by 20-40 ps from the main pulse are typical), single pulse operation had to be verified very carefully. This was accomplished using a 30 ps risetime detector with a sampling scope of 25 ps risetime, for long separations, and autocorrelation scans of up to 80 ps from the main pulse to cover the short temporal separations. The pulsing regime is
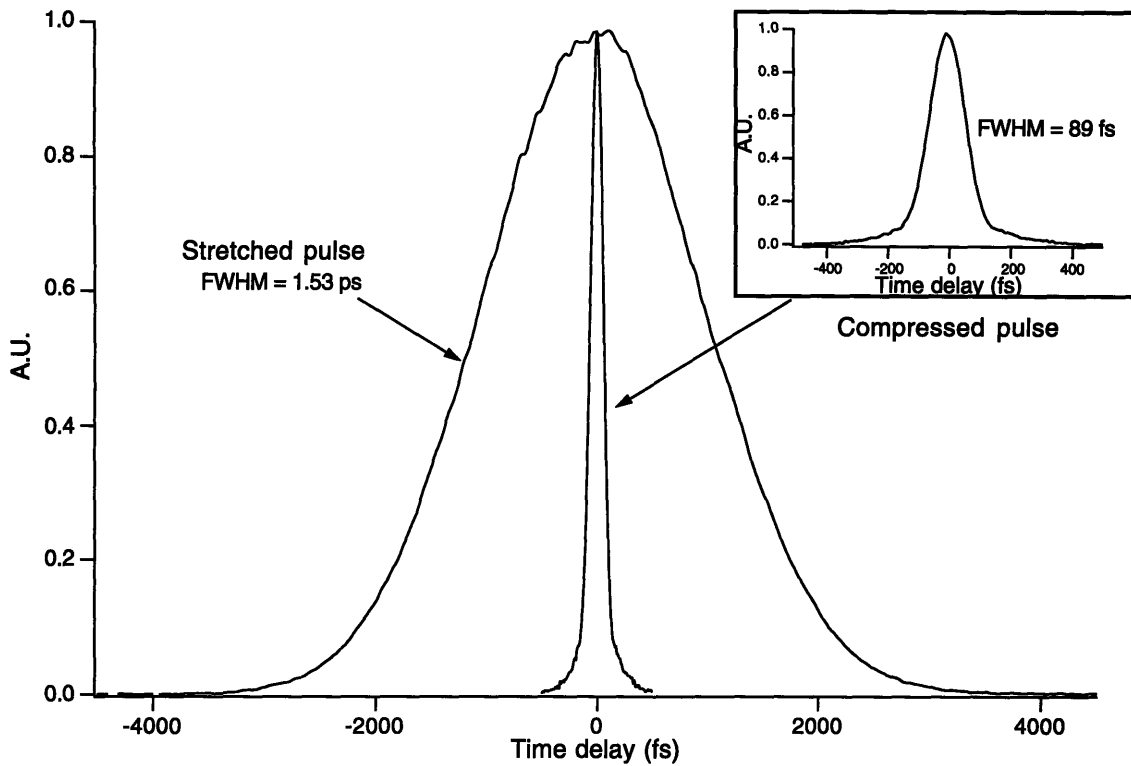
Figure 2.2: Intensity autocorrelations of the output of the SP-APM fiber laser from the high-energy port and after compression. The inset shows the compressed pulse in more detail.

highly dependent on the polarization state of the different waveplates in the laser cavity (which together with the polarizing beamsplitter are responsible for the modelocking action). An easy way of moving to single pulse operation is to observe the real-time autocorrelation of the compressed output pulses (to be discussed in the next section), since the peak power changes noticeably when all the available energy is put into one pulse. By adjusting the various waveplates and looking for an increase in the autocorrelation signal,

single pulse operation is easily achieved. Adjustment of the waveplates will sometimes lead to a modification in pulse chirp which in turn will lead to a change in compressed pulsewidth. This will affect the peak power and also show up as a change in the autocorrelation signal. This effect was typically less dramatic than the transition from multiple pulse to single pulse operation.

2.1.3 Dispersion compensation of the chirped output pulses

To compensate the large chirp on the pulses at the output we use a double pass silicon prism pair arrangement. Pulse durations as short as 81 fs have been observed, albeit with about 20-30% of the total energy remaining uncompressed in the wings. We use an adjustable slit between the first and second pass of the prism pair to perform spectral filtering [17]. The Brewster cut prisms are highly dispersive in the 1.5 μm spectral range (~1000
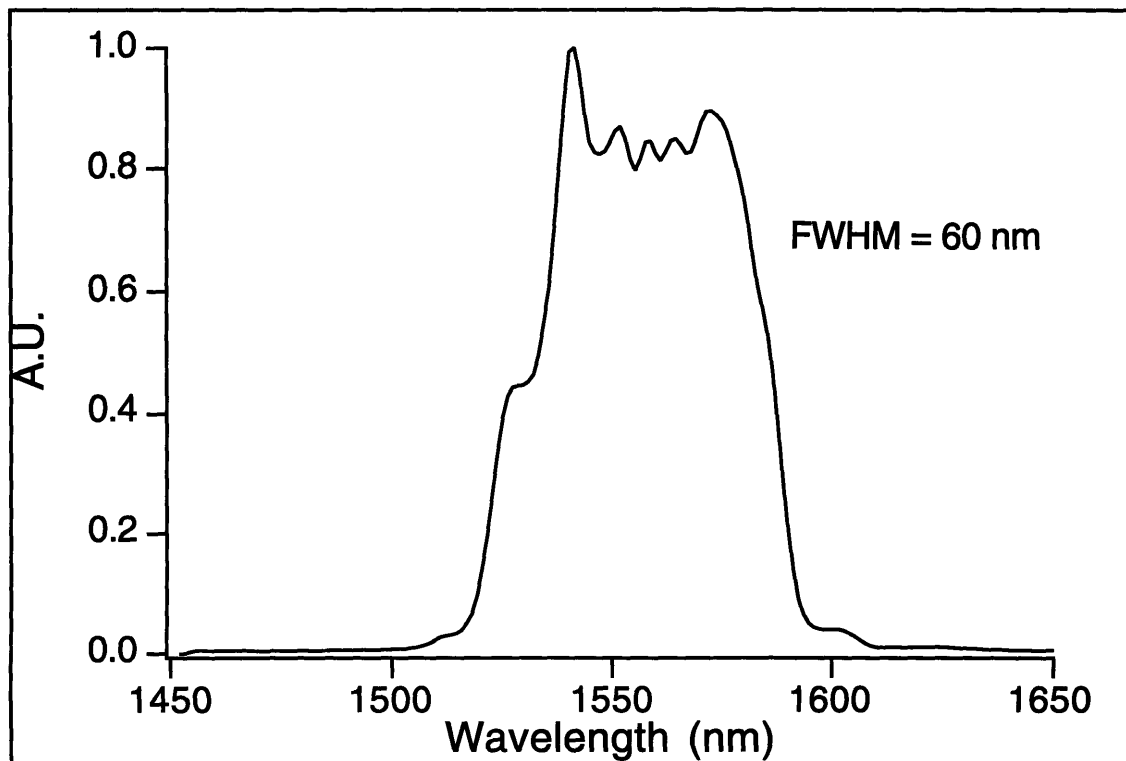
Figure 2.3:   Spectrum of SP-APM fiber laser output.

fs^2/mm) [18] and therefore a separation (apex to apex distance) of only about 18 cm is required, making the compressor stage very compact as well. The transmission losses through our prism compensator are ~30% and are due to losses in the prisms. Since the

beam is incident on the prisms at Brewster's angle, the residual reflection losses are negligible. High optical grade silicon should lead to a decrease of the transmission losses.

Figure 2.2 shows the highly chirped output pulse from the high-energy port of the laser and the pulse after compression. The inset in Figure 2.2 shows the compressed pulse in more detail. The 89 fs pulse shown represents some compromise between minimum pulsewidth and minimum wing energy. For this case about 10% of the pulse energy was filtered out spectrally. Figure 2.3 shows the corresponding optical spectrum with a width of almost 60 nm yielding a time-bandwidth product of 0.72 for 90 fs pulses assuming a sech profile. This indicates that some residual higher order chirp is present on the laser output and is not compensated by the prisms. In this context, we note that, with the ~ 1000
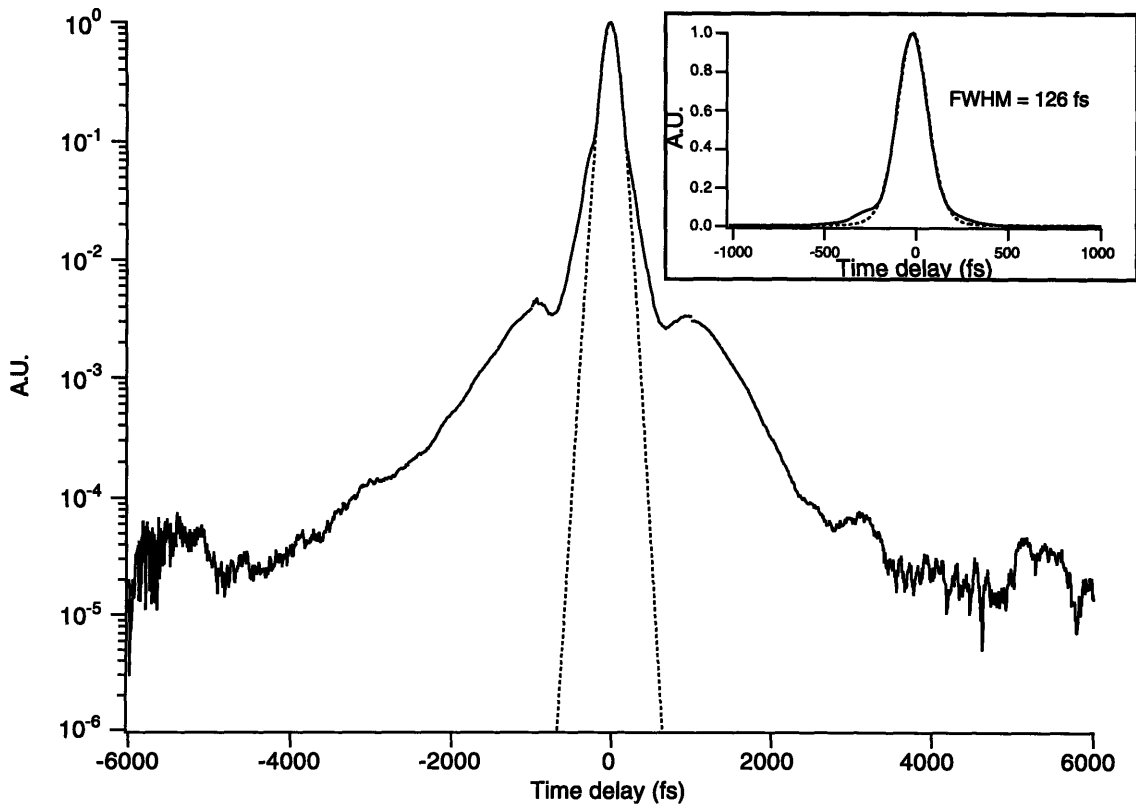
Figure 2.4:   High dynamic range intensity autocorrelation of compressed SP-APM fiber laser output. The inset shows the autocorrelation on a linear scale. The dashed line is a fit to the intensity autocorrelation of an ideal sech pulse.

fs^3/mm third order dispersion of silicon (about 10 times more than standard fiber) and an 18 cm separation the prisms add $\sim$-3×10^5 fs^3 of third order dispersion [19]. This amount

of third order dispersion added to a transform-limited pulse would not account for the wings on the compressed pulse or the measured deviation from the transform limit. Another compression stage to balance the third order dispersion might result in even shorter pulses closer to the transform limit (approximately 40 fs for the measured spectrum).

To characterize the pulses further, keeping in mind that the pulses we are using come from the APM rejection port, a high dynamic range autocorrelation of the compressed pulses was measured. This is necessary since even a very low and broad pedestal will lead to a major portion of the energy residing in this pedestal. For example, in our system, a unity height square pulse of 100 fs duration sitting on top of a 25 ns pedestal of height 10^{-5} will contain only 40% of the energy calculated from the average power and the repetition rate. Figure 2.4 shows the measured high dynamic range autocorrelation on a log scale, and goes down to approximately 5×10^{-5} of the peak of the pulse at 4 ps away from the peak. This leads to an estimated 5% of the energy in the pedestal.

2.1.4 Amplitude noise characterization

An important issue for pump-probe experiments is the stability or amplitude fluctuations of the source, since they will ultimately limit the signal-to-noise ratio in these experiments. To measure the amplitude noise the well known technique [20] [21] of measuring the power spectrum of the laser output on a photodiode with an electronic spectrum analyzer was used. The measured average photocurrent is approximately 2 mA, which corresponds to a shot noise power of -164 dBm/Hz. At this low power the measurement is limited by the spectrum analyzer's noise floor (at -156 dBm/Hz). Figure 2.5 shows the RF spectrum near the first ($k = 1$) harmonic which is centered at the laser repetition rate. The resolution bandwidth for this measurement is 1 KHz. As the figure illustrates, the amplitude noise sidebands are about 90 dB down from the carrier. As pointed out in ref. 20 the ratio of the area of the main spike to the area of the noise sidebands, is directly related to r.m.s. pulse energy deviations (This is true only in the absence of negligible phase noise, which becomes evident in the higher harmonics). A good approximation of this ratio is given by $(P_N \Delta f_n)/(P_c \Delta f_{res})$, where P_N and P_c are the powers at the peak of the noise sidebands and the peak of the carrier respectively, and Δf_N and Δf_{res} are the spectral width of the noise sidebands and the resolution bandwidth respectively. The relative energy fluctuations $\Delta E/E$ are given by the square root of the above ratio.

25

From the data the estimated energy fluctuations are $\Delta E/E = 8 \times 10^{-4}$, i.e., less than 0.1% fluctuation over the noise sideband region extending out to 200 KHz. Beyond 300 KHz the amplitude noise is less than -144 dBm/Hz (20 dB above shot noise), decreasing slowly up to 4 Mhz where it is instrument-limited. The above number should be compared, for example, to the noise of color center lasers, which show noise on the order of 1% even for much narrower frequency ranges [22]. Figure 2.6 is a high-resolution zoom-in on the central spike in Figure 2.5 using a much narrower resolution bandwidth (30 Hz)
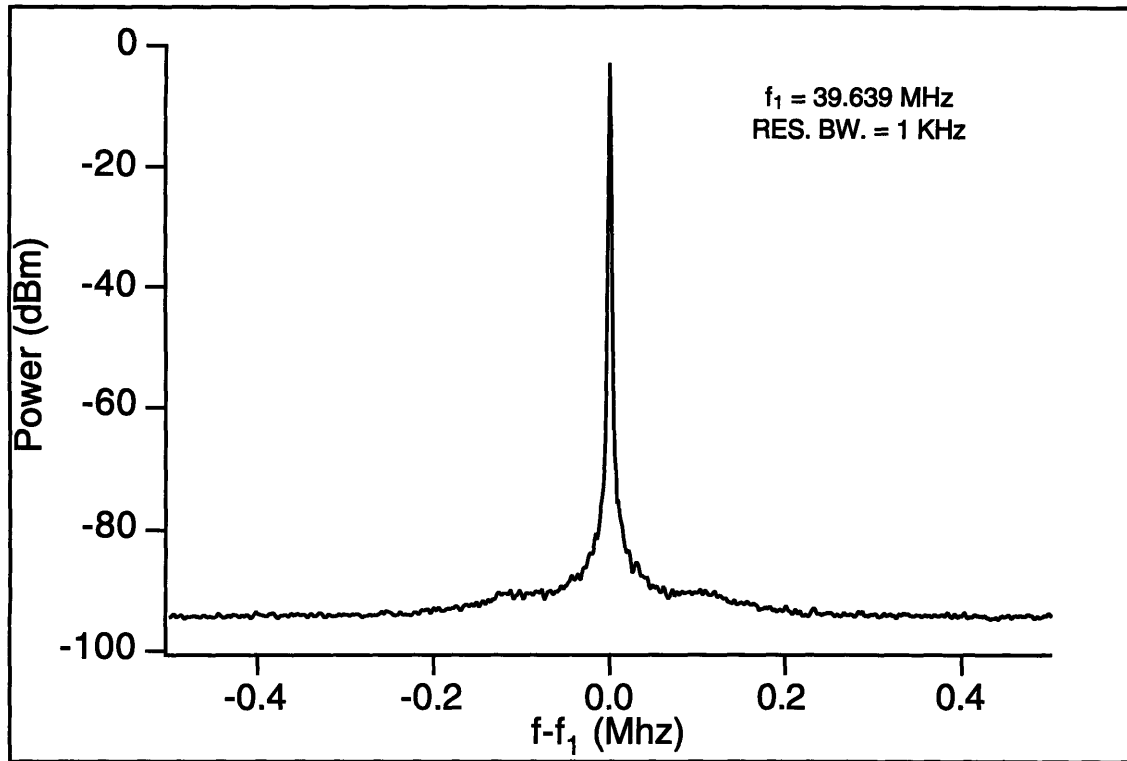
Figure 2.5: RF spectrum of the SP-APM fiber laser near the first harmonic at 39.6 Mhz.

on the RF spectrum analyzer. This spectrum shows the lower frequency noise and in particular noise sidebands at ~ 2 kHz, which are probably due to relaxation oscillations. It should also be noted that in the above measurement the MOPA was operated at constant current. The MOPA can also be operated in constant power mode when a feedback signal (such as the silicon photodiode output) is used, for even stabler operation at low frequencies.
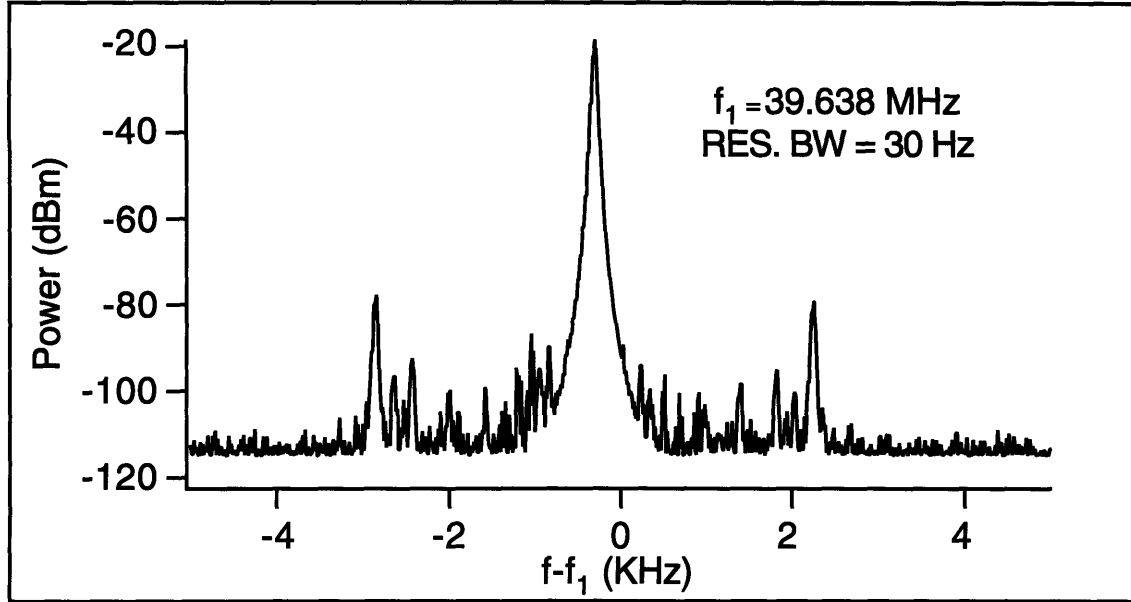
Figure 2.6:   High resolution RF spectrum of the SP-APM fiber laser.

2.1.5 Frequency doubling

Recently it has become of interest to find alternatives for a seed laser in a Ti:Sapphire regenerative amplifier system. One proposed alternative would be a frequency-doubled stretched-pulse APM fiber laser, pumped by a MOPA. This would eliminate the need for an argon ion laser and a modelocked Ti:Sapphire, replacing them with a much cheaper and more compact source for the amplifier. To make this viable the doubling efficiency has to be high without drastic degradation of the second harmonic pulsewidth. High conversion efficiency implies a longer nonlinear crystal, but because of walkoff between the fundamental and frequency-doubled pulse, a longer crystal would lead to pulse broadening of the frequency-doubled pulse. Since this is not simple broadening due to GVD, these pulses would not be compressible using standard grating or prism compressors.

Two different SHG crystals were investigated: $KNbO_3$ and BBO. $KNbO_3$ has a higher second order nonlinearity, but is also more dispersive than BBO. In both cases the crystal length was 1.5 mm. To characterize the effective bandwidth for frequency doubling, the spectrum of the frequency-doubled pulse was compared to the spectrum of the fundamental convolved with itself [23]. The ratio of these gives the effective filter due to phase matching bandwidth and will be narrower for longer crystals. Figure 2.7 shows the autoconvolution of the fundamental pulse spectrum and the spectra of the frequency-
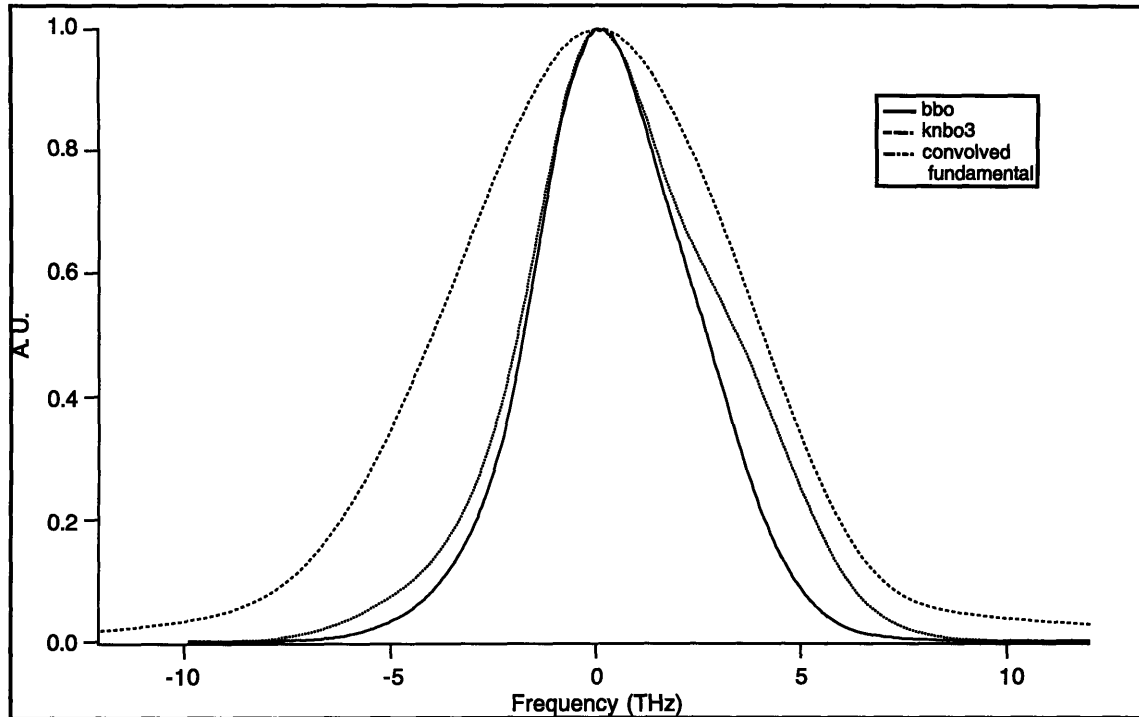
Figure 2.7: Spectrum of the fundamental pulse convolved with itself (dashed line) compared with the SHG spectrum for two types of doubling crystal: BBO (solid line) and $KNbO_3$ (dotted line).

doubled pulses from the $KNbO_3$ and the BBO (the carrier frequency has been removed to allow direct comparison of the different bandwidths). Because the spectrum from the fiber laser is extremely broad, a large fraction of that spectrum is lost because of the filtering in the SHG crystal. Also, the spectrum of the frequency-doubled pulse from BBO is broader than the one from the $KNbO_3$ as expected (because BBO is less dispersive its phase matching bandwidth is broader). From the full width at half maximum of the frequency doubled spectrum produced by the BBO crystal, a ~ 70 fs pulse width can be inferred (assuming a transform-limited pulse).

The average power of the frequency-doubled pulse train was measured for both crystals. For a given input power of the fundamental pulse, the power from the $KNbO_3$ was typically 4 times higher than that from the BBO. For an average power of 45 mW and 125 fs pulses at the input up to 320 μW of frequency-doubled power was achieved with the right focusing ($f = 30$ mm). Because the doubling system was not optimized for the 1.5 μm wavelength, only an estimated 40 mW entered the crystal. Since the repetition rate is ~ 40 Mhz, 1 nJ fundamental pulses were converted to 8 pJ of frequency-doubled pulses, to

28

yield 0.8% conversion efficiency. Further tweaking (e.g., the pulsewidth) would result in a ~ 1% conversion efficiency. This low conversion efficiency may be due to the effective filtering of the SHG crystal mentioned earlier, so that effectively only half of the input power is being converted. Since the conversion efficiency scales linearly with input power, an increase in input power would yield higher conversion efficiencies. If the prism system were to be made lossless (with higher grade silicon) and the crystal and optics optimized for 1.5 μm, then at 80 mW input a conversion efficiency of at least 2% may be expected, resulting in 1.6 mW of frequency-doubled average power or an energy 40 pJ per pulse.

2.2 Color center amplifiers

In order to get high energy femtosecond pulses at 1.5 μm a broadband gain medium centered at this wavelength is required. A natural choice would be a color center crystal, since these crystals have proven to be good gain media for solid-state lasers in this spectral region. Another choice would be the Cr^{4+}:YAG crystal, however these crystals are still in early stages of development and require some further study. Yet another choice would be an optical parametric amplifier (OPA).

Color center crystals have been used as gain media for lasers at 1.5 μm for many years and are fairly well understood, and therefore were chosen as the amplifier gain medium for this project. In particular, a solid-state 1.5 μm amplifier based on the NaCl:OH⁻ color center crystal was recently demonstrated [24] [25]. Since this amplifier worked well it was the first choice in this project, and a multiple-pass NaCl:OH⁻ color center amplifier seeded by an APM NaCl:OH⁻ color center laser. For reasons to be explained below, this system was ultimately replaced by a KCl:Tl⁺ color center amplifier seeded by a stretched-pulse APM fiber laser, which proved to be a superior system in many respects.

2.2.1 The NaCl color center amplifier and its disadvantages

The NaCl:OH⁻ color center crystal, when pumped by a Nd:YAG laser, has broadband gain centered at 1.58 μm. However, because of orientational bleaching [26] it requires an auxiliary pump; otherwise the gain "fades". The auxiliary pump laser excitation in NaCl:OH⁻ is needed to excite a higher energy (~2 eV) transition of the active color center, and thus to counteract center reorientation effect. This is one of the main disadvantages of this crystal, since the requirement of overlapping three beams in the gain crystal adds to the complexity of the system. In addition, this 2 eV transition is masked by the absorption band of F centers. The latter are formed in much higher concentrations than the active color

29

centers, are very difficult to remove, and render the crystals virtually opaque in the 2 eV range. As a consequence, losses are high, excitation of the active color centers is rather ineffective and the single-pass gain of NaCl:OH⁻ amplifier crystals therefore is low. This in turn necessitates several passes (typically 4-5 passes were required to reach microjoule energy levels) and the beam's spatial profile was distorted and filamented, due to imperfect polishing of the crystal faces and internal inhomogeneities.

This NaCl:OH⁻ amplifier was used in conjunction with an APM NaCl:OH⁻ laser as a seed. Since this seed laser needed active stabilization and had relatively high amplitude noise [22], it made a rather imperfect source for amplification, although its gain spectrum was automatically matched to that of the amplifier crystals (as opposed to the fiber laser discussed below).

2.2.2 The KCl color center amplifier

The shortcomings of the all NaCl:OH⁻ system led to the consideration of an alternative amplifier crystal and alternative seeding laser. $KCl:Tl^+$ is the second popular color center crystal with gain spectrum centered in the 1.5 μm region, and has been used extensively as a laser crystal in this spectral region. Since this crystal does not suffer from orientational bleaching effects it requires only a single pump laser - the Nd:YAG. The homogeneity of the crystals is much better and therefore the internal losses are lower. Even though the emission cross-section is about 6.5 times lower than the NaCl:OH⁻ (1.3×10^{-17} cm⁻² as opposed to 8.5×10^{-17} cm⁻²), the doping densities that can be achieved are much higher, so that the small-signal single-pass gain through a 2 cm long crystal $G = \exp(\sigma NL)$ can be on the order of 10^3 (σ emission cross-section; N active center density; L crystal length). This in turn leads to the possibility of attaining microjoule level energies in 2 passes and a very high quality spatial beam profile.

As mentioned in section 1.3.1 the SP-APM fiber laser is well-suited for seeding the amplifier, since it does not require active stabilization and it has very low amplitude noise [27] and leads to very stable amplified pulses. It produces pulse energies comparable to the APM color center lasers, but in the from of highly chirped 1-2 ps pulses. This , however, is not a drawback since the amplified pulses need to be recompressed (because of dispersive elements in the amplifier system, notably the electro-optic pulse selector to be described later). The main drawback of using this laser as the seed is the mismatch between its pulse optical spectrum and the gain spectrum of the amplifier crystal. This means that the amplifier is also an effective filter and chops off a significant part of the original pulse spectrum, setting limits on the shortest pulse attainable after recompression.

2.2.3 Amplifier design

The amplifier is a multiple-pass system such that the seeding pulse makes a few passes through the gain medium, which is pumped by a Q-switched Nd:YAG laser. Typically systems like this one use noncollinear geometries (e.g., "bow-tie" geometry) to achieve several passes through the gain region of the crystal. For a long and narrow crystal this may become a serious alignment problem. Also, as mentioned before, if the crystal faces are not of high optical quality (flatness as well as smoothness) or the crystal has defects, cracks, etc., more passes will lead to a quick degradation of the spatial profile of the output beam. This was one of the main weaknesses of the NaCl:OH⁻ amplifier system [24]. If the gain medium has high enough small-signal single-pass gain, then reducing the number of passes is desirable. In the present system it was found that 2 passes were sufficient for output pulse energies of 10 μJ - more than enough for continuum generation with femtosecond pulses.

Since only 2 passes were needed, a collinear geometry is possible and the alignment is simple. The input beam is horizontally polarized and passes through a polarizing beamsplitter (PBS) without any loss. After the first pass the beam is passed through a λ/4 waveplate, is then reflected off a mirror back on itself to pass through the waveplate again and then through the gain medium for the second pass but now with the orthogonal polarization. At the PBS the beam is now reflected out of the system (see Figure 2.8). It should be noted that as will be discussed in section 2.2.4 , the gain is anisotropic and the highest single-pass gain is achieved with the pump linearly polarized at 45°. Since the double-pass collinear configuration requires orthogonal polarizations in the two passes (to allow coupling out after the second pass), it may be that the total gain is not optimized for signal polarization, and avoiding polarization flipping would result in even better performance.

The pump beam is focused into the crystal with a 300 mm focal length lens through a dichroic curved mirror (with radius of curvature $R = 250$ mm or focal length of 125 mm) that transmits the pump at 1.06 μm and reflects and focuses the seeding pulse at 1.5 μm. It should be noted that the pump must be focused tighter than in the NaCl:OH⁻ amplifier system, to make up for the smaller emission cross-section in the present system. This can be understood as follows: In the case where 1) the absorbed pump photon density is less than or equal to the active color center density, 2) the confocal parameter of the pump beam is larger than the crystal length, and 3) every pump photon is absorbed and utilized for gain, the small-signal single-pass gain may be written:

R = 25 cm

λ/4

KCl
crystal

Dewar

R = 25 cm

30 cm

λ/2

Q-Switched Nd:YAG
1.06 μm, 1 KHz
1.4 mJ, 80 ns

PBS

λ/2

Electro-optic
pulse selection

Isolator

Stretched-pulse
APM fiber laser
1.5 ps pulses
40 MHz, 1.55 μm

Pulse
compression

Amplified μJ pulses
250 fs, 1 KHz
1.52 μm

Continuum
generation

Figure 2.8:   KCl amplifier system experimental setup

$$G = \exp(N\sigma L) = \exp\left[\left(\tilde{E}_p \big/ \pi\omega_0^2 L\right)\sigma L\right] = \exp\left(\sigma \tilde{E}_p \big/ \pi\omega_0^2\right) \qquad (2.1)$$

where $\tilde{E}_p = E_p/\hbar\omega$ is the pump pulse energy divided by the photon energy (i.e., the number of pump photons per pulse), ω_0 is the pump spot radius, and σ, N, L were defined earlier. For given pump energy a reduction of the emission cross-section requires a corresponding reduction in the pump spot area to achieve the same gain. Obviously reduction of the pump spot is desirable as long as it does not lead to the confocal parameter being smaller than the crystal length or absorbed photon densities greater than the active color center density. These conditions may be written, respectively, as follows:

$$\omega_0 \geq \sqrt{\frac{L\lambda}{2\pi n}}$$

$$\omega_0 \geq \sqrt{\frac{\tilde{E}_p}{N_0 \pi L}} \qquad (2.2)$$

where λ is the center wavelength, n is the refractive index and N_0 is the density of the active color centers.

The reflecting mirror after the first pass was a curved high reflector for 1.5 µm light with the same radius of curvature. Placing it approximately a distance of 2 focal lengths away from the gain medium, re-images the waist back into the crystal. The output beam after the 2 passes was found to have excellent spatial quality with no obvious filamentation or distortion.

Since the seeding pulse must arrive at the gain medium together with the pump pulse, synchronization is required. Furthermore, the repetition rate of the seeding fiber laser is approximately 40 Mhz, whereas the repetition rate of the Q-switched Nd:YAG pump laser is 1 kHz. This means that pulse selection is necessary to match the pump laser rate. Pulse selection was performed by means of an electro-optic (E-O) cell, which can "open" for 10 ns and let only one pulse through. The E-O crystal is made of $LiTaO_3$ and is 8 cm long and its dispersion is such that it will broaden a 100 fs pulse at 1.5 µm to about 750 fs. When the input beam to the E-O cell is well polarized the rejection ratio is typically 150:1. The E-O cell can operate at up to 50 kHz, but in this system was operated at 1 kHz to match the pump laser, so by letting one pulse through every 1 ms, the fiber laser repetition rate was divided down. Since the fiber laser is a passively modelocked laser, there is no timing ref-

33

erence (such as a modelocker driver signal in an actively modelocked system) and therefore the output pulse train itself was used as a trigger for the countdown circuit. Additionally, the Q-switched laser served as the master "clock", and the signal pulses were timed relative to and dependent on the pump pulse. Any timing jitter in the pump pulse "dragged" the signal pulse along, rather than causing it to miss the pump pulse altogether.

The synchronization worked as follows: the Q-switched pump laser put out an electrical signal whenever a pulse was shot. This signal (after being converted to a standard TTL signal) was then used as a gate to the countdown circuit. Simultaneously, a small fraction of the fiber laser output was leaked onto a fast photodiode (1 ns risetime), which was fed into the countdown circuit. Any signal over some adjustable threshold is counted by the circuit. The countdown circuit was programmed such that following the gate pulse from the pump laser, the countdown circuit would start counting a preset number of pulses and then "open" the E-O cell for one pulse. By changing this preset number the relative delay between the pump pulse and the seeding pulse may be adjusted. In this scheme, the seeding pulse train will automatically be slaved to the 1 kHz pump repetition rate and the selected pulse may be timed to arrive at the gain medium with the pump pulse.

2.2.4 Single pass performance

The amplifier crystal was a 2 cm long $KCl:Tl^+$ color center crystal, placed in an evacuated dewar and cooled down to 77° K. The gain region was created by bombarding the crystal with high-energy electrons. This region was very dark and extended only to the penetration depth of the high-energy electrons, beyond which the crystal was transparent. The border between these regions in the crystal, has a graded color center density and it was in this transition region where highest gain was achieved. The dewar windows were slightly tilted and one of the faces of the crystal was beveled at an angle, all to avoid lasing between parallel surfaces.

The Q-switched Nd:YAG laser put out 80 ns, 1.4 mJ pulses at a repetition rate of 1 kHz, which were focused to a ~ 100 µm spot in the crystal. Since the gain in these crystals is anisotropic a waveplate was used in the pump beam and it was found that the best results were achieved with a λ/2 waveplate, rotating the pump to 45° linear polarization. The highly-chirped 1.5 ps pulses from the fiber laser were not compressed before amplification, because of the high dispersion of the E-O cell. The fiber laser output train was passed through an isolator (which also served to polarize the beam), through the E-O cell, an additional λ/2 waveplate to rotate the polarization to horizontal and then through the PBS. The beam was reflected and focused (collinear with the pump) to ~ 60 µm spot in the
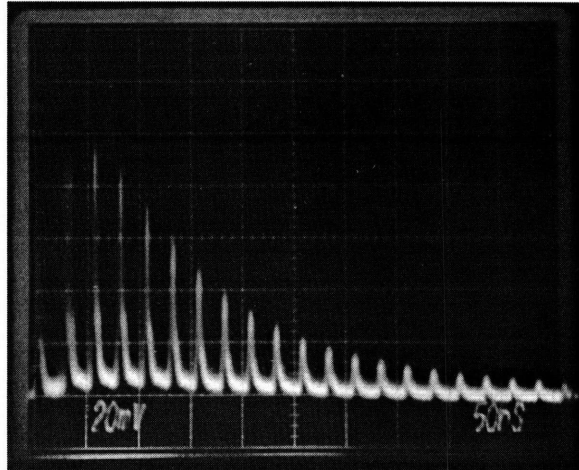
Figure 2.9:   Amplified pulse train (no pulse selection)

crystal and a fast photodiode was used just after the crystal (after passing through a silicon filter to filter out the pump). The selected pulse was observed with the pump on and the pump off and the ratio was measured. In this way the gain of the crystal is measured directly, the linear losses (e.g., reflections at the crystal surfaces) are normalized out. As mentioned earlier the dependence on signal polarization was not checked, since the system geometry dictated the polarization of the signal.
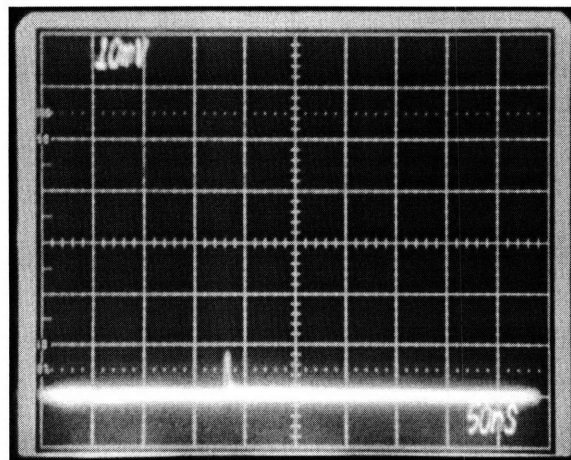
Figure 2.10:   Selected pulse before amplification (pump is off). Note that the vertical scale here is 10 mV/div.

Typically, the small-signal single-pass gain measured in this way was ~ 1000, and could be "tuned" to some extent by moving the beams across the graded region in the crys-

35

tal mentioned above. Figure 2.9 shows the amplified pulse train with the pump on, but with no pulse selection. Figure 2.10 and Figure 2.11 compare the transmitted seeding pulse with pump on and the pump off. As can be seen in these figures the gain is close to 1000.
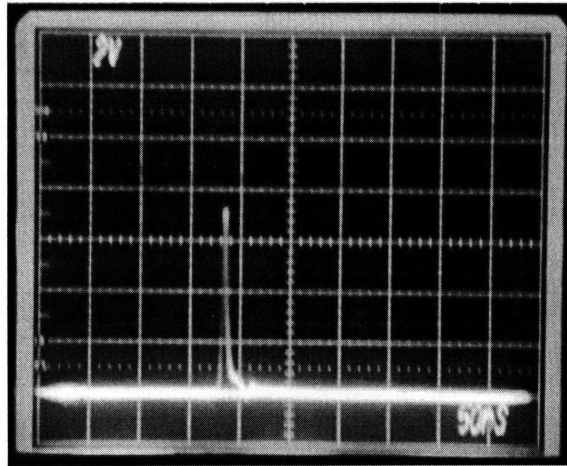
Figure 2.11:   Selected pulse after single-pass amplification (pump in on). Note that the vertical scale here is 2 V/div.

2.2.5 Double pass performance

After maximizing the signal after the first pass, the beam was reflected back for the second pass collinear with the first pass. The resulting average output power was measured after the PBS and an additional $\lambda/2$ waveplate (to rotate the polarization back to horizontal). After dividing by the 1 kHz repetition rate to get the energy per pulse, it was compared to the energy of the pulses just before the crystal (usually accomplished by turning pulse selection off, measuring the average power and dividing by the 40 MHz repetition rate of the seeding fiber laser). The ratio of these measured pulse energies is the total energy gain of the amplifier system and was found to be up to 13000, yielding pulse energies of ~ 10 µJ.

The amplified pulse train was passed through a double pass silicon prism pair arrangement to recompress the amplified pulses (similar to the one described in section 2.1.3). As mentioned in section 2.1.3, because the prisms are somewhat lossy, there are about 30% transmission losses through the compressor. The compressed amplified pulses were as short as 220 fs and the spectrum was about 21 nm wide as shown in Figure 2.12. This implies a time-bandwidth product of approximately 0.6 (assuming sech shaped pulses).

36
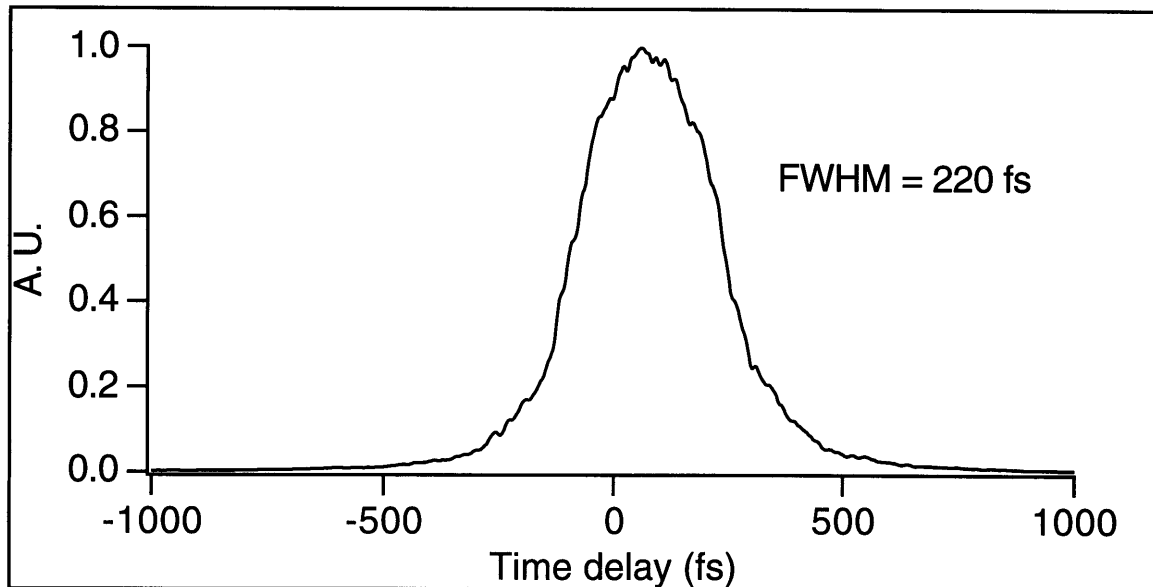
(a)
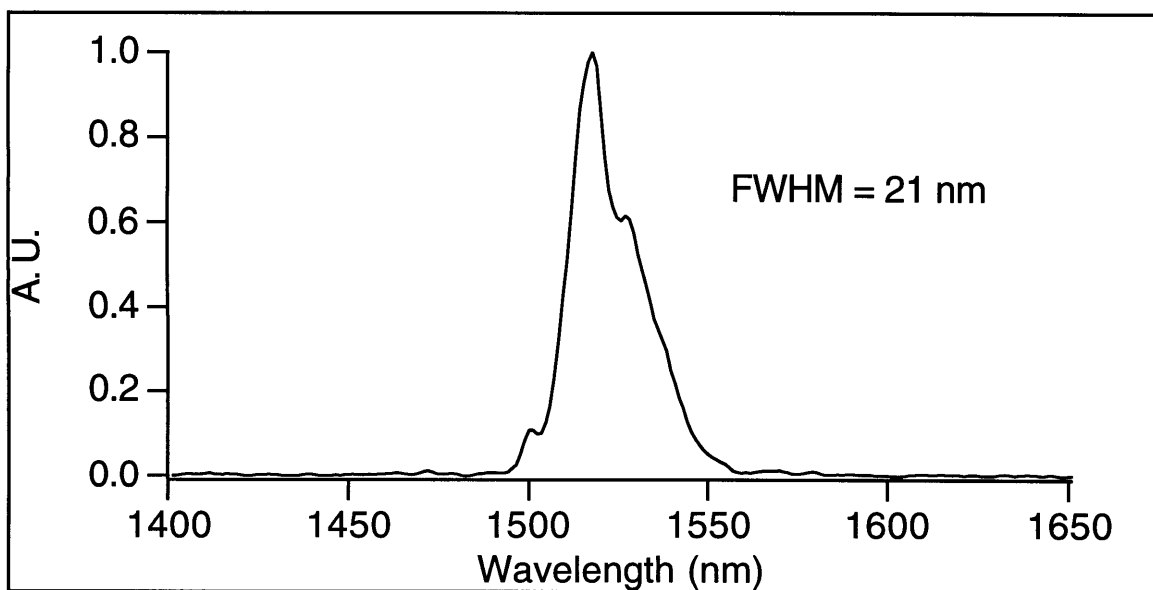
(b)

Figure 2.12: (a) Intensity autocorrelation of amplified pulse. (b) Spectrum of amplified pulse.

The reason for not achieving shorter pulses is apparent in Figure 2.13, which compares the original spectrum of the output of the fiber laser and the spectrum of the amplified pulses. Because of the mismatch between the fiber laser center wavelength (at 1.56 μm) and the amplifier gain bandwidth (centered at 1.52 μm), the amplifier acts as an effective filter and chops off most of the long wavelength content of the original pulses, reducing the bandwidth by a factor of 3. The remaining spectrum must contain higher order chirp, which is not compensated and hence the non-transform-limited result. This gain narrowing
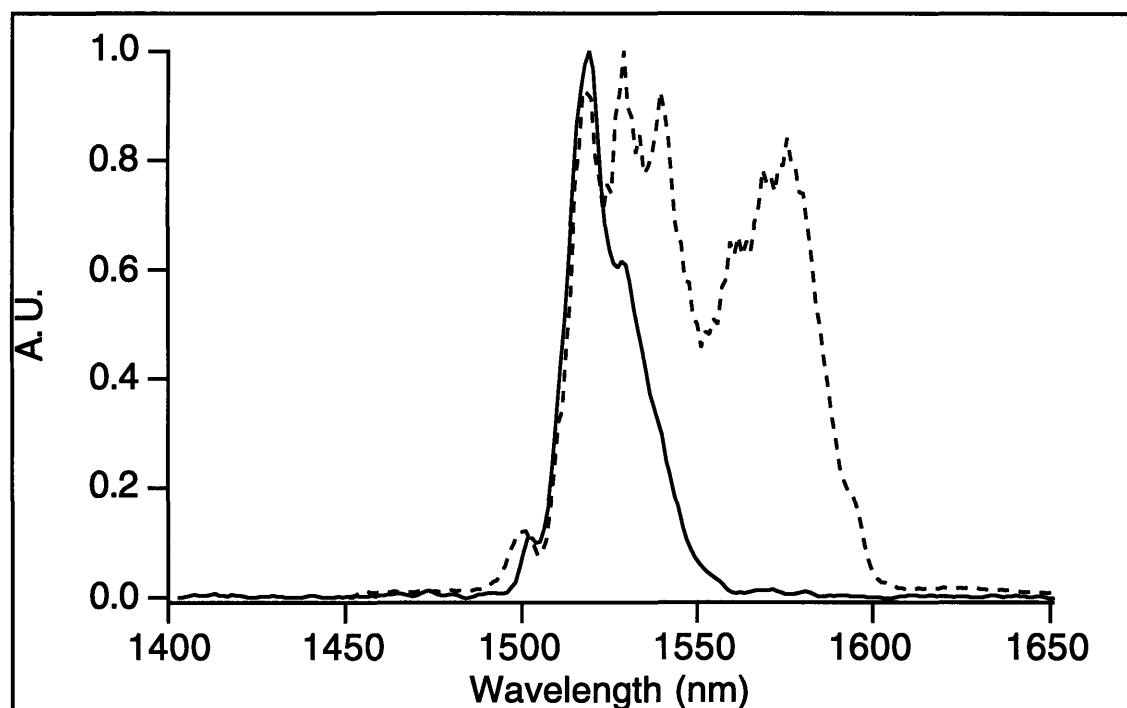
Figure 2.13: Comparison of pulse spectrum before amplification (dashed line) and after amplification (solid line). This demonstrates the gain narrowing in the amplifier.

effect means a loss of energy, so by finding a similar crystal but centered closer to the fiber laser center wavelength, the improvement in peak power may be dramatic. One possible color center crystal that would fit this description is KBr. Alternatively the seeding laser may be replaced with an APM $KCl:Tl^+$ color center laser. However, as pointed out earlier this source requires active stabilization and is much noisier. Under typical operation conditions, after compression the amplified pulses have a 250 fs duration with 5 μJ energy per pulse for a peak power of ~ 20 MW.

2.2.6 Continuum generation and spectral slicing

As explained in the introduction, the goal for the amplifier is to produce high intensity ultrashort pulses to facilitate time-resolved nonlinear optics experiments. In particular we are interested in femtosecond continuum generation - the extreme spectral broadening of femtosecond pulses. To this end the compressed output pulses from the amplifier were focused into various materials to investigate which would give the best spectral broadening. The materials investigated included 2 types of bulk glass, ZnSe and standard optical fiber. The focused spot in the case of bulk materials was ~ 50 μm for a peak intensity of 2.5×10^{11} W/cm^2. In the case of fiber the beam was focused to the effective fiber core radius (~ 4 μm) and the peak intensity (taking into account coupling losses) reached ~ 2×10^{13} W/cm^2.

The spectral broadening is due to self-phase modulation (SPM) and is enhanced through self-focusing effects, such that the effective length where SPM takes place is much longer than the confocal parameter. The critical power for self-focusing is defined as [28]:

$$P_c = \frac{\lambda^2}{2\pi n_0 n_2}$$

(2.3)

where λ is the free space wavelength, n_0 is the linear refractive index and n_2 is the nonlinear refractive index. In the present experiment for continuum generation in ZnSe, for example, the critical power is ~ 25 kW, which means that the peak power mentioned in the last section is approximately 800 times the critical power. The distance to self-focusing is [28]:

$$L_s = \frac{\pi \omega_0^2}{\lambda} \sqrt{\frac{P_c}{P}}$$

(2.4)

where the factor before the radical is simply the confocal parameter for the beam at the input of the material and P its peak power. In order for self-focusing effects to take place the material has to be at least this thick, otherwise only SPM will occur. The accumulated nonlinear phase over a distance L can be written as:

$$\phi_{NL} = \frac{2\pi}{\lambda} n_2 \int_{-L/2}^{L/2} \frac{P}{\pi \omega^2(z)} dz = \frac{2\pi}{\lambda} n_2 \frac{\pi \omega_0^2 n_0}{\lambda} \frac{P}{\pi \omega_0^2} 2 \tan^{-1}\left(\frac{L}{2 z_0}\right) =$$

$$= 2 \frac{P}{P_c} \tan^{-1}\left(\frac{L}{2 z_0}\right)$$

(2.5)

39

From the previous 2 expressions the following can be concluded: 1) if the P is on the order of P_c, the distance to self-focusing is one confocal parameter and therefore if L is not much thicker than that no appreciable self-focusing will occur and SPM will give only π radians nonlinear phase shift and hence almost no spectral broadening. 2) if P is much larger than P_c, the distance to self-focusing is much smaller than the confocal parameter. If we set L, the thickness of the material, to that distance we get for the nonlinear phase due to SPM alone (from the last expression):

$$\phi_{NL} \approx \frac{P}{P_c} 2 \frac{L}{2z_0} = \frac{P}{P_c} \frac{z_0\sqrt{P_c/P}}{z_0} = \sqrt{\frac{P}{P_c}} \qquad (2.6)$$

So, for example, in the present experiment for continuum generation in ZnSe, $P/P_c \approx 800$ and the corresponding nonlinear phase shift is only about 9π radians. This gives relatively small spectral broadening, certainly not a supercontinuum. This discussion demonstrates how essential self-focusing is to the continuum generation process.

The extent of the continuum is not symmetric around the center wavelength (which would be expected if only SPM were present), and this is due to any asymmetry in the pulse. This asymmetry can be present in the initial pulse or could be due to propagation effects, such as self-steepening, time dependence of the nonlinear index, etc. [29]. For the case of no self-focusing and self-steepening included only in the equation for the phase of the pulse (assumed to be a sech), the continuum bandwidth is given by [29]:

$$\frac{\Delta\omega_\pm}{\omega_0} = \frac{1}{2}\left(\sqrt{Q^2 + 4} \pm |Q|\right) - 1$$

$$Q = \frac{n_2 IL}{c\tau} = \frac{\phi_{NL}}{\omega_0 \tau} \qquad (2.7)$$

where ω_0 is the center frequency of the original spectrum, $\Delta\omega_-$ is the maximum extent of the continuum on the low frequency side (Stokes side), $\Delta\omega_+$ is the maximum extent of the continuum on the high frequency side (anti-Stokes side), n_2 is the nonlinear index, I is the peak intensity, L is the total length, c is the speed of light, ϕ_{NL} is the peak nonlinear phase and τ is the pulsewidth. When $Q \gg 1$ (referred to as a supercontinuum) $\Delta\omega_+/\omega_0 \approx |Q|$ and $\Delta\omega_-/\omega_0 \approx 1/|Q| - 1$ (which can be no larger than ω_0, as would be expected). As can be seen, the extent of the spectral broadening depends on Q and therefore depends on the

magnitude of the nonlinear index n_2. The bulk materials that were used to generate continuum were high n_2 materials, but such that the nonlinearity was far from any resonance to avoid any significant absorption.

Some of the materials that were tried and did not conform to the above specifications were the following: 1) GaAs - two-photon absorption is too high and everything is absorbed; 2) Sapphire - even though this is a very popular continuum generator in the visible, around 1.5 μm n_2 is too small and the corresponding spectral broadening was negligible. 3) BaF_2 - only very small spectral broadening due to low n_2.
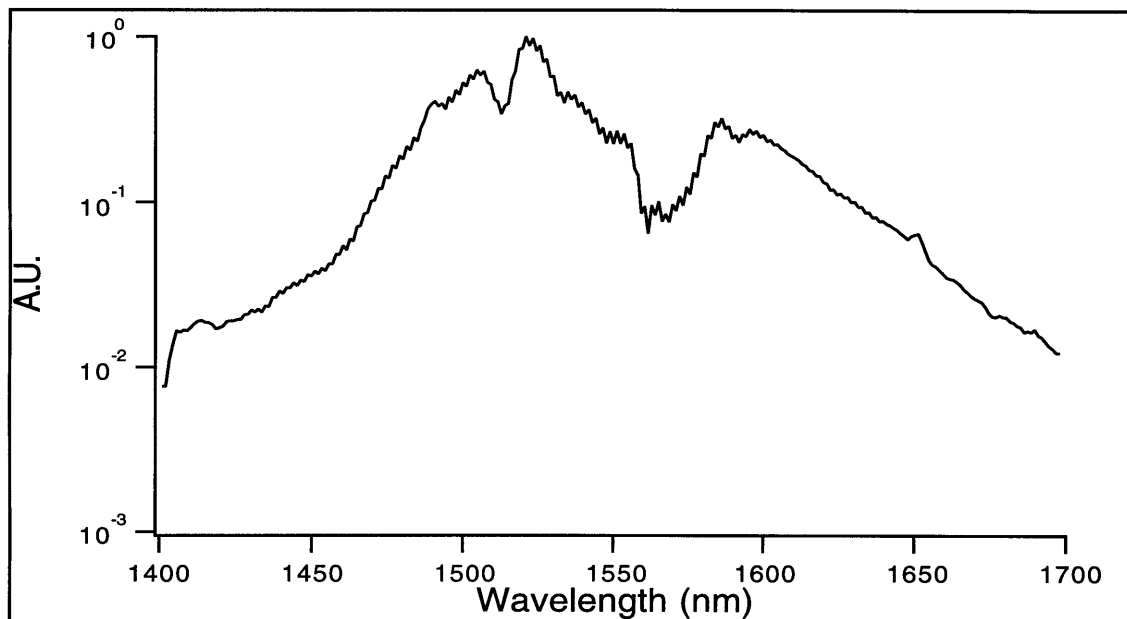
Figure 2.14: Continuum spectrum produced from BK7 glass

2.2.7 Continuum generation in glasses

The first materials that we used successfully for the continuum generation were 2 types of glass: BK7 and SF56. BK7 is a standard glass from which many optical components are made, with an n_2 of 6.4×10^{-16} cm^2/W, whereas SF56 is not as common, but has a very high n_2 of 4.3×10^{-15} cm^2/W (which is ~ 15 times larger than that of standard glass fiber). In the case of BK7, a small 1-2 mm bluish streak that looked like a tiny filament appeared in the material and could be moved by changing the distance of the focusing lens from the glass. This is probably the region of strong self-focusing, where the intensities are high enough to cause multiphoton absorption and subsequent blue fluorescence. This streak may be associated with the dynamically moving focus [30] [31]. No such streak was ob-

served in the SF56 even though it has a higher nonlinearity (maybe because of a lower multiphoton absorption cross-section or the fluorescence occurring in the UV).

The continuum spectrum was recorded with an optical multichannel analyzer (OMA) with a linear InGaAs photodiode array and a 150 lines/mm grating. The spectrum was not a single shot spectrum, since the minimum time to read out the photodiode array is 15 ms, but the pulses are spaced by 1 ms. The resulting spectra recorded here are therefore aver-
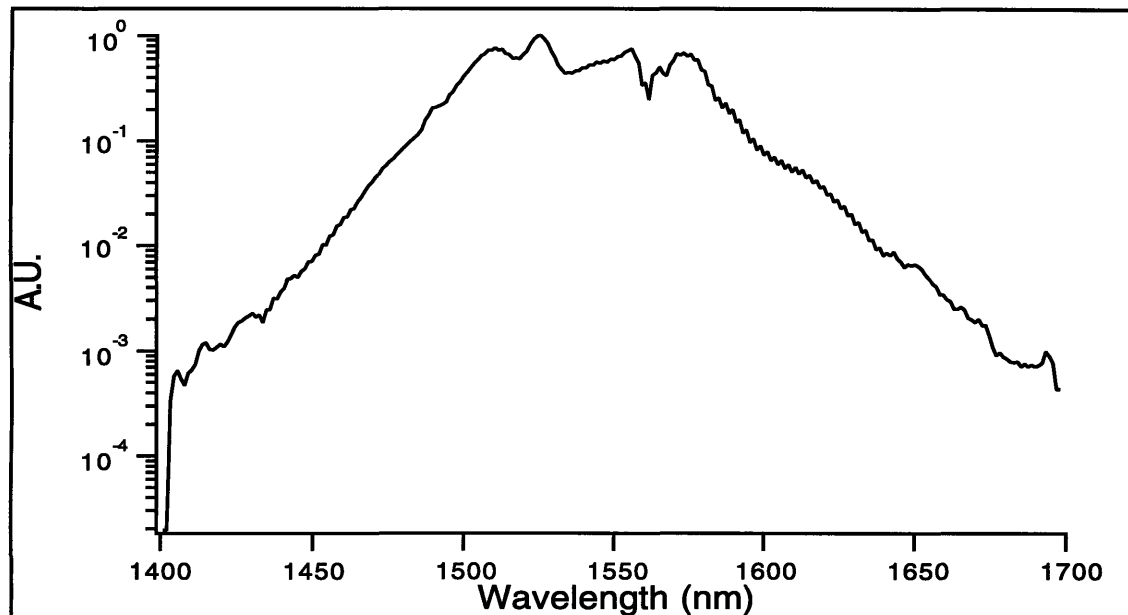
Figure 2.15: Continuum spectrum produced from SF56 glass

ages of approximately 15 successive spectra. The range of the spectrum that was recorded was from 1400 nm to 1700 nm. On the long wavelength side it is limited by the efficiency of the detector array, which drops off sharply around 1700 nm. Extending the range on the short wavelength side requires moving the grating and recalibrating the OMA. The spectra shown here are on a log scale, and it should be remembered that the area under the spectrum contains a few microjoules of energy. So that even regions in the spectrum which are 3 orders of magnitude down from the peak may contain significant energy. Figure 2.14 shows the continuum spectrum produced from the BK7 glass and Figure 2.15 the spectrum from the SF56 glass. The drop at the low wavelength edge of the spectrum is not real and is due to a "dead" diode in the OMA.

2.2.8 Continuum generation in ZnSe

Another candidate for continuum generation would be a semiconductor, where $n_2 \propto 1/E_g^4$, E_g being the bandgap of the semiconductor [32] (This theory also applies to insulators such as KCl and NaCl, the only difference being their much larger bandgap). This implies that by going to lower bandgap the nonlinearity increases very quickly. However absorption processes need to be taken into account, and in the intensity regimes discussed here multiphoton absorption processes become important. In fact the cross-sections for
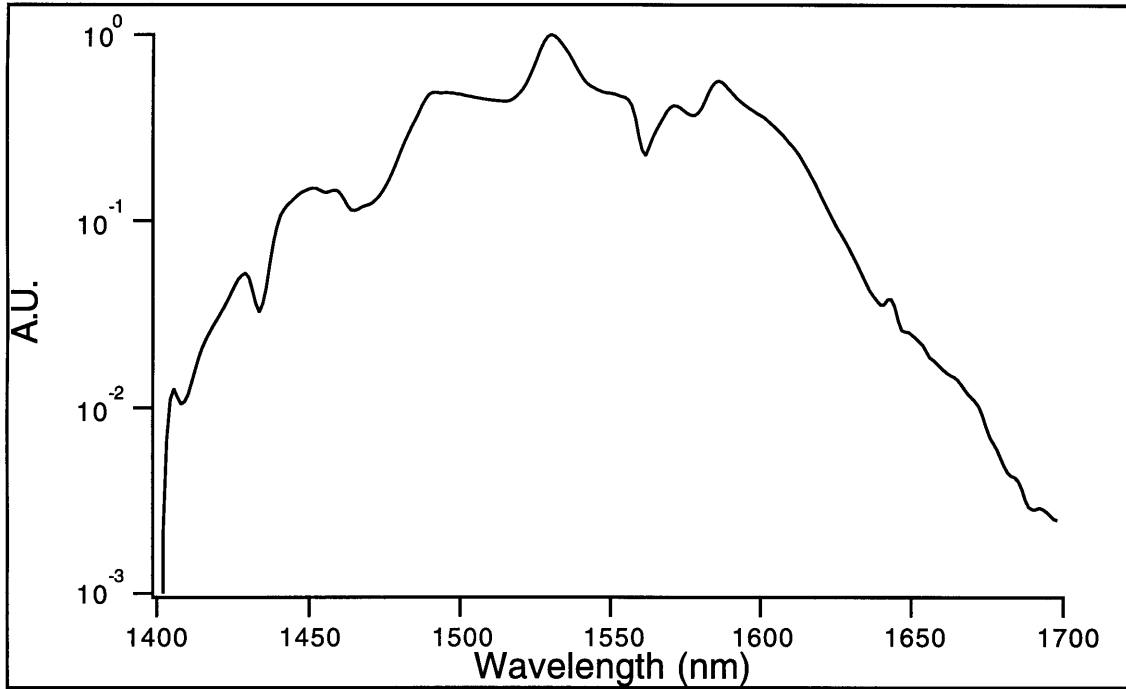
Figure 2.16: Spectrum of continuum produced from ZnSe

these processes also scale with powers of E_g^{-4} [33]. ZnSe has a bandgap of ~ 2.7 eV which requires at least four 1.5 μm photons to bridge the bandgap. For this wavelength region n_2 is almost dispersionless and is given in the literature $n_2 = 5.5 \times 10^{-14}$ cm²/W [32]. For the continuum generation a commercial 3 mm polycrystalline plate of ZnSe was used. Once the focusing was adjusted correctly, blue luminescence was observed indicating some multiphoton absorption. The continuum was very broad and extended into the visible, where some red light was observed. Figure 2.16 shows the portion of the ZnSe continuum spectrum centered around 1550 nm.

2.2.9 Continuum generation in fiber

To try and get the most spectacular results as far as continuum extent, the amplified compressed pulses were coupled into a 12 cm long standard glass fiber. The small effective area and the long interaction length lead to huge nonlinear phase shifts and therefore to extremely broad spectra. Under these conditions the fiber glowed orange, presumably
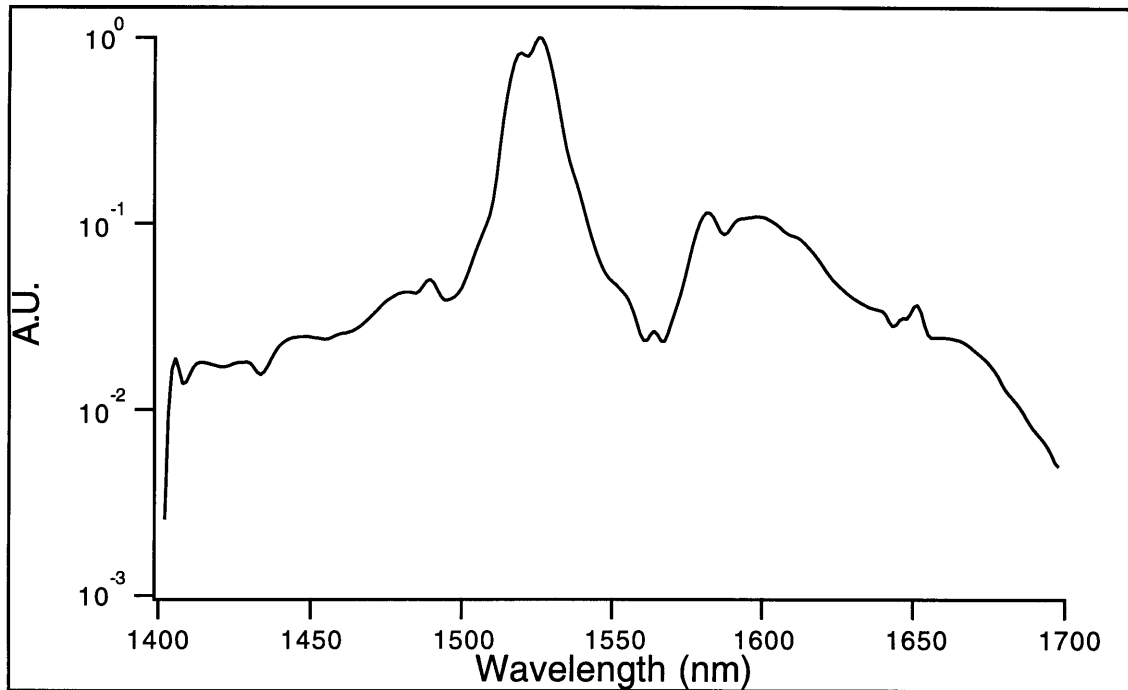
Figure 2.17: Spectrum of continuum produced from a 12 cm long standard glass fiber

from higher transitions luminescing. The output of the fiber contained a yellow center surrounded by a deep red ring followed by a yellow ring and finally a green-blue ring. These effects may possibly be explained by some of the visible light being in a higher transverse mode, or simply having a different diffraction pattern. This output was then spread by means of a 600 lines/mm grating showing a continuous spectrum from blue to red. Figure 2.17 shows IR part of the fiber continuum spectrum. It should be pointed out this spectrum is unusable as a femtosecond continuum, because in this extreme case the temporal shape of the pulse is not preserved across the continuum. It is not even clear what processes take place under these high intensities and long interaction lengths, much less what happens to the initial femtosecond pulse and its spectrum. However, it may be a very good CW tunable coherent white light source.

44

The above results suggest some more materials that would be suitable for continuum generation. There are 3 more glasses that have an n_2 even larger than SF56, namely SF57, SF58 and SF59. Unfortunately, SF59 and SF58, which have the highest n_2, are very difficult glasses to process. They stain easily and are very susceptible to environmental conditions. On the other hand SF57 is a very popular glass, which is cheap and easy to handle and has the third highest n_2 (5.5×10^{-15} cm^2/W) in the Schott glass catalog (it was not available during this experiment).

In semiconductors the next choice would be ZnS, which has a bandgap of 3.5 eV and requires 5 photon absorption to cross the bandgap, leading to a significant reduction in multiphoton absorption. The corresponding reduction in n_2 due to the bandgap scaling rule mentioned earlier, would only be a factor of ~ 2.8 relative to ZnSe.

Finally, a shorter piece of fiber on the order of 1 cm will still give enormous spectrum but more usable as a tunable femtosecond source. In fact, using it as a part of a fiber grating compressor, with the fiber having optimal length [34] may lead to some of the shortest pulses around 1.5 μm.
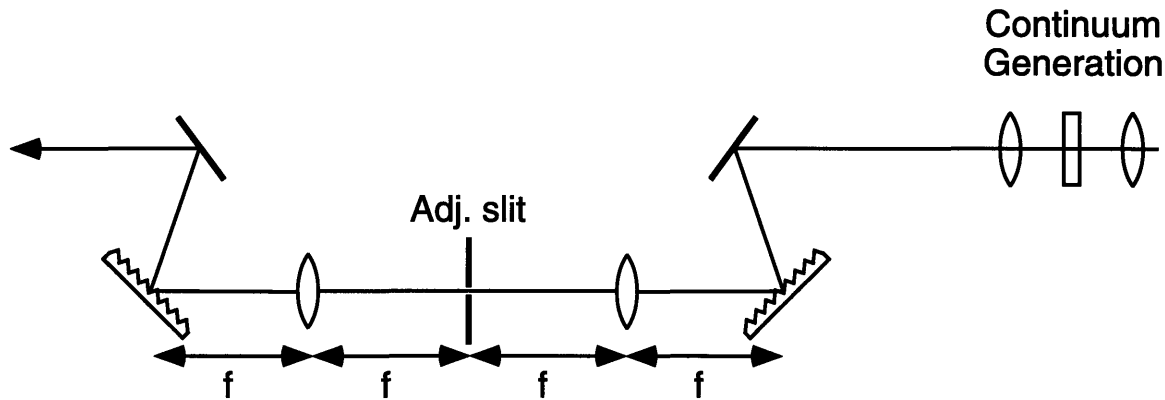
Figure 2.18:   Experimental setup for spectral slicing of the continuum, using a zero dispersion grating compressor. The dispersion may be adjusted by moving the gratings horizontally.

2.2.10 Spectral slicing

The final step in setting up this source requires the ability to slice the continuum and select a tunable variable bandwidth slice. Figure 2.18 shows the setup for such a slicer and is known as a zero dispersion compressor [35]. In the absence of the slit in the center, it im

ages one grating on top of the other with zero separation (hence zero dispersion). In the center a Fourier plane is created, where the spectral components are separated spatially. By placing an adjustable slit on a translation stage at this point, a variable bandwidth filter with tunable center wavelength is implemented. Small adjustments to the grating distances gives limited dispersion control that may lead to some further pulse shortening.
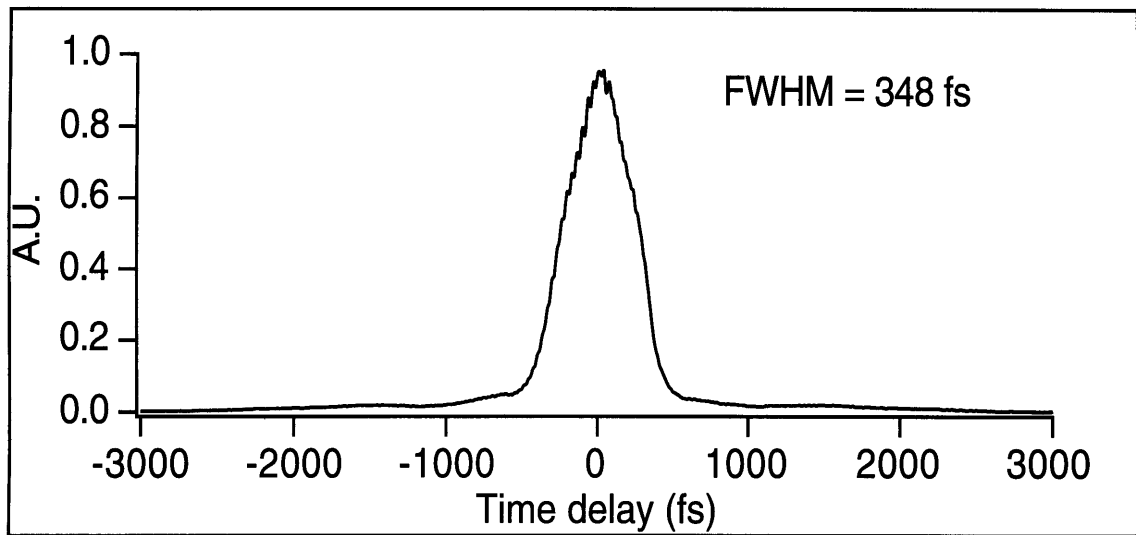
(a)
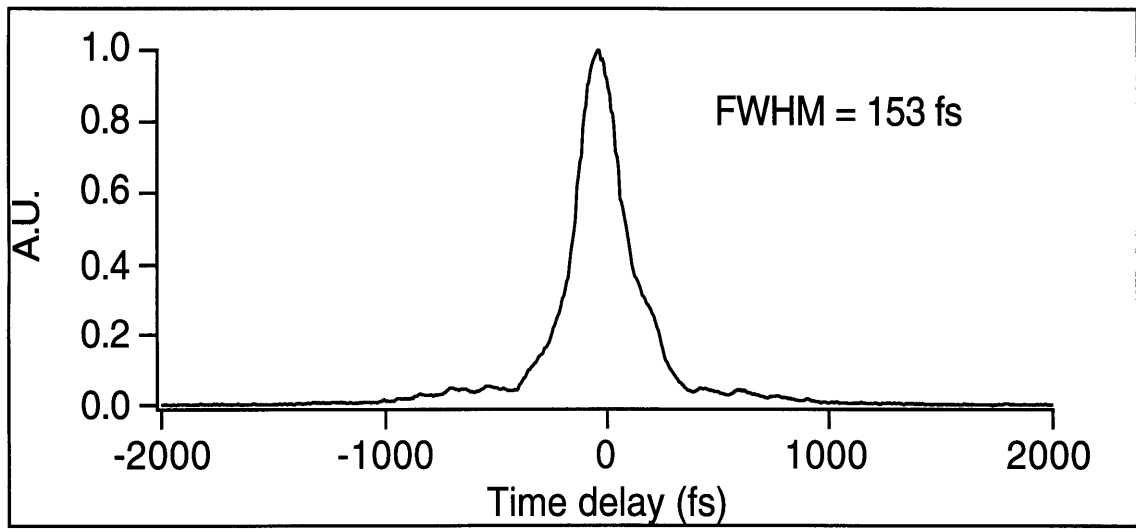
(b)

Figure 2.19: Comparison of intensity autocorrelation of continuum pulse before (a) and after (b) spectral slicing. The continuum was produced from SF56 glass.
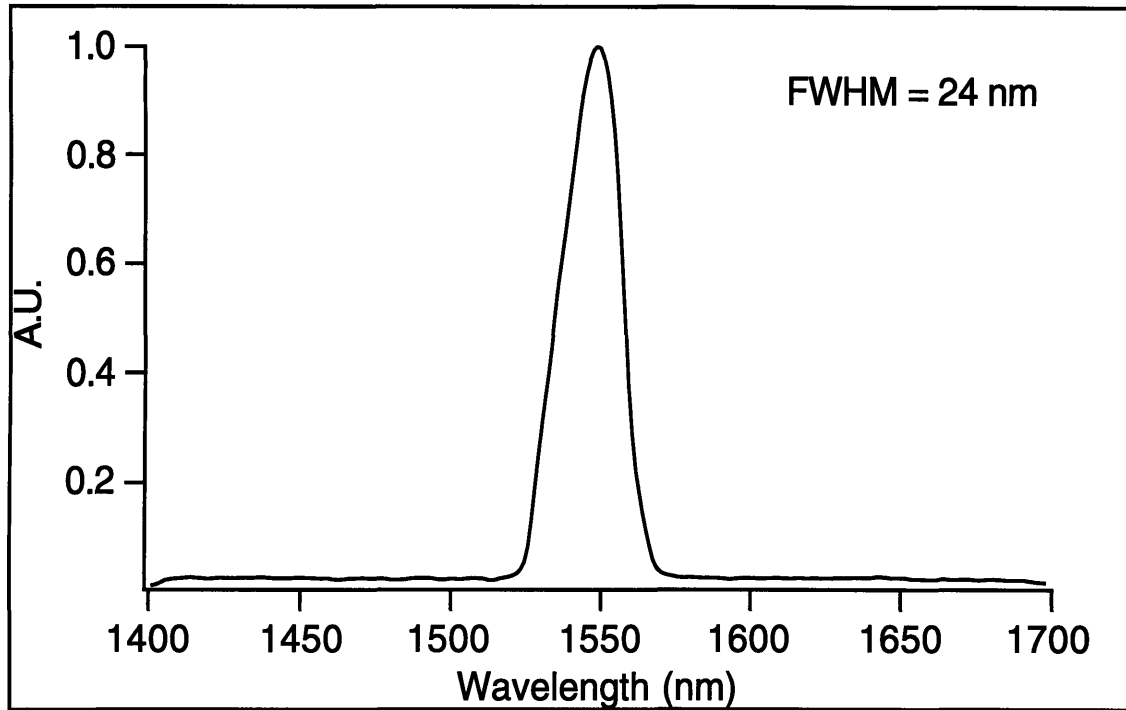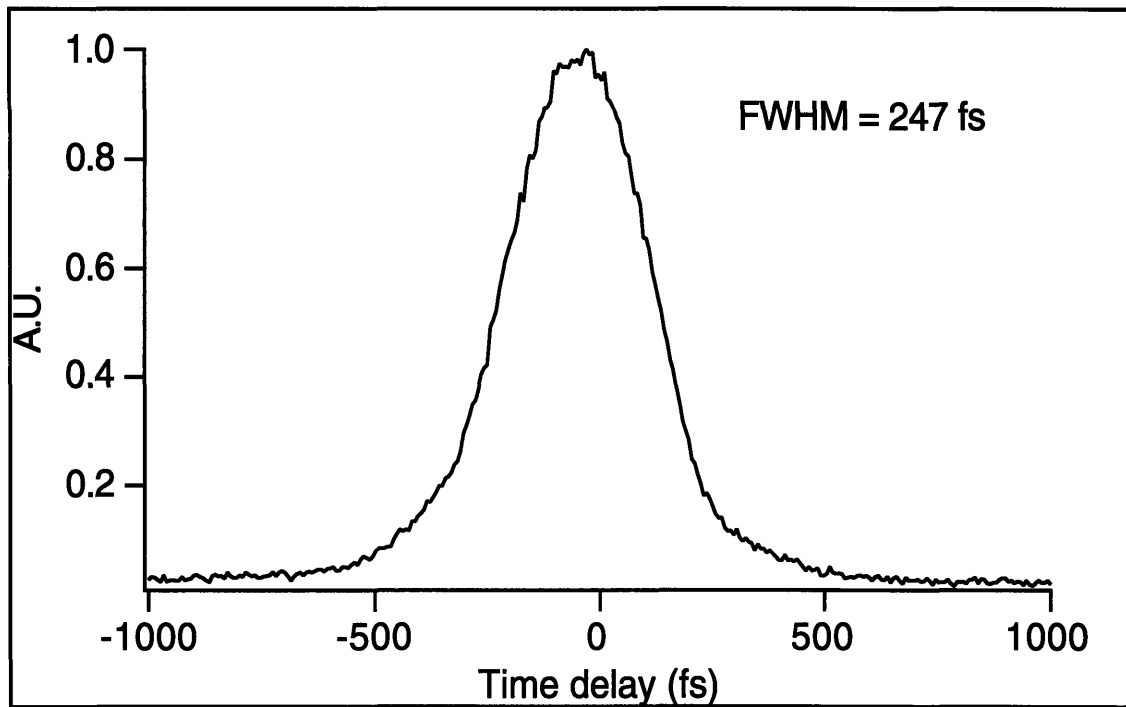
Figure 2.20: Spectral slicing of BK7 continuum. With this narrower bandwidth (24 nm) the pulses were longer (compare with Figure 2.21)

It was found that with all the materials that were tried for continuum generation, the spectral slicer could be adjusted to give some further pulse shortening, resulting in pulses as short as ~ 150 fs. This means that there are spectral regions in the continuum where the chirp is linear over the corresponding bandwidth. Figure 2.19 shows the effect of spectral
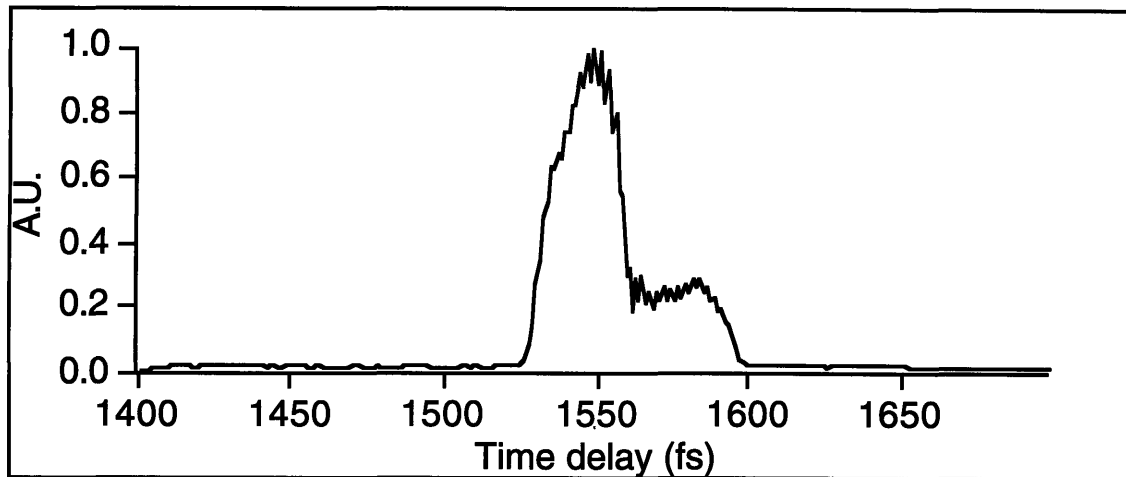
(a)
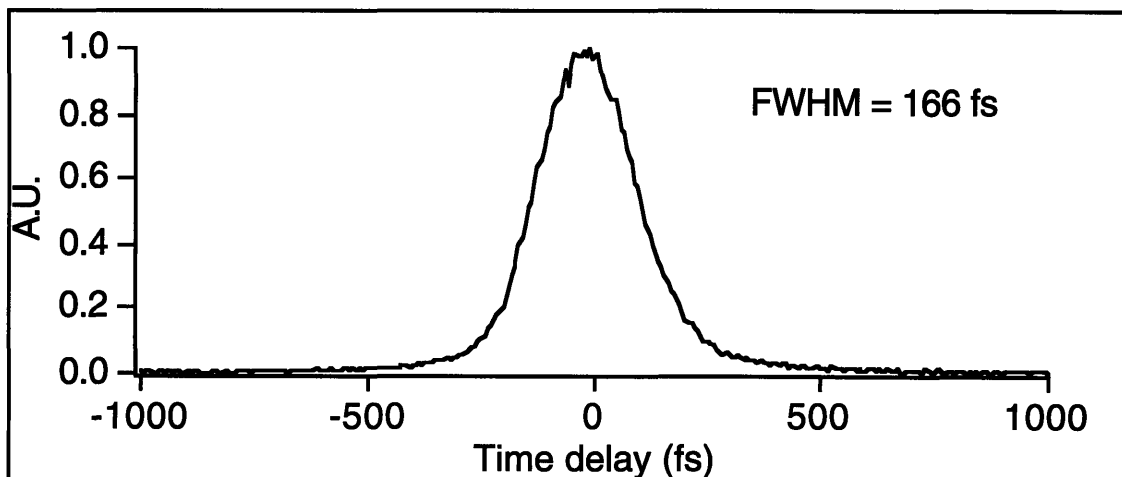
(b)

Figure 2.21: When the adjustable slit is opened further to increase the bandwidth of the spectral slice (a), the intensity autocorrelation width of that slice is reduced

slicing on the on the intensity autocorrelation. Here the continuum produced from SF56 glass is autocorrelated before and after spectral slicing. After spectral slicing the pulse is shorter and cleaner and indicates that some dispersion compensation was performed by the spectral slicer. Figure 2.20 and Figure 2.21 show the effect of different slit widths in the

slicer (i.e., spectral slices of different bandwidth) on the intensity autocorrelation, where the continuum was produced from BK7 glass. The larger bandwidth slice yields a cleaner shorter pulse.
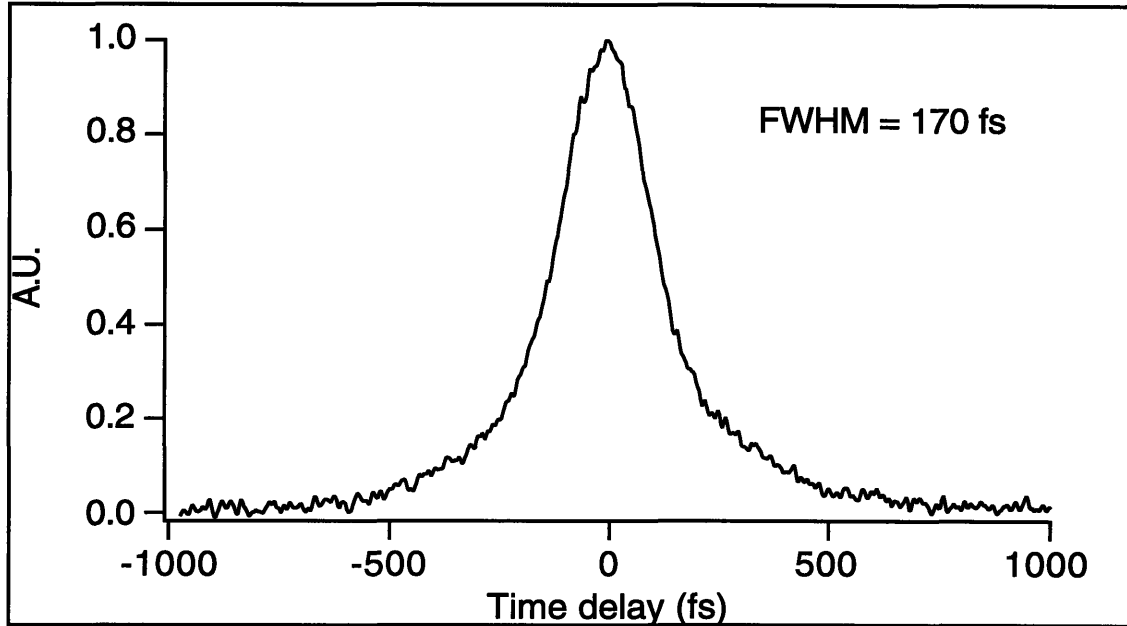
(a)
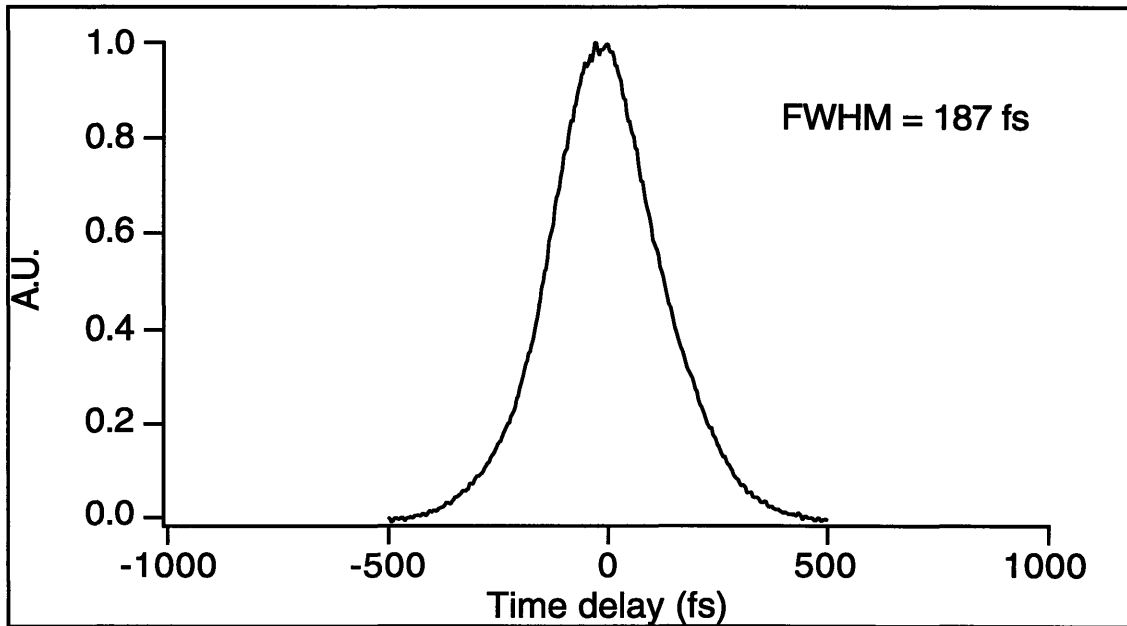
(b)

Figure 2.22: Intensity autocorrelations of spectral slices from continuum produced from (a) standard glass fiber and (b) ZnSe.

Figure 2.22 shows intensity autocorrelations of spectral slices from continuum generated from ZnSe and standard glass fiber. These too show that some dispersion compensation is possible in the slicer to yield spectrally filtered pulses with pulsewidths of ~ 150 fs. This also indicates that dispersion is present and important in the material generating the continuum and is producing linear chirp in excess of the linear chirp present before continuum generation. Spectral slices were easily taken from the region of 1470 nm to 1650 nm, where most of the energy is concentrated. In the case of broader continuum (e.g., continuum generated from ZnSe) spectral slices could also be taken from regions in the spectrum further away from 1500 nm.

Chapter 3

Nonlinear dynamic anisotropy in 1.5 μm semiconductor optical amplifiers

This chapter will describe the investigation of the nonlinear femtosecond response of a polarization-independent semiconductor optical amplifier. Although this device is designed for isotropic gain, it shows an induced dynamic anisotropy. Section 3.1 describes the heterodyne pump-probe technique, which allows polarization-resolved and time-resolved measurements of the nonlinear gain and nonlinear index, needed to characterize the induced anisotropy. Section 3.2 details the experimental setup. Section 3.3 discusses the device: its principle of operation, structure and polarization selection rules. Section 3.4 presents theoretical calculations to better understand and interpret the experimental results. In particular, it is found that the measurement is sensitive primarily to the hole dynamics, and, based on a k•p band structure calculation, that the holes in the two different well types have very different masses. The dynamics of the hole distributions in the different wells are therefore expected to be different. Section 3.5 presents some related experimental and theoretical results pertaining to these devices. Section 3.6 describes the experimental results, including the observation of the dynamic anisotropy in the gain and index response. Finally, section 3.7 describes a new experimental technique for measuring the induced anisotropy directly, and the results of this measurement.

3.1 The pump-probe technique

3.1.1 Pump-probe experiments on semiconductor devices

Pump-probe experiments provide one of the best ways to study optical nonlinearities in materials and devices. Essentially, the optical pump beam sets up a nonlinear polarization

(typically a second or third order polarization) and the optical probe beam interacts with this polarization. By examining the change in the probe induced by the pump, information may be extracted regarding the nonlinearity in the material or device. Although this type of experiment may be performed with CW radiation, it is then inherently limited to low peak powers and therefore will set up relatively small nonlinear polarizations for the probe to interact with. This will lead to low signal to noise ratio and reduced sensitivity of the measurement. By going to ultrafast pump-probe experiments the peak power is increased by the inverse of the duty cycle (i.e., period of the pulse train over pulsewidth) relative to CW. In the present case of a 100 MHz pulse train of 100 fs pulses this translates to a factor of 10^5 (for an instantaneous nonlinearity like the Kerr effect). An added advantage is the ability to time-resolve the nonlinear response of the material or device under test.

Pump-probe experiments may be performed in a reflection or transmission geometry, but since the present experiment deals with semiconductor devices, the transmission geometry is chosen to enhance the measured signal through interaction length. In particular, the devices are active waveguides where the whole length of the device contributes to the nonlinear signal. This is not the case when pump-probing a bulk sample. If , for example the nonlinear refractive index (n_2, a third order nonlinearity) is measured, the quantity of interest is the nonlinear phase accumulated by the probe and may be written:

$$
\begin{aligned}
\phi_{NL} &= \frac{2\pi}{\lambda} n_2 \int_{-L/2}^{L/2} I(z)dz = \frac{2\pi}{\lambda} n_2 \int_{-L/2}^{L/2} \frac{P}{\pi\omega_0^2\left(1+\left(z/z_0\right)^2\right)} dz = \\
&\frac{2\pi}{\lambda} n_2 \frac{z_0}{\pi\omega_0^2} \int_{-L/2z_0}^{L/2z_0} \frac{P}{\left(1+x^2\right)} dx = 2\frac{2\pi}{\lambda^2} P n_0 n_2 \tan^{-1}\frac{L}{2z_0}
\end{aligned}
\tag{3.1}
$$

where λ is the free space wavelength, I is the peak intensity, L is the sample thickness, P is the peak power, ω_0 is the beam waist, z_0 is the confocal parameter in the material and n_0 is the linear refractive index. From the above expression two important points become obvious: 1) The signal is independent of spot size or how tight the focusing is. 2) By going from $L = 2z_0$ to $L = \infty$ only a factor of 2 is gained in signal, therefore the effective interaction length is $2z_0$. In the case of waveguiding in one dimension (i.e., a planar waveguide the results are slightly different:

52

$$\phi_{NL} = \frac{2\pi}{\lambda} n_2 \Gamma \int_{-L/2}^{L/2} \frac{P}{2d\omega_0 \sqrt{1+(z/z_0)^2}} dz = \frac{2\pi}{\lambda} n_2 \Gamma \frac{z_0}{2d\omega_0} P \int_{-L/2z_0}^{L/2z_0} \frac{dx}{\sqrt{1+x^2}} =$$

$$2\frac{2\pi^2}{\lambda^2} P n_0 n_2 \Gamma \frac{\omega_0}{2d} \sinh^{-1}\frac{L}{2z_0} \approx \frac{\pi^2}{\lambda^2} P n_0 n_2 \sinh^{-1}\frac{L}{2z_0}$$

(3.2)

here d is the waveguide thickness, Γ is the fill factor or the effective area of the beam that contributes to the nonlinear signal, and the rest of the symbols have their previous meaning. In the last step the approximation $\Gamma \approx d/2\omega_0$ was used. Here again the signal does not depend on the spot size. For $L = 2z_0$, $\sinh^{-1}1 \approx 0.88$, but for lengths much longer than this $\sinh^{-1}x \xrightarrow[x\to\infty]{} \ln(2x)$ and, for example, when $L = 20z_0$, $\sinh^{-1}10 \approx 3$. This means an improvement in signal by a factor of 3.4, but the diffraction of the beam in one of the dimensions will lead to an elliptical beam at the output with an ellipticity of approximately 10. So in this case, too, nothing is gained by making the interaction length much longer than the confocal parameter.

When waveguiding is present in two dimensions, the interaction length is the length of the waveguide. The ratio of the waveguide length to the confocal parameter corresponding to a waist with dimensions of the waveguide cross-section, can easily be 2 orders of magnitude or more. It is for this reason that waveguide configurations are well-suited for nonlinear optics experiments. The best results are achieved if the beam can be focused to the cross-sectional dimensions of the waveguide (i.e., $\Gamma \approx 1$). In the present experiment that is not the case; and, in fact, the fill factor is polarization dependent.

The main advantages of waveguides in general is the gain in effective interaction length and the spatial averaging over a single mode, but an added advantage of active waveguides is the possibility of establishing carrier populations in the conduction and valence band by means of electrical pumping (i.e., by supplying a current to the semiconductor diode). These carrier distributions can now be probed. In contrast, a passive device would require doping (establishing only one type of carrier population) or a three pulse experiment, where the first pulse establishes the carrier populations.

In order to perform pump-probe experiments, there has to be a means of distinguishing between the pump and the probe beams. In a non-collinear configuration this is trivial. However, pump-probing a relatively long waveguide implies a collinear configuration and distinguishing between the beams by spatial separation is not feasible. The simplest way to accomplish this in a waveguide configuration is by using two orthogonal polarizations for the pump and probe, and passing the beams at the output through a polarizer oriented to
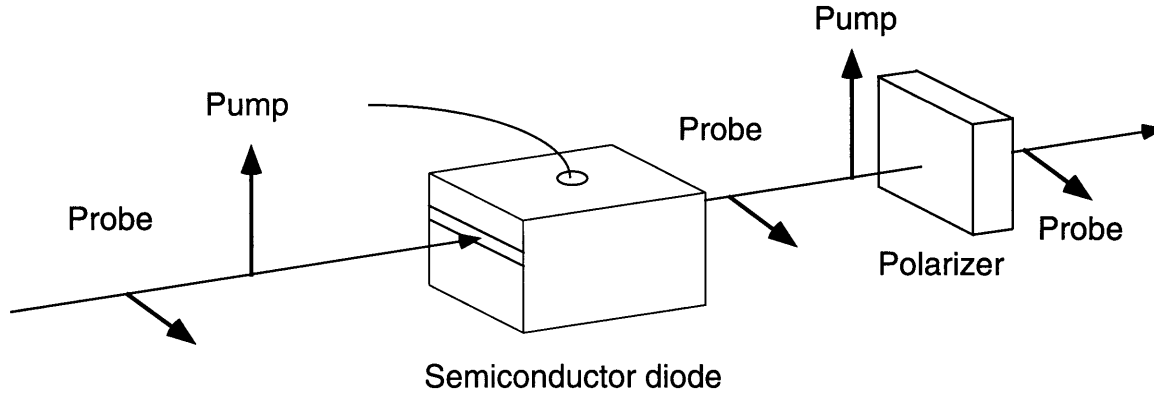
Figure 3.1:   Standard pump-probe configuration with cross-polarized pump and probe

reject the pump beam but pass the probe beam (see Figure 3.1). The main drawback of this method is that experiments that require copolarized pump and probe beams are not possible.

3.1.2 The heterodyne technique for nonlinear gain and index measurements

A way around this problem was devised recently [36] and is based on a scheme of "labeling" the pump and probe beams before they go through the device and is called heterodyne pump-probe for reasons which will become obvious. The basic idea is shown schematically in Figure 3.2. The "labeling" of the beams is accomplished by frequency upshifting the probe by a small amount relative to the carrier frequency (usually a RF frequency). In addition a third beam is generated from the original beam and is also up-shifted by a slightly different frequency and is called the heterodyne reference beam and it serves as a local oscillator. By beating the pump and probe beams with the heterodyne reference beam after the device, and detecting at the beat frequency of the probe and reference, the probe is distinguished from the pump. The pump and reference have a different beat frequency, to which the detector is not sensitive. For maximum signal the probe and heterodyne reference should be copolarized, but there is no restriction on the polarization of the pump relative to the probe.

It is important to realize that the pump and probe are pulse trains and therefore the optical spectrum of the pulses is the sampled spectral envelope of a single pulse (where the samples are separated by the repetition rate of the pulse train). When one of the beams is upshifted in frequency relative to another beam, the beat signal will be a sum of all the pairs of spectral components of the pulses. If this were a single-shot experiment it would not work, since two optical spectra separated by an RF frequency would be indistinguishable
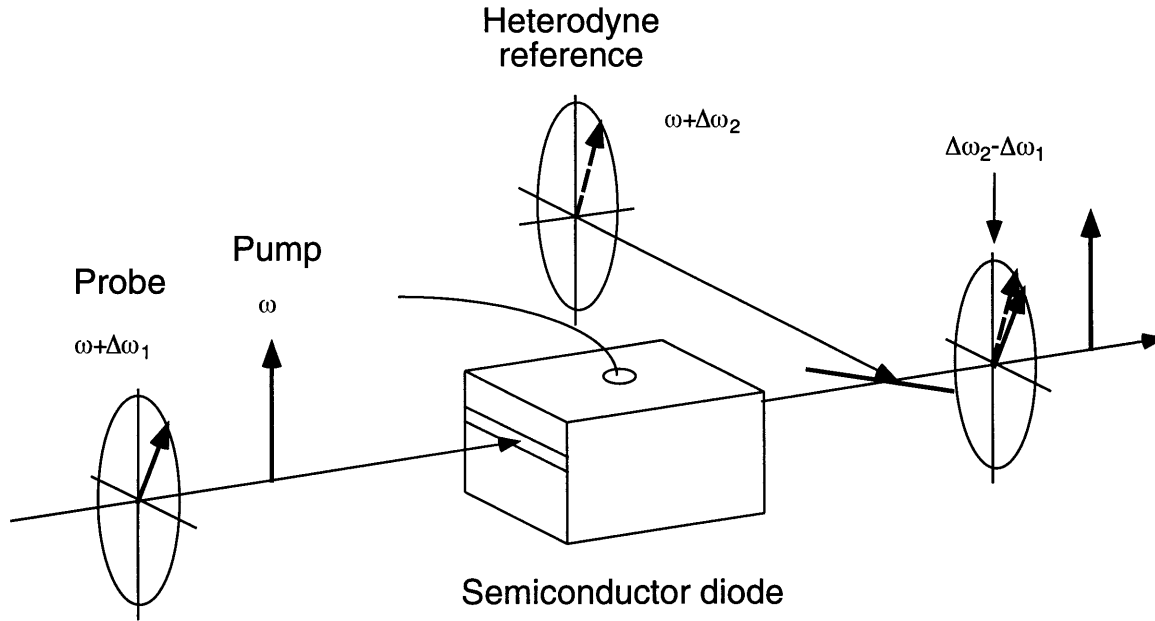
Figure 3.2: Schematic view of heterodyne pump-probe technique

for all practical purposes. In other words, averaging is essential for this experiment. It should also be noted that the required interference between probe and reference happens only when the two corresponding pulses overlap in time, i.e., within ~ 100 fs or equivalently within 30 μm. Finally, since this experiment is inherently phase sensitive, it offers the possibility of nonlinear phase measurements in addition to the nonlinear gain measurements. It also means that interferometric stability has to be maintained, which is easily accomplished in the electronics domain, by tracking the beat frequency in the RF receiver.

In previous experiments with this system the heterodyne reference was also sent through the device. This required sending the reference ahead in time, before the pump and the probe, so that any changes the reference pulse induced in the device would have decayed by the time the pump and probe reached the device. As a result an imbalanced interferometer had to be constructed after the device to make up for the time delay between probe and reference, making the temporal overlap of probe and reference possible. The reason for sending the reference through the device was that all pulses needed to see the same "environment", before being interferometrically recombined. In the present experiment it was found that sending the reference around the device (bypassing it) worked just as well. In fact, in many respects it is superior to the previous design. It does not require the imbalanced interferometer after the device and since the reference does not suffer

coupling losses into and out of the device, it is a much stronger local oscillator leading to a larger detected signal.

3.2 Experimental setup

3.2.1 The source

Figure 3.3 shows the experimental setup of the modified heterodyne pump-probe setup. The source for this experiment is a coupled-cavity APM $KCl:Tl^+$ color center laser [37] [38] [39]. The laser is synchronously pumped by an actively modelocked Nd:YAG laser with a repetition rate of 100 MHz and typical pulsewidths of 100-200 ps. The synch-pumped pulses from the main cavity of the color center laser are typically 20-30 ps long. Because of the spectrally broad gain curve, the output may be tuned from about 1.45 μm to 1.57 μm by means of a birefringent tuning plate. Since the cavity lengths of the pump laser and the color center are matched their repetition rates are similar.

The coupled APM cavity is matched in length to the main cavity and contains a 40 cm piece of dispersion-shifted fiber as the nonlinear element [38]. In dispersion-shifted fiber the effective core area is smaller that in standard fiber (~ 35 μm^2 vs. 50-80 μm^2 [1]) which leads to an enhanced nonlinearity through higher intensity in the fiber. Using $n_2 = 2.6 \times 10^{-16}$ [40], the free-space wavelength $\lambda = 1.51$ μm, the effective area $A_{eff} = 35$ μm^2, and the fiber length $L = 40$ cm, we get a nonlinear coefficient of ~ 2.5 kW^{-1} for one roundtrip through the fiber. So for about 1.3 kW peak power in the fiber a nonlinear π phase can be accumulated in one roundtrip. Typical pulsewidths from the APM laser are 120-150 fs long, so that typical pulse energies required for a nonlinear π phase shift are 0.15-0.2 nJ per pulse in the fiber. With coupling losses of about 35% this leads to about 0.3 nJ or 30 mW (assuming the 100 MHz repetition rate) in the coupled APM cavity. This is easily achieved with the $KCl:Tl^+$ color center laser which typically puts out 150-300 mW average power.

Active stabilization by means of a piezoelectric transducer (PZT) glued to the fiber, is used for keeping the cavity lengths matched to within a fraction of a wavelength. The PZT is controlled by an electronic feedback circuit [41], which tries to follow the average power coming back from the fiber. Wavelength tuning is more limited when the laser is operating in APM mode, typically from about 1.49 to 1.52 μm. A recent novel birefringent tuning plate [42] allows some more degrees of freedom in the tuning characteristics. This plate is designed to suffer no degradation in rejection ratio when going to higher orders, which are associated with narrower bandwidth. This results in a practical variable bandwidth tuning

56
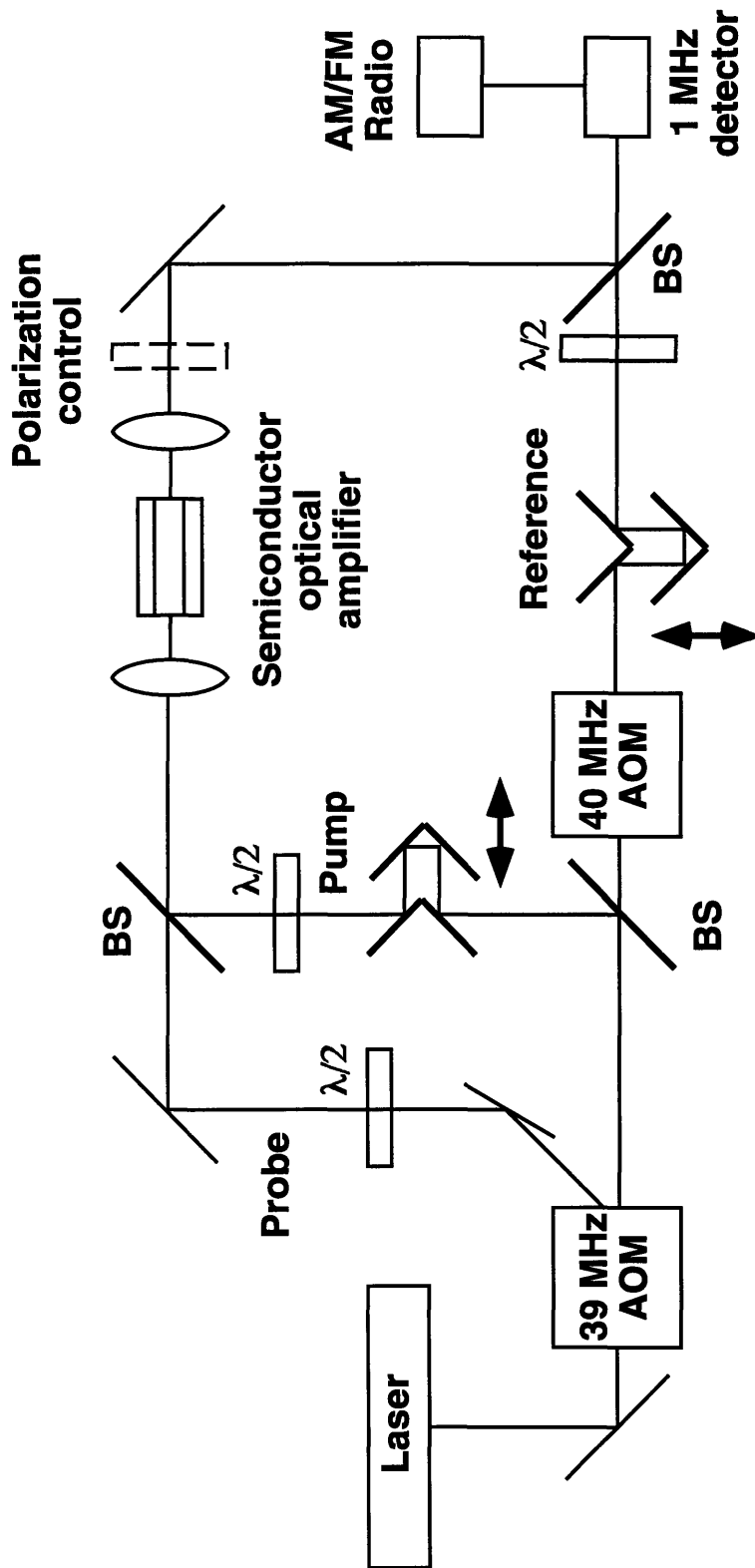
Figure 3.3: Experimental setup of the heterodyne pump-probe system. AOM = Acousto-optic modulator, BS = Beamsplitter.

filter. The lower orders can support shorter pulses but are not quite as tunable (the pulse width tends to broaden quickly when tuning away from the central wavelength of about 1.51 µm). The higher orders yield longer but more tunable pulses. The ability to control
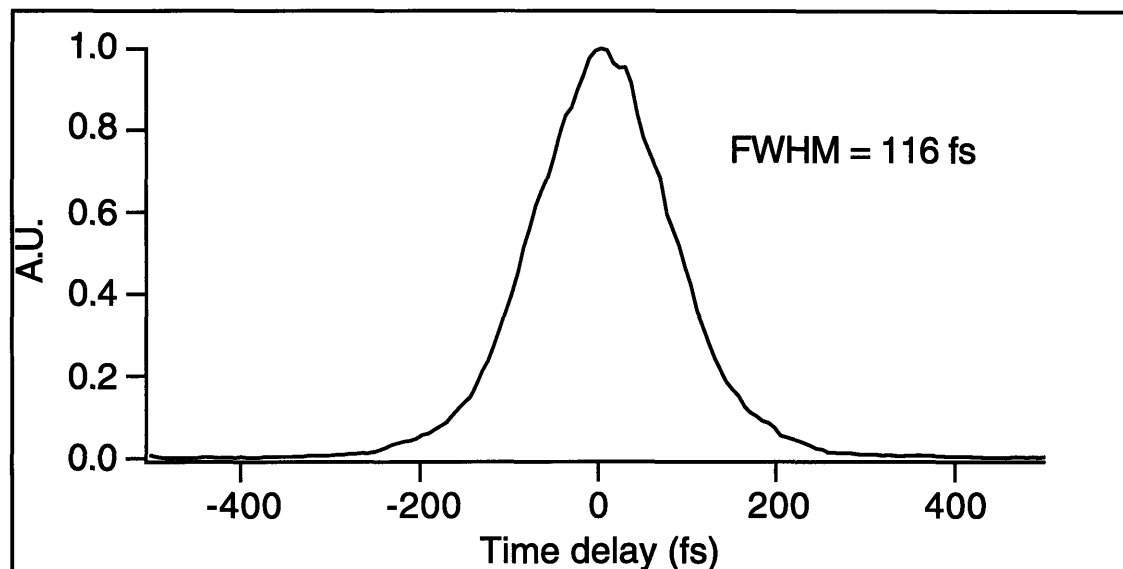
(a)
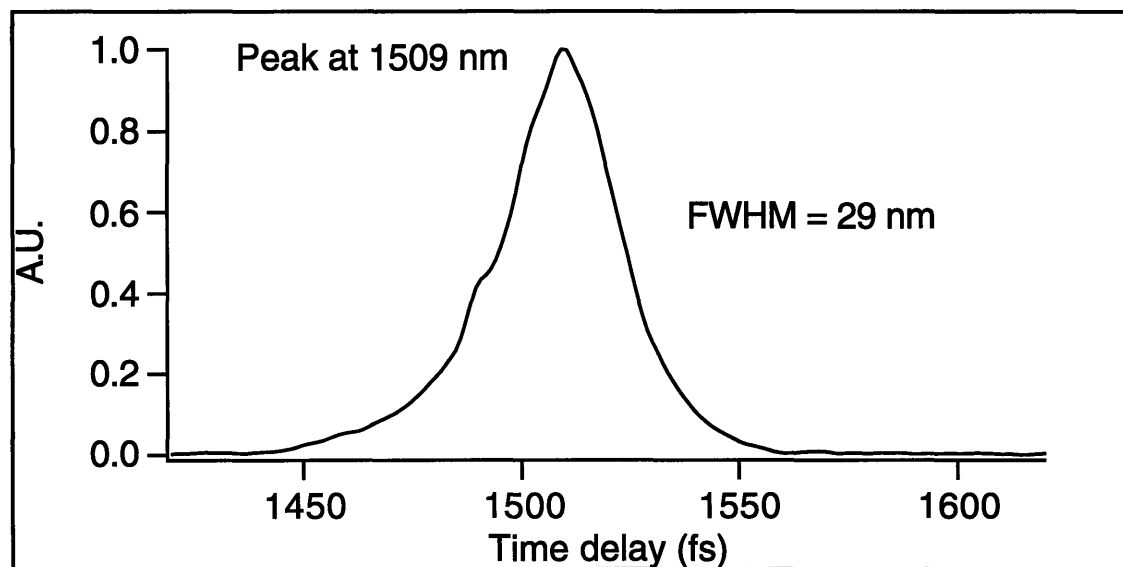
(b)

Figure 3.4: Typical intensity autocorrelation (a) and corresponding optical spectrum (b) of pulses used in the pump-probe experiment.

the pulsewidth to some extent can be very useful for some experiments. A typical intensity autocorrelation and corresponding optical spectrum are shown in Figure 3.4. The time-bandwidth product is typically 1.1-1.3 times the transform limit assuming sech pulses, indicating low chirp.

3.2.2 The pump, probe and reference beams setup

The probe and reference beams are generated from the diffracted (diffraction efficiency ~ 20 %) and upshifted pulse train at the output of traveling wave acousto-optic modulators (AOM's). The probe beam is generated by a 39 MHz AOM and the reference beam from a 40 MHz AOM. It should be noted that dispersion in the reference generating AOM is not an issue, since the reference pulse does not limit the time resolution of the experiment, it only plays the role of the local oscillator. However, dispersion in the probe generating AOM will broaden the probe pulse and degrade the temporal resolution of the experiment. In the present experiment, when using pulses of no less than 120 fs, this broadening is negligible. If the pump is assumed to have spectral components at multiples of 100 MHz (the repetition rate of the laser), the different possible beat frequencies will be at 1, 39, 40, 60, 61 and 99 MHz (and at any of these frequencies plus an integral multiple of 100 MHz).

As can be seen in Figure 3.3 the reference bypasses the device and gets recombined with the transmitted pump and probe after the device using a beamsplitter. Once the reference and probe are combined after the beamsplitter they are coupled into a fiber before the detector, which insures collinearity and the absence of spatial fringes on the detector. An adjustable time delay in the reference arm is used to temporally overlap the reference and the probe. Effectively, the reference and probe beams are two arms of a rather large Mach-Zehnder interferometer. It should be noted that changing the pump current to the device will change the linear refractive index and therefore the optical length of the probe arm. By small adjustments to the reference arm path length, this mismatch is compensated.

3.2.3 The detection system

To select out the beat frequency of interest at 1 MHz and discriminate against the rest, a tuned detector was built. The detector is a resonant circuit with an adjustable inductor (to allow fine tuning to 1 MHz) and gives a narrowband (~50 kHz) filter around 1 MHz. The rolloff is at 40 dB/decade, so that at 39 and 40 MHz the transmission of the filter is down by more than 3 orders of magnitude. The transimpedance gain is about 2 kΩ, so that 1 mA of current would show up as a 2 V signal at the output. The detected signal is fed into the antenna input of a HAM radio which is tuned to 1 MHz. When either the probe or the ref-

erence are chopped at audio frequencies, the audio output and a speaker can be used to "listen to the data".

The pump induces amplitude (or gain) changes as well as phase (or index) changes, so that the probe carries on it amplitude modulation as well as phase changes. As mentioned earlier, since this is a phase sensitive measurement the phase modulation can be recovered with no further changes to the setup. By using AM reception in the radio the amplitude changes are directly measured and by using FM reception the instantaneous frequency is directly measured. Since mechanical chopping in conjunction with lock-in detection is always employed for improving the signal to noise ratio, the output of the radio is fed into a lock-in amplifier. The input is mixed down with the chopper reference frequency and low pass filtered (i.e. time integrated). The integration of the measured FM signal is exactly the phase modulated signal. As mentioned earlier, interferometric stability is maintained by the receiver, which can easily track slow drifts.

3.2.4 Calibration (measuring absolute numbers)

When measuring gain changes, the probe may be chopped to calibrate the absolute transmission change. By measuring the signal before the pump arrives, the linear transmission is measured. Subsequent measurements (typically, with chopped pump which is a background-free measurement) are referred to this transmission level. When measuring phase changes, the calibration is less trivial since a phase reference is needed [43]. To this end, the mirror at one of the corners of the Mach-Zehnder interferometer was mounted on a PZT (see Figure 3.3). Prior to using it in the experiment it was mounted in a balanced Michelson interferometer and calibrated. By ramping the PZT (with a triangle wave) with a variable voltage and observing the interference signal on an oscilloscope, it was found what voltage corresponded to a π phase shift (at that point the interference signal switches polarity). Once this calibration is complete, the PZT is placed in the heterodyne system and the pump is blocked. The PZT is driven with the π voltage and the signal is detected (using the PZT driver as a lock-in reference), so that at this point the lock-in voltage reading corresponds to a phase shift π. Subsequent measurements and the corresponding lock-in voltage will be referenced to this level.

3.2.5 Polarization control

Polarization control in the experimental setup is achieved by using a $\lambda/2$ waveplates in all 3 beams, making possible all linear polarizations for all the beams. The polarization control section in Figure 3.3 is used for making the generally elliptic polarization at the output of the diode, a linear polarization. This is important for the direct anisotropy meas-

60

urement to be discussed later. A λ/4 waveplate properly oriented can transform an arbitrary elliptically polarized beam to a linearly polarized beam. An additional λ/2 waveplate can transform an arbitrary linearly polarized beam into any specific linear polarization.

3.2.6 Coupling into the device

Finally, the device itself is electrically pumped by a current source which can be incremented by 1 mA steps. The light is coupled into the device by means of a fiber lens at the end of a short piece of dispersion-shifted fiber, which automatically ensures collinear pump and probe and the absence of any spatial interference effects at the input facet of the device. Because the device was active, it was easy to align the fiber at the input, by back-coupling the ASE out of the device. The device which was investigated had optical windows on both facets (see next section), so that the gain region was recessed relative to the input facet. The standard fiber lenses did not have the appropriate working distance, and therefore a specially designed fiber lens micro-lathed with a laser was employed [44].

3.3 The polarization insensitive semiconductor optical amplifier (PI-SOA)

3.3.1 General characteristics

In general it is very difficult to control the state of polarization at the output of a fiber and so it is typically arbitrary. On the other hand standard SOA's supply gain predominantly to one linear polarization - either parallel to the layers of the device (TE) or perpendicular to them (TM). In fact the majority of double heterostructure bulk and multiple quantum well (MQW) devices supply gain to TE polarized light. Only in tensile-strained MQW is there a possibility of making a device with TM gain. This means that the light at the fiber output needs to have its polarization transformed to TE (or TM), otherwise the amplification will not be efficient (in the worst case there will be no amplification). This in turn means that in order to be able to integrate these SOA's into optical communication systems, either a polarization controller has to be integrated just before the SOA or the SOA must be made isotropic supplying equal gain to all polarization states. This is the motivation behind the PI-SOA's.

3.3.2 Polarization selection rules - introduction

In bulk and unstrained MQW devices as well as compressive strained MQW devices, the main radiative transitions are between the conduction band and the heavy hole band, near the Brillouin zone center. These transitions are TM forbidden (strictly speaking this true only in the zone center, but is still approximately true close to the zone center). With

61

TENSILE AMPLIFIER (4T)
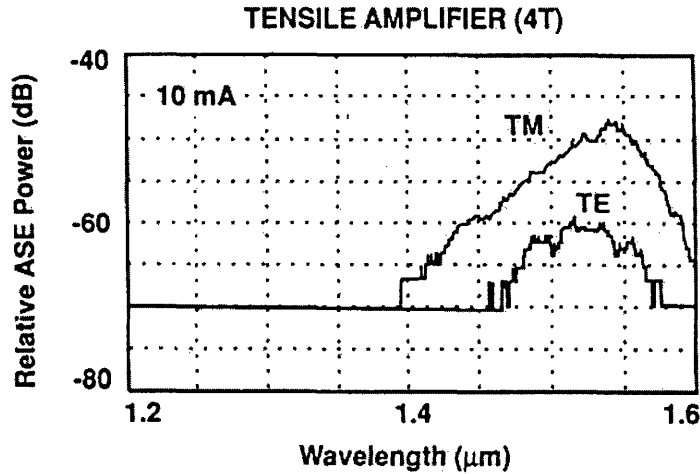
Figure 3.5:   ASE spectrum of a tensile strain MQW SOA (from ref. 47)

proper tensile strain the light hole band may be moved higher in energy relative to the heavy hole band such that the main radiative transitions are between the conduction band and the light hole band. In this case both polarizations are allowed, but TM is 4 times more likely than TE; or, in other words, the matrix element for a transition involving TM polarized light is 4 times larger than one involving TE polarized light. A device containing such tensile-strained QW's in the active region would supply gain mainly to TM polarized light, as mentioned before. The predominantly TM amplified spontaneous emission (ASE) spectrum of such a 4 QW tensile strained device is shown in Figure 3.5.

3.3.3 Mixed-strain quantum wells

By mixing compressive and tensile strained wells in the active region and tailoring the structure parameters, the gain for TE and TM polarized light may be made almost equal and therefore making the device isotropic. It should be remembered that making the gain isotropic involves more than just the quantum mechanical selection rules. The effective small signal gain coefficient is $g = \Gamma g'(N)N$ where $g' = dg/dN$ is the differential gain, Γ is the confinement factor of the waveguide and N is the carrier density. The differential gain is the semiconductor equivalent of the cross-section of the transition and contains the quantum mechanical matrix element or transition strength. It also is a function of the carrier density N. The carrier density at a given energy depends on the density of states. Finally, since the device is a waveguide only the waveguiding region will contribute gain, so only the fraction of the optical mode overlapping with the active part of the waveguide, Γ, will experience gain. This confinement factor is different for TE and TM polarized light. So to

TENSILE / COMPRESSIVE AMPLIFIER (3T/3C)
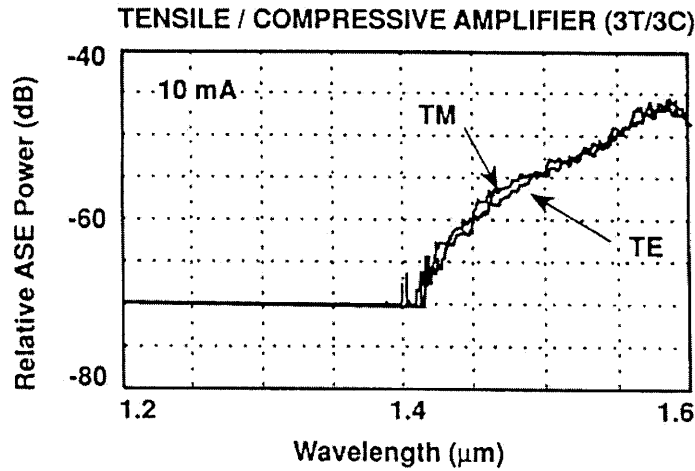
Figure 3.6:   ASE spectrum from a mixed strain SOA. The TE and TM spectra are almost identical (from ref. 47)

make g equal for TE and TM, all these factor must be taken into account and the product $\Gamma g'N$ must be made equal for both polarizations.

Recently, such a PI-SOA device was demonstrated operating first at 1.3 μm [45] [46] and later at 1.5 μm [47]. The TE and TM ASE spectrum of the device described in ref. 47 is shown in Figure 3.6 and are equal to within 1-2 dB.   A more recent variation of the device also operating at 1.5 μm demonstrated superior gain isotropy (< 1 dB gain difference over the bandwidth of operation) [48].   All of these experiments were performed in the regime where the amplifier was linear well away from saturation.   In the experiments described here, the gain and index were investigated in the large signal, or nonlinear, regime, on a femtosecond timescale.

3.3.4 Structure

The device used in the present experiment was identical to the one described in ref. 47. The device contained 3 pairs of alternating compressive and tensile strained quantum wells. The wells were InGaAs wells with -1% strain in the compressive wells and +1% strain in the tensile wells (relative to InP).   The barriers between the wells were nominally un-strained InGaAsP lattice matched to InP.   The compressive well thickness was 35 Å and the tensile well was 160 Å with barrier thickness of 100 Å.   The reason for the different thickness of the wells is the following: tensile strain causes an increase in bandgap as does quantum confinement, but compressive strain causes a decrease in the bandgap.   To tailor
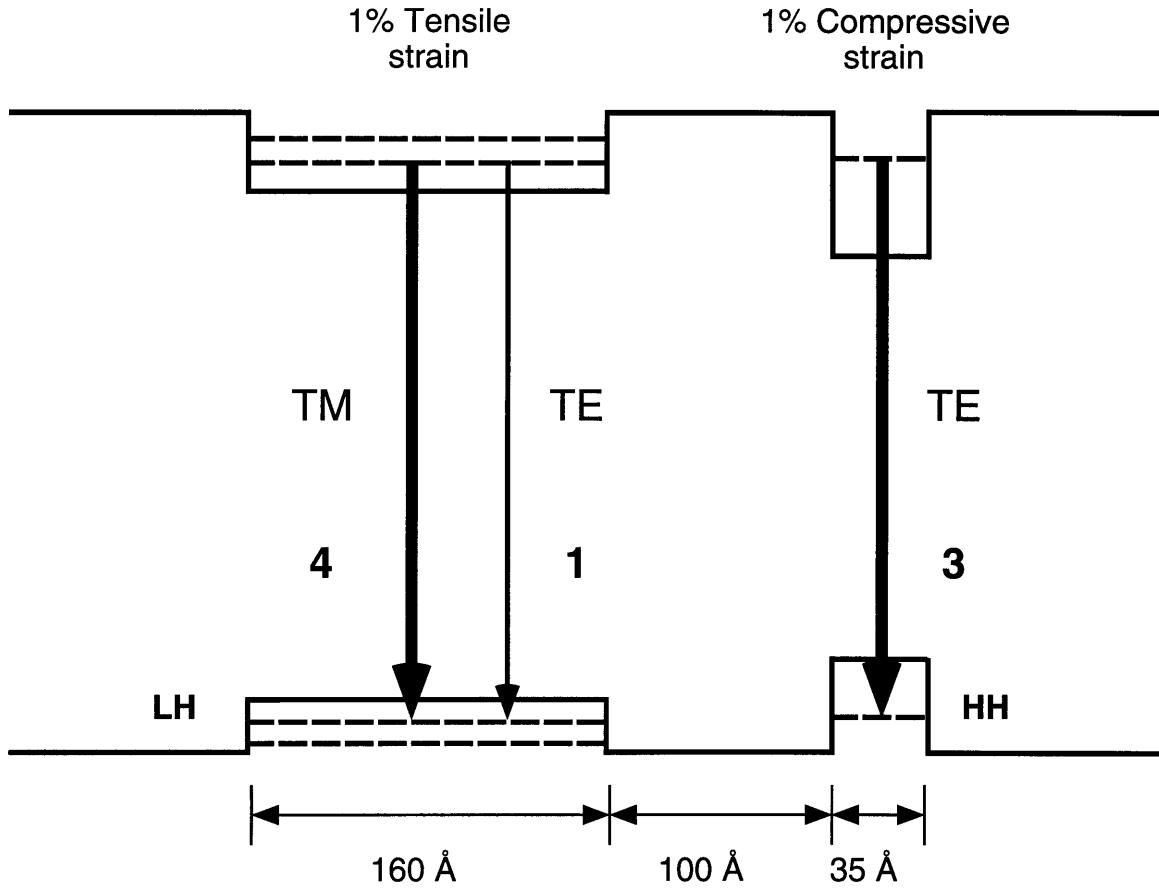
Figure 3.7: Schematic drawing of the device structure and the relative transition strengths for TE and TM polarized light in the two different QW's.

the transition energy to be the same in both wells, the compressive strained well was made very narrow to increase quantum confinement effects and offset the bandgap decrease due to the strain. This also allows another degree of freedom for balancing the gain for TE and TM polarized light. Further details of the growth and characteristics of the device are given in ref. 47. Figure 3.7 shows a schematic drawing of the device structure with the relative transition strengths for TE and TM in the compressive and tensile wells. It should be noted that the well depths are different too, because of the different strain-induced bandgap shifts.

3.3.5 polarization selection rules revisited

To understand the origin of the polarization selection rules, the wavefunctions of the conduction and valence band carriers have to be examined. In the $k \cdot p$ theory (including spin-orbit interaction), it can be shown that the Brillouin zone center wavefunctions of the 2 conduction states (including spin) and the 6 valence states are orthogonal. Furthermore,

the conduction states are similar to atomic s orbitals (spherically symmetric) and the valence states are linear combinations of states similar to atomic p orbitals ("dumbbells") [49]. The usual notation for these states are $|S\alpha\rangle$, $|X\alpha\rangle$, $|Y\alpha\rangle$, $|Z\alpha\rangle$ where $\alpha =\uparrow$ or $\downarrow$ for the two different spins. The heavy hole zone center states are a linear combinations of $|X\alpha\rangle$ and $|Y\alpha\rangle$ only, whereas the light hole zone center states are linear combinations of all three p-like functions.

The matrix element governing radiative transitions is proportional to the dot product of the light polarization and the momentum matrix element:

$$\hat{\varepsilon} \bullet \langle m|\vec{p}|n \rangle \tag{3.3}$$

where $\hat{\varepsilon}$ is the polarization unit vector, m and n are one of the above 4 functions and $\vec{p}$ is the momentum. The only non-zero momentum matrix elements are of the form $\langle S|p_i|I \rangle$ where $i = x,\ y,\ z$. So in the case of the zone center heavy hole state the only non-zero momentum matrix elements are $\langle S|p_x|X \rangle$ and $\langle S|p_y|Y \rangle$. In both cases the dot product with a unit vector in the z direction (corresponding to TM polarization) is identically zero. This why TM transitions between conduction band and heavy hole band are forbidden. Away from zone enter the valence bands couple to each other and mix, i.e., they are no longer orthogonal. The heavy hole band may then acquire some light hole character and in particular acquire some fraction of the $|Z\rangle$ function. In this case the TM transition is no longer strictly forbidden. The transition strength depends on the fraction or amplitude of the different p-like components in the valence band state [50]. The relative transition strengths shown in Figure 3.7 were derived in this way (they are proportional to the square of the above matrix element). These results hold for both bulk and QW's at the Brillouin zone center. Recently, a universal curve for the transition strength in QW's (in the infinite well limit) away from the zone center was derived theoretically [51] and gives some analytical results for the strongly bound states in QW's. However, close to the zone center where most of the carriers reside there are no large changes in the transition strengths.

These selection rules offer a unique opportunity to study the femtosecond dynamics of interwell coupling in the mixed strain devices. If the pump pulse is linearly polarized (TE or TM), it will excite predominantly one set of wells. By probing with the orthogonal polarization the measurement is predominantly sensitive to the other set of wells. Any coupling (via tunneling) or transfer (via thermionic emission, diffusion across the barrier and recapture) between the two different sets of wells, should show up in this pump-probe

measurement. The departure from the ideal experiment is due to the fact that the tensile well is sensitive to some extent to TE light, and also because the carriers away from the zone center are not in a purely heavy hole or light hole state.

3.4 Theoretical investigation of the device

3.4.1 Fermi level calculations

It has been pointed out recently that typical MQW SOA's under normal electrical pumping, have a quasi-Fermi level significantly higher than the quantum barriers [52]. This implies that the QW's in the conduction band are "full". In the valence band the density of states is much higher and therefore it is not as easy to fill the QW's. The calculation of this quasi-Fermi level is based on integrating the 2D density of states (times the Fermi factor) from the bound level energy up to the barrier energy and adding the integral of the 3D density of states (times the Fermi factor) from the bottom of the barrier. The sum
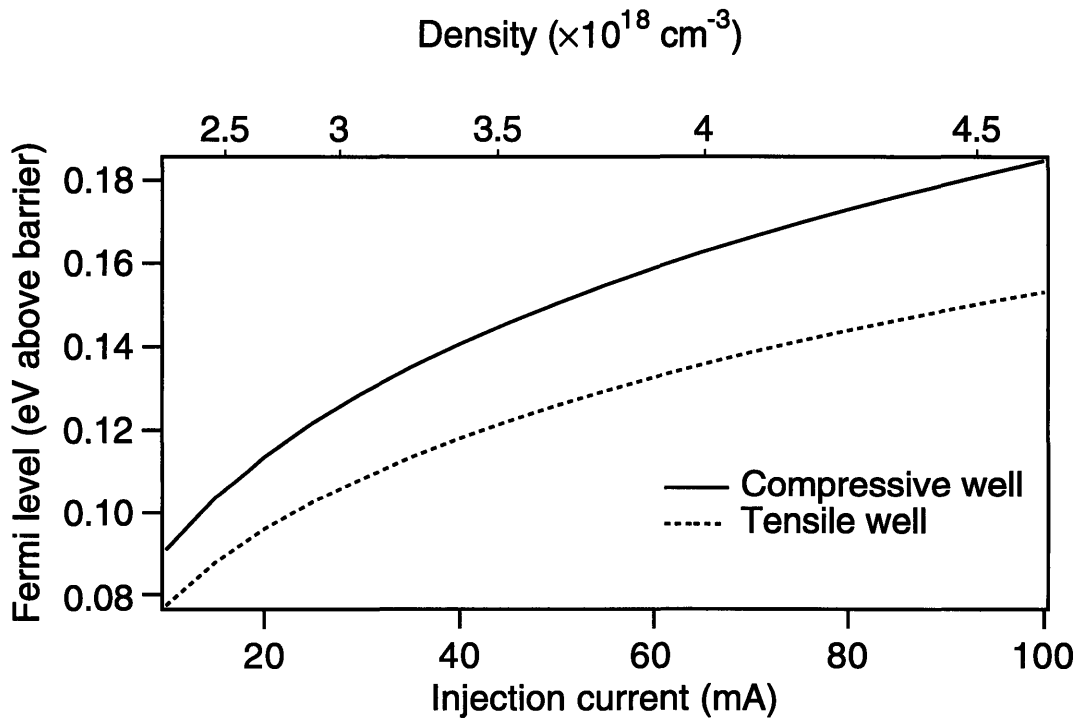
Figure 3.8: Electron quasi-Fermi level as a function of injection current (bottom axis) or carrier density (top axis), for the compressive well (solid line) and the tensile well (dashed line).

has to equal the carrier density in the well region. The total carrier density can be derived from the injection current and the recombination time, which is also carrier density dependent.

For the device used in our experiments it was found that the recombination time is mainly governed by Auger processes [53]. In this case the carrier density is given by:

$$N = \left(\frac{I}{qVC}\right)^{1/3}$$ (3.4)

where I is the injection current, q is the electron charge, V is the active volume and C is the Auger coefficient (on the order of 10^{-29} cm^6/s). For a given current the corresponding electron density was calculated using the above expression. The integration described above was then performed by varying the quasi-Fermi level until the result was equal to the electron density. Figure 3.8 shows the result of the calculation for our device. The quasi-Fermi level is shown (relative to the barrier) as a function of injection current, for the compressive and tensile wells. The experiments were performed at a central wavelength of 1.51 μm. At this wavelength 33-34 mA corresponds to transparency and 28 mA is deep into the absorption regime. It is therefore obvious from the figure that for any injection current in this experiment, the quasi-Fermi level for electrons will indeed be high in the barrier and the QW conduction band will be full. Most of the changes in the distribution, for example due to carrier heating, are most distinct near the Fermi energy. However, the probe is close to the bound levels in the QW and therefore is not sensitive to changes near the Fermi level. This implies that our experiments are not sensitive to electron dynamics, and most of the dynamics that will be measured will be due to holes.

3.4.2 Band structure k•p calculations

Since the holes govern most of the dynamics of these devices, it is necessary to examine the valence band more closely, in particular, the dispersion of the heavy and light hole bands and the corresponding effective masses in the two types of QW's. The k•p theory is well suited for this sort of calculation, since it is a good approximation near high-symmetry points such as the Brillouin zone center. Following the Kane model [49] the subset of the two conduction bands and six valence bands are treated exactly, with the effect of higher lying bands lumped into empirical constants such as the Luttinger parameters [54]. These higher lying bands are essential and cannot be neglected since without taking them into account the heavy hole band is dispersionless. A further simplification is achieved by

assuming the conduction band and the split-off band are far enough in energy from the heavy and light hole band, such that they are effectively decoupled from these bands and have parabolic shapes. The original 8×8 Hamiltonian is now block diagonal and only the 4×4 block corresponding to the two heavy hole bands and the two light hole bands (they are actually only 2 bands, each twice degenerate because of spin) is used in the calculations. This k•p formalism is now taken together with the envelope function approximation for QW's [55]. The wavefunctions are constructed in the well layers and barrier layers and are required to be continuous across the interfaces. Probability current conservation also requires that $m(z)^{-1} d\psi/dz$ be continuous across the interfaces (here m is the effective mass, ψ is the wavefunction and z is the direction perpendicular to the QW layer. When these boundary conditions are imposed, a huge determinantal equation is constructed and solved for the eigenenergy. This procedure must be repeated for each point of interest in k-space. In these calculations we neglect the anisotropy of the masses in the plane of the QW, which is justified since the Luttinger parameters γ_2 and γ_3 are approximately equal in each region and may be replaced by their average (also known as the axial approximation) [56]. This means that only one direction in k-space must be examined. Finally, we neglect the coupling between the wells and treat each well with finite barrier height, but infinite spatial extent. This is justified since the heavy holes extend very little into the barriers (much less than the 100 Å barrier thickness). Also the levels closest in energy in the two wells are approximately orthogonal states (light hole levels in one well are approximately lined up with heavy holes in the neighboring wells) and the coupling is therefore negligible. This argument will have important consequences for the possibility of hole tunneling. The calculations that were performed follow closely ref. 57, but may be implemented in many other ways [58] [59] [60].

At this point a few words should be said on the effects of strain on band structure. Strain, even in bulk, breaks spatial symmetries because the direction in which the strain is applied makes one direction in space special. This symmetry breaking is accompanied by the lifting of degeneracies, as is well known from group theory [61]. In particular the heavy and light hole degeneracy at the zone center is lifted. The strain contains two components known as the hydrostatic component and the shear component. The hydrostatic component with its accompanying deformation potential results from the physical change of the primitive cell volume and is responsible for a static shift in the bandgap. The shear component (with its corresponding deformation potential) is responsible for the splitting between heavy and light hole states [62]. It should also be noted that to support coherent strain in a layer (i.e., without causing dislocations), the layer thickness has to be under

some critical thickness, which can be derived in a number of ways [63]. This is an important consideration for strained-layer QW devices, since dislocations lead to rapid degradation in the operation of these devices.

3.4.3 Limitations of the k•p calculation

Before presenting the results of this calculation some of its limitations should be discussed. There are a few parameters which are not known very well even experimentally. Two of the most important ones are: 1) the valence band offset (VBO) - how is the bandgap difference between two materials split between the conduction and valence band. 2) similarly, how does the hydrostatic bandgap shift (due to the strain) split between the conduction band and the valence band. This split is usually taken to be: all the shift in the conduction band, or 2/3 of the shift in the conduction band. The major approximation in the calculation leads to neglecting the influence of the conduction and split-off bands on the heavy and light hole bands. The modification in band structure due to the inclusion of the split-off band (i.e., going to a 6×6 Hamiltonian) was recently shown [64]. The dispersion of the bands is somewhat modified and the masses at the zone center may change by up to 30% (the split-off energy in the material of interest: $\Delta \approx 300$ meV). Obviously, higher lying levels in the QW will interact more strongly with the split-off band, since they will be closer in energy. Neglecting the coupling to the conduction band is usually justified, since the bandgap is close to 1 eV. However, it has been shown that strain contributes to such coupling [65]; and, as will be discussed later, intervalence band absorption (IVBA) is zero because of this approximation. Finally, these calculations (like most band structure calculations) are all in the one electron approximation and neglect many-body effects such as bandgap renormalization.

3.4.4 The results of the k•p calculation

The parameters used for the calculation are given in Table 3.1 and were mostly taken from ref. 66. The values for alloys were linearly interpolated between the constituent binary values. The VBO was taken to be 35% of the bandgap difference between the barrier and well material (before accounting for energy shifts due to strain). This number was derived from the transitivity condition [67]. This gave good results for the tensile well in terms of the transition energies, but was less satisfactory for the compressive well. This may be because the same VBO was used for both wells. Recently, a theoretical investigation of the VBO problem in strained-layer devices was undertaken, and showed that the final VBO (after accounting for strain-induced energy shifts) was about 40% [68]. More rigorous theoretical calculations for the VBO in general exist in the literature (see e.g., ref.

	Compressive strained quantum well	Tensile strained quantum well
Material	$In_{0.68}Ga_{0.32}As$	$In_{0.39}Ga_{0.61}As$
Bandgap (eV)	0.59	0.90
Barrier bandgap (eV)	0.95	0.95
VBO (%)	0.35	0.35
Lattice constant (Å)	5.9276	5.8101
Strain (%)	-1	+1
Stiffness constant C_{11} (dyn/cm^2)	9.48×10^{11}	10.51×10^{11}
Stiffness constant C_{12} (dyn/cm^2)	4.80×10^{11}	5.05×10^{11}
Hydrostatic deformation potential (eV)	-7.2	-8.3
Shear deformation potential (eV)	-1.8	-1.7
Hydrostatic shift (meV)	-71	86
Shear splitting (meV)	-36	34
width (Å)	35	160
Electron effective mass (well)	0.036	0.049
Electron effective mass (barrier)	0.058	0.058
Luttinger parameter γ_1 (well)	16.0	12.1
Luttinger parameter γ_2 (well)	6.3	4.5
Luttinger parameter γ_3 (well)	7.1	5.3
Luttinger parameter γ_1 (barrier)	11.7	11.7
Luttinger parameter γ_2 (barrier)	4.4	4.4
Luttinger parameter γ_3 (barrier)	5.2	5.2

Table 3.1:   Material parameters used for the k•p calculation

69), but were not used here. The splitting ratio of the hydrostatic shift was taken as 2/3 of the total shift in the conduction band.

Figure 3.9 and Figure 3.10 show band diagrams of the compressive and tensile wells. Note that the bottom of the heavy and light hole well are different, due to the shear component of the strain. The fundamental energy transition in the compressive well corresponds to 1.59 μm and in the tensile well to 1.53 μm. However, once carriers are injected these
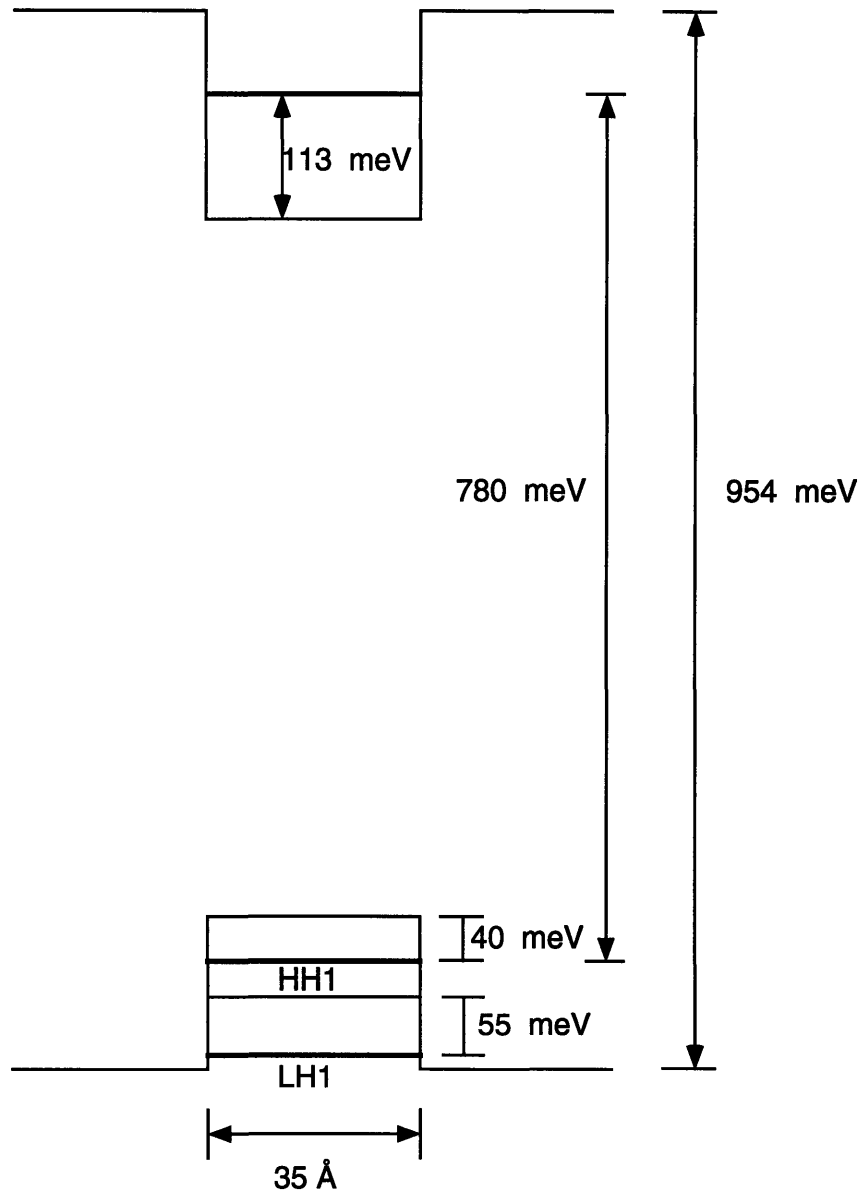
Figure 3.9: Band diagram of compressive well. The thick lines are the bound levels. The bottom of the light hole well is lower than the bottom of the heavy hole well, because of the strain.

may change, not necessarily in the same way, since the density of states in the two wells

are different. The uncertainty in the VBO mentioned earlier, may be another source for the discrepancy.

Figure 3.11 and Figure 3.12 show the calculated band structure for the compressive and tensile wells. The energy relative to the unstrained valence band edge is plotted as a
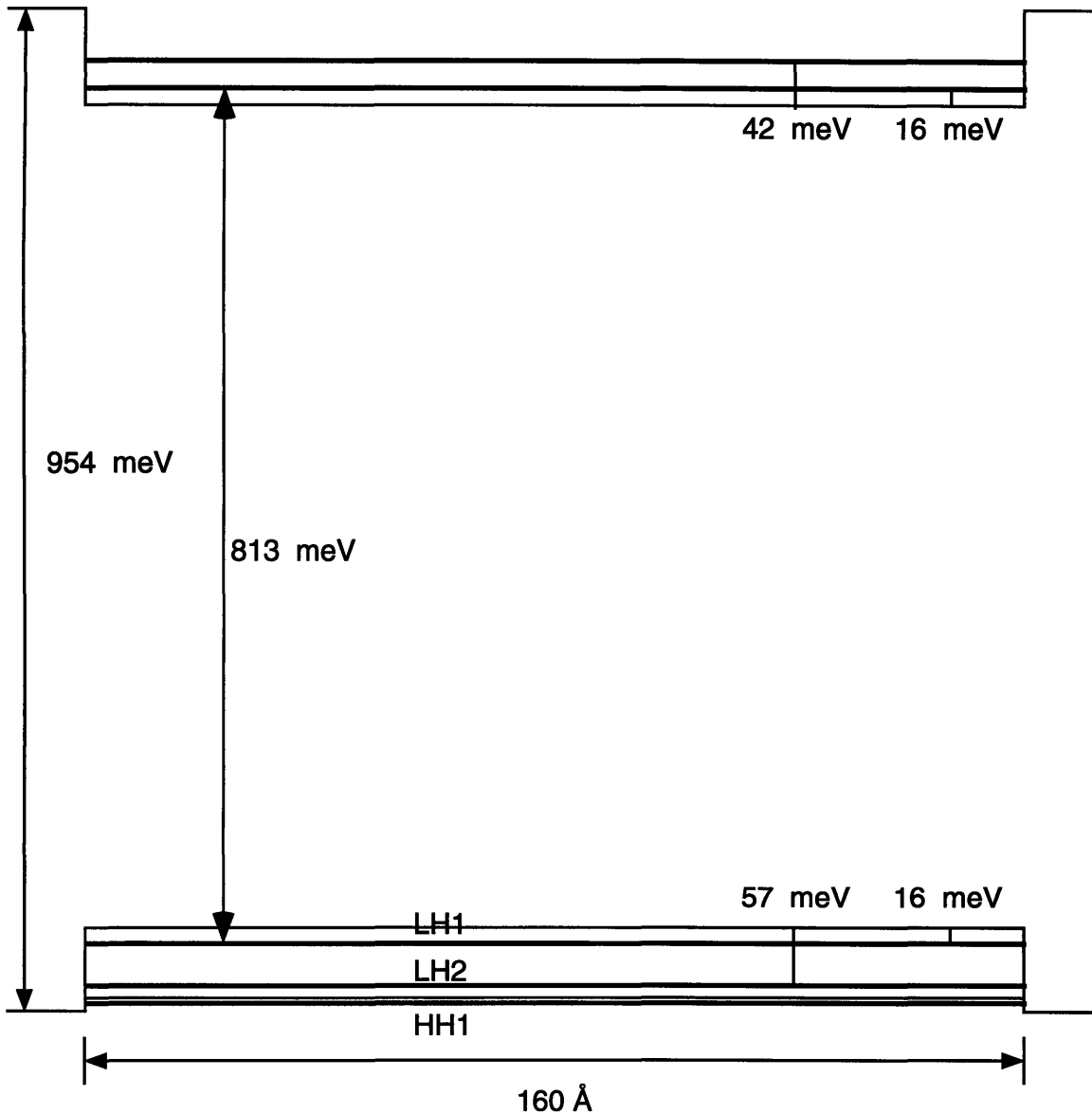
Figure 3.10: Band diagram of tensile well. The thick lines signify the bound levels. As in Figure 3.9, the bottom of the heavy and light hole wells are different due to the strain.

function of k. Three features are apparent in these results: 1) the light hole band is highest

in energy in the tensile well, but the heavy hole band is highest in the compressive well (as required for this device). 2) the valence bands undergo considerable warping (even to the extent that negative masses appear). 3) the curvature of the heavy hole band in the compressive well is much smaller that the curvature of the light hole band in the tensile well. Since the effective mass is proportional to the curvature of the bands through:

$$\frac{1}{m*} = \frac{1}{\hbar^2}\frac{d^2E}{dk^2}$$ (3.5)
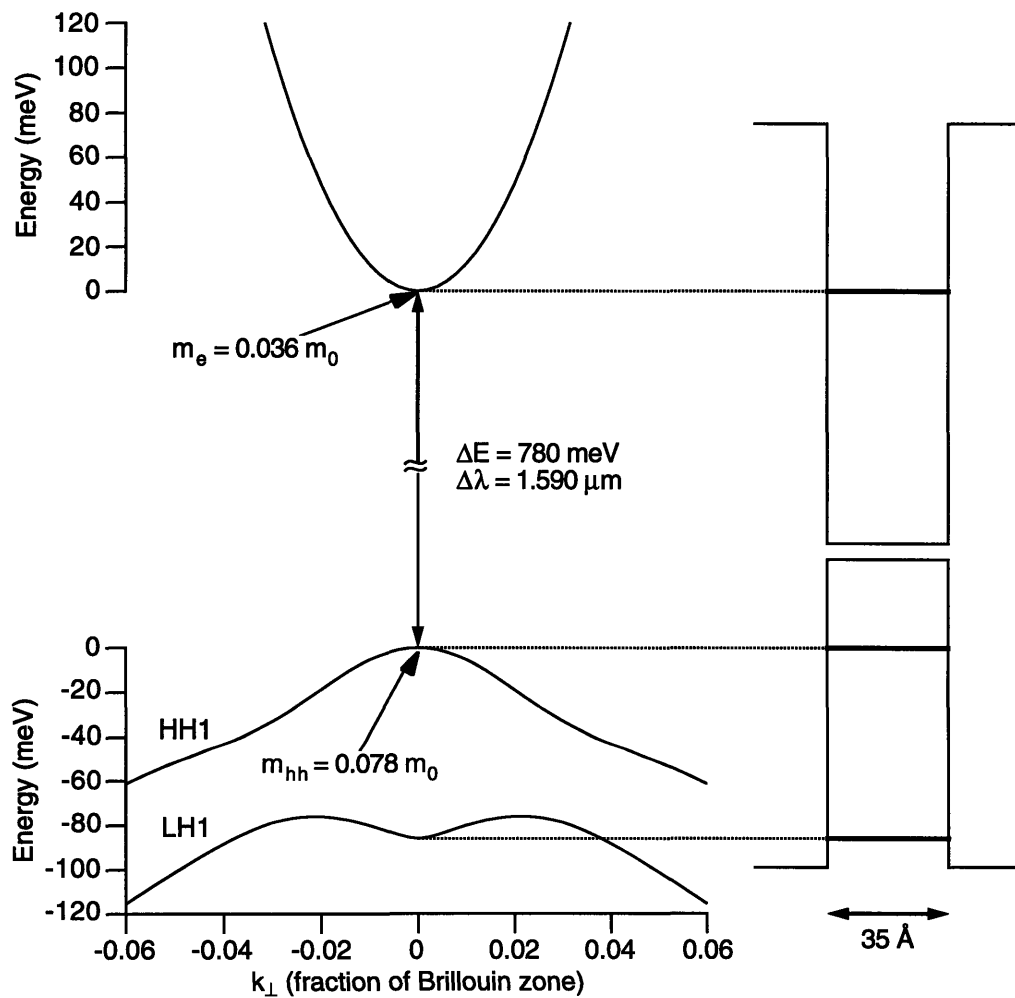
Figure 3.11: Calculated band structure for the compressive well. The transition energy and the bulk bandgap (627 meV) are not to scale.

where $\hbar$ is Planck's constant over 2π and d^2E/dk^2 is the band curvature. Since the band are not parabolic, the effective mass is a function of k. From the calculation it is found that the effective mass of the heavy hole in the compressive well (in the zone center) is $\sim 0.08\ m_0$ (where m_0 is the electron mass) and the effective mass of the light hole in the tensile well is $\sim 0.21\ m_0$. This means that the heavy hole state is actually light and light hole is actually heavy (known as mass reversal). In fact the light hole is almost 3 times heavier which will lead to different dynamics in the different wells, as will be discussed later.
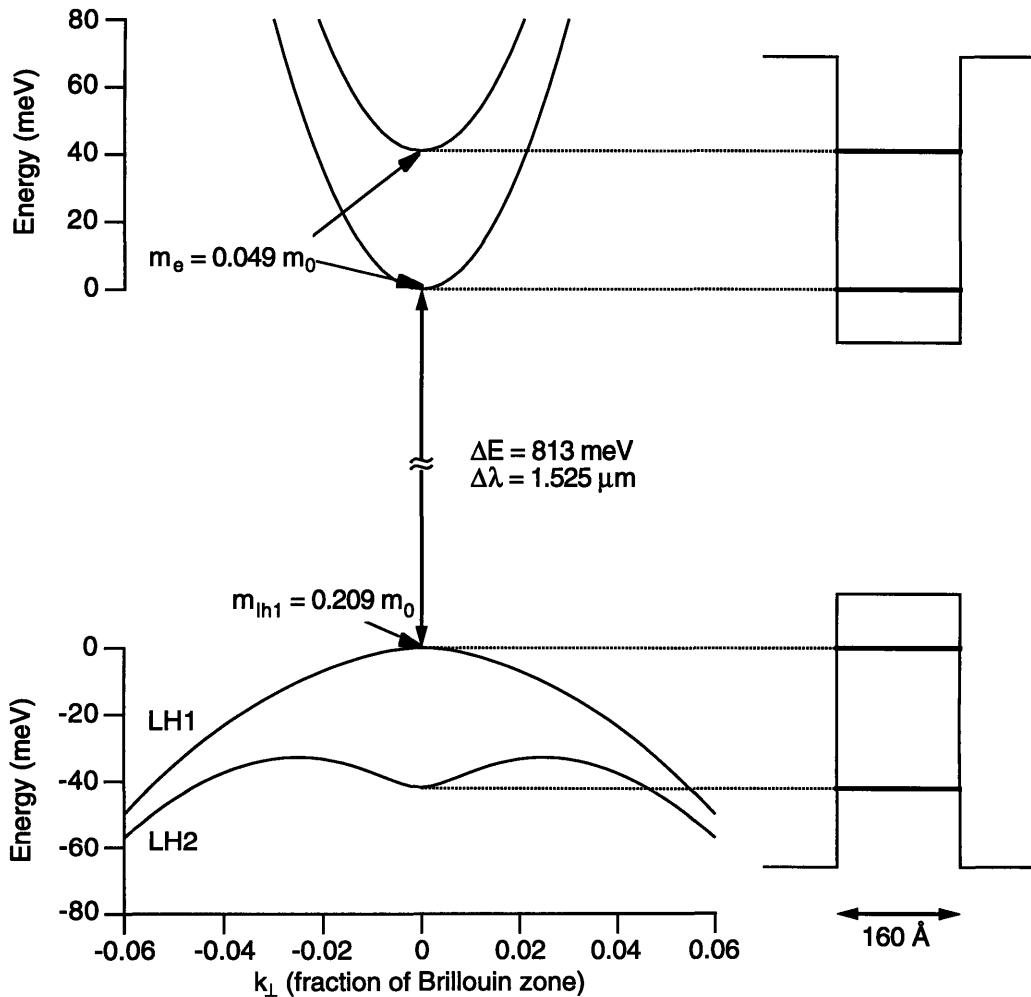
Figure 3.12:   Calculated band structure of tensile well. The transition energy and the bulk bandgap (781 meV) are not to scale

3.4.5 Electron tunneling time calculation

To better understand the interwell coupling, the electron tunneling time was calculated. Although, the experiment is not very sensitive to electron dynamics, the results of this

74

calculation should give some indication of the timescales involved in the problem. The model for the calculation consisted of one pair of wells extending infinitely in the $\pm z$ directions. The parameters for the calculation were taken from the k·p results. The eigenfunctions of the complete structure were calculated and are shown in Figure 3.13. The tunneling time was then calculated using:

$$\tau_{tunneling} = \frac{h}{2(E_2 - E_1)} \tag{3.6}$$

where the denominator is the energy difference between the fundamental symmetric and
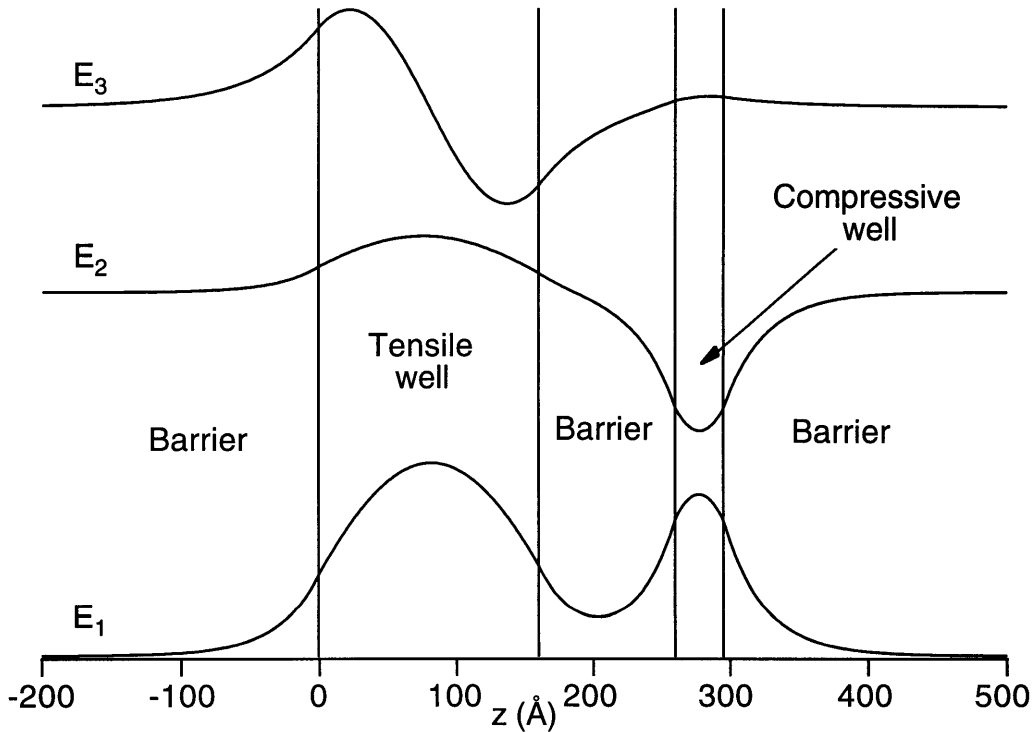
Figure 3.13:   The wavefunctions of the coupled compressive and tensile wells in the conduction band. E_2-E_1 = 1.7 meV and E_3-E_2 = 41.6 meV.

antisymmetric wavefunctions. The tunneling time was found to be ~ 1.2 ps, meaning that if a wavepacket is launched in one of the wells, the maximal transfer to the other well

75

occurs after 1.2 ps. Note that the transfer from one well to the other is never complete, because the wells are not identical.

The probability of hole tunneling is low, because of the larger masses that are involved, but more importantly because the states in the two wells are orthogonal in the Brillouin zone center, as explained earlier. Tunneling as an interwell transfer mechanism is therefore negligible.

3.4.6 Estimates for interwell transfer times

After tunneling has been discounted as a means for interwell transfer, the only remaining mechanism is diffusion across the barrier (which follows the optical excitation), followed by recapture of the carriers into the QW's. The diffusion process is well understood and the diffusion time scales as L^2/D where L is the barrier thickness and D is the diffusion constant. It has been found that the diffusion is ambipolar, so that the total diffusion constant is closer the hole diffusion constant. However, recent experimental investigations have shown that transfer times do not scale with the square of L, but follow an almost linear scaling law [70]. It was found that by considering a rate equation based on liquid flow dynamics, which weights the electron and hole quantum capture times by appropriate probability densities and includes carrier cooling, leads to good agreement with their experimental observations. Their results for high excitations in a passive unstrained InGaAs sample indicate total transfer times for 100 Å, of about 2-3 ps [70]. Adding strain in their experiments did not alter the results significantly.

The problem of quantum mechanical capture time in QW's is a difficult one and has been extensively covered in the literature in recent years. Such phenomena as capture time oscillation as a function of well width, have been reported [71]. However, in the limit of high carrier densities (our operation regime), these effects are smeared out because the carrier energies are broadened by carrier-carrier scattering. The well width does play a role in the capture process in the following way: when the well gets narrower the bound level rises in the well and approaches the barrier and the 3D density of states region. As the density of states changes from a 2D density of states to a smaller 3D density of states, the capture rate decreases and the capture time increases. Based on the conclusions of ref. 70 it seems hard to treat diffusion and the recapture process separately, and therefore a total transfer time is a more reasonable quantity. In our device, which is active (rather than passive) and has InGaAsP (rather than InP) barriers, that the total transfer time is on the order of a few picoseconds, similarly to the results of ref. 70.

3.5 Related results for these devices

3.5.1 Four wave mixing experiments

Recently, CW four wave mixing (FWM) experiments were performed on identical devices [72]. In these experiments the FWM sideband power is measured as a function of the frequency detuning between the CW pump and probe beams. Each time the inverse detuning is comparable to a time constant in the material response, there is a pole and corresponding rolloff in the FWM signal. The dispersion of the device causes phase mismatch and shows up as a sinc function modulating the response. Ideally, the sinc function should be broader than any inverse frequency of interest. The experiment is performed for both the Stokes and anti-Stokes sidebands, and the results are than fitted with a sum of complex Lorentzians. Unfortunately, there are a lot of fitting parameters and to get a good interpretation of the results, they have to be supplemented by independent measurements such as time-resolved pump-probe measurements.

The experiments described in ref. 72 were carried out with the four different TE and TM polarization combinations for the pump and probe beams. The maximum detuning was ~ 1 THz corresponding to 160 fs. The conclusions from this experiment were indicated that the main contribution to interwell transport was from carrier number transport (as opposed to carrier temperature transport), i.e., escape, diffusion and recapture of carriers. No indication was given as to the timescales involved in this process.

3.5.2 CW saturation theory

The CW nonlinear characteristics of these devices were recently investigated theoretically [73]. A rate equation model for the two bound levels in the QW's and one continuum level was used, and the self-saturation (e.g., TE saturation due to TE pumping) and cross-saturation (e.g., TE saturation due to TM pumping) of the devices was investigated. This model took into account the fact that TE transitions are allowed in both wells , but TM transitions were forbidden in the compressive well. This "asymmetry" leads to polarization dependent cross-saturation (i.e., the cross-saturation characteristics are different for TE-TM and TM-TE). The parameter of importance in these calculations is the ratio, R, of carrier escape rate from the wells to the carrier capture rate by the wells.

Finally, the induced anisotropy was investigated by simulating the effects of the device on a probe beam linearly polarized at 45° at the device input, while being pumped by another beam. Induced birefringence leads to an ellipticity of the probe polarization at the output, and induced dichroism leads to a rotation or tilting of the probe polarization at the

output of the device. The amount of anisotropy depends critically on the parameter R. Induced anisotropy suggests an optical switching element based on polarization control in a SOA which has been verified experimentally [74]. These theoretical results will have a bearing on some of the results discussed later.

3.6 Anisotropy in the nonlinear response of PI-SOA's

Although the linear response of the PI-SOA's is polarization insensitive or isotropic by design, this does not imply isotropy of the nonlinear response. In fact, as discussed earlier, theoretical results on the CW saturation characteristics of these device predict polarization-dependent or anisotropic behavior. The results of the present experiment show further dynamic anisotropy on a femtosecond time scale.

3.6.1 Polarization resolved pump-probe results

In the experiment, the pump and probe wavelengths are held constant (1.51 µm in this case). In order to explore the different regimes of operation (gain, transparency and absorption), the injection current is tuned. In this way the quasi-Fermi level is moved relative to the probing wavelength or energy. The measurement results consist of gain and index data taken in each one of these operation regimes. The injection currents corresponding to gain, transparency and absorption were 80, 33 and 28 mA, respectively. As explained earlier, switching from a gain measurement to an index measurement means switching the radio receiver from AM detection to FM detection. For each of these 6 sets of data all 4 combinations of TE and TM polarizations for the pump and probe, were measured.

The pulsewidth for these measurements was ~ 130 fs at a center wavelength of 1.51 µm. Care was taken to control the pump power such that the induced transmission changes were no more than ~ 10%. In this regime of operation the pump-probe signal scales linearly with pump power as it should. Too much pump power causes the trace to distort and indicates higher order nonlinearities. Typical pump powers were estimated to be a few hundred femtojoules at the input of the devices. The phase change associated with a 10% transmission change was found to be ~ $\pi/10$ and by increasing the pump to a point where the transmission change was ~ 90%, a phase change of 0.75π was observed (similar changes have been previously reported in standard SOA's [75]).

As is well known, the pump-probe signal is proportional to the intensity autocorrelation convolved with the nonlinear response function [76]. This ignores coherent coupling, which is important in semiconductors primarily when pump and probe are copolarized [77], and will be addressed later. The nonlinear response was modeled as a sum of a Dirac

delta function, a step function and two single-sided exponentials with different time constants:

$$a_0 \delta(t) + \left[a_1 \exp\left(-t/\tau_1\right) + a_2 \exp\left(-t/\tau_2\right) + a_3 \right] u(t)$$

$$u(t) = \begin{cases} 1 & t \geq 0 \\ 0 & t < 0 \end{cases} \tag{3.7}$$

The delta function accounts for processes, which are much faster than the pulse width (or more accurately, the width of the intensity autocorrelation function). The step function accounts for processes which are much slower than the total time measurement window, and therefore seem like a step change. The delta function and step function may be thought of as single-sided exponentials with very short and very long time constants, respectively. The remaining two exponentials account for processes with intermediate timescales, and in some sense are the processes of real interest in the experiment. The process with the longer time constant is usually attributed to carrier cooling times. After energy has been injected into the carrier bath by the pump pulse, the heated non-equilibrium carrier distribution interacts with the lattice (mainly by emitting LO phonons) and cools down with this time constant. The shorter time constant has been attributed to a delay in the carrier heating [78] and also includes the effect of an artifact due to index-gain coupling [79].

The total response is now convolved with the measured intensity autocorrelation. The amplitudes and time constants in the response function are adjusted until a best fit is achieved. The convolution computation time goes in general as the number of points squared. This can be made more efficient when the following is realized:

$$S(t) = g(t) * \exp(-t/\tau) u(t) = \int_{-\infty}^{\infty} g(t) \exp\left[-(t'-t)/\tau \right] u(t'-t) dt$$

$$= \exp(-t'/\tau) \int_{-\infty}^{t'} g(t) \exp(t/\tau) dt \tag{3.8}$$

which in discrete form looks as follows:

$$S(n) = \exp(-n(\Delta t)/\tau)(\Delta t) \sum_{i=-\infty}^{n} g(i(\Delta t)) \exp(i(\Delta t)/\tau) \qquad (3.9)$$

If a running sum is kept, the whole convolution can be computed by looping over the array of points only once (instead of twice). The convolution of the intensity autocorrelation function with the step function gives the partial area under the autocorrelation function and can be computed similarly with a running sum, and the convolution with the delta function is trivial (the autocorrelation function itself).

Figure 3.14 and Figure 3.15 show the pump-induced transmission and phase changes, when the device is operating in the gain regime (I = 80 mA). The long-lived step change in the transmission data confirms this to be the gain regime: the pump causes stimulated transitions, depleting the upper level (or conduction band) and reducing the long-lived gain (which eventually recovers on the recombination time scale). Also shown in the figures is are theoretical fits to the data. In this regime of operation it was possible to fit the data with a very small or zero fast component. The data also show that the cooling time of all polarization combinations except the TE-TE combination was ~ 700 fs, but that the TE-TE combination had a ~ 900 fs time constant, both in the transmission and index measurements. The fitting error on the time constants was smaller than 50 fs. This data suggests that there is an anisotropy in the device, since the response is pump-polarization dependent.

Figure 3.16 and Figure 3.17 show the pump-induced transmission and phase changes, when the device is operating near the transparency point (I ≈ 33 mA). The absence of long-lived steps in the data confirms that the measurement is near transparency, since beyond the first few picoseconds the net gain is zero and the transmission has recovered to the level of transmission before zero time delay (i.e., before the arrival of the pump pulse). These data show the same behavior for the cooling time constants as the gain regime set. However, here a spike near zero time delay becomes obvious; and, in the fit, the exponential with the short time constant is necessary to achieve a good fit. In fact, The short time constant is shorter than the intensity autocorrelation width. This feature is due to index-gain coupling and will be discussed later.

Finally, Figure 3.18 and Figure 3.19 show the pump-induced transmission and phase changes, when the device is operating in the absorption regime (I = 28 mA). Again, the fact that the long-lived changes in the transmission data step up, confirms this to be the
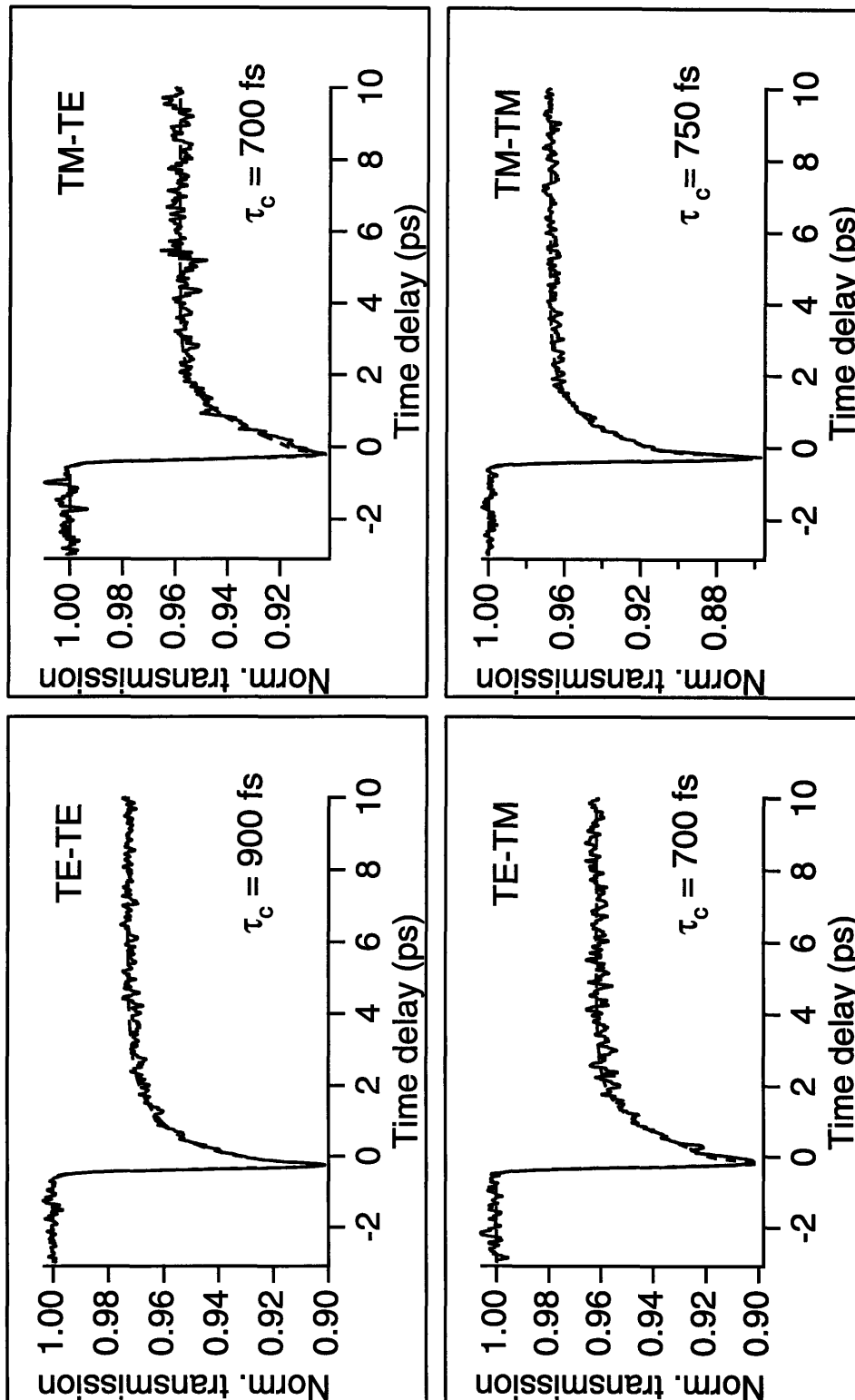
Figure 3.14: Pump-probe data for transmission changes in the gain regime (I = 80 mA). The solid lines are the data and the dashed lines are the fits.
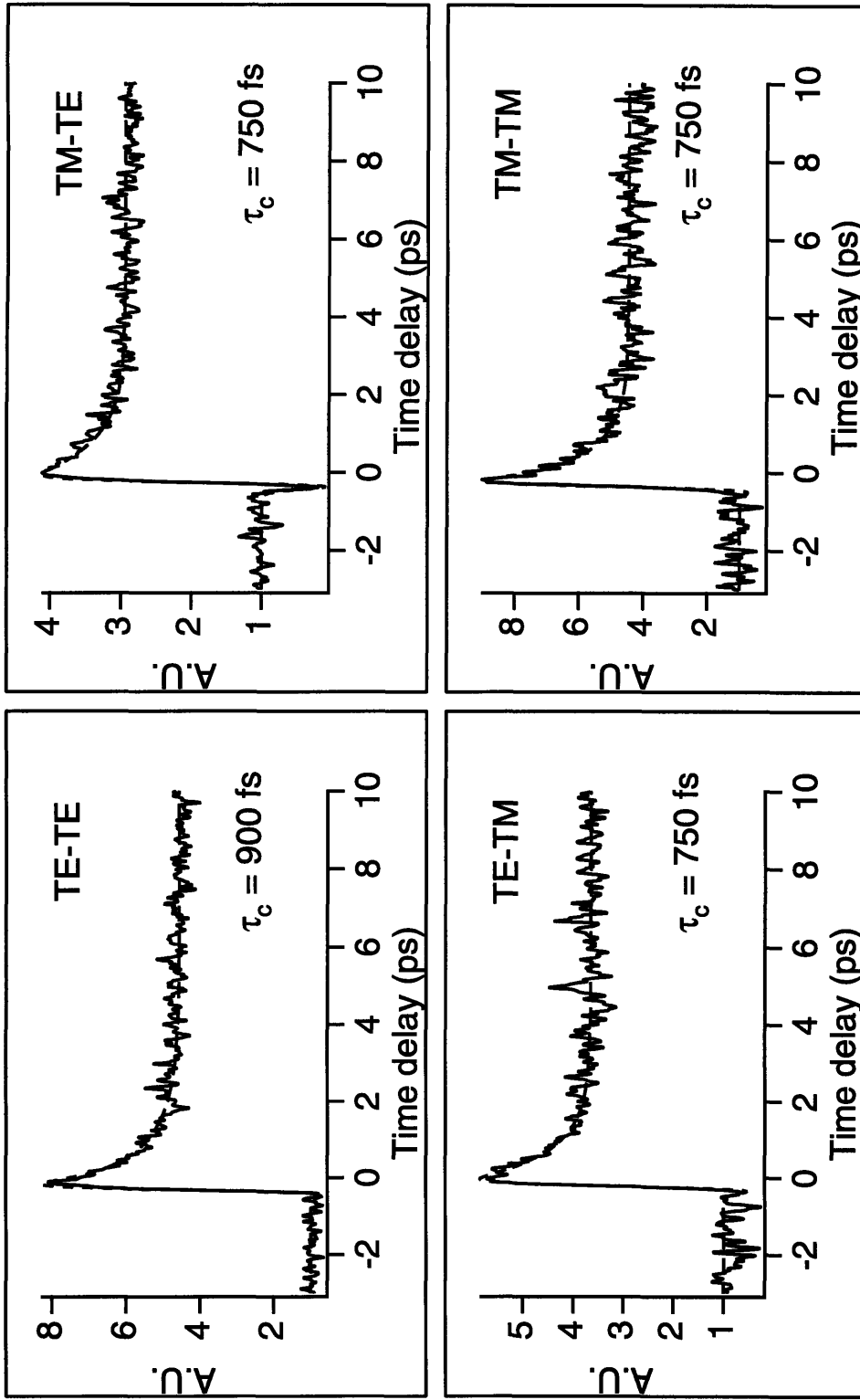
Figure 3.15: Pump-probe data for index changes in the gain regime (I = 80 mA). The solid lines are the data and the dashed lines are the fits.
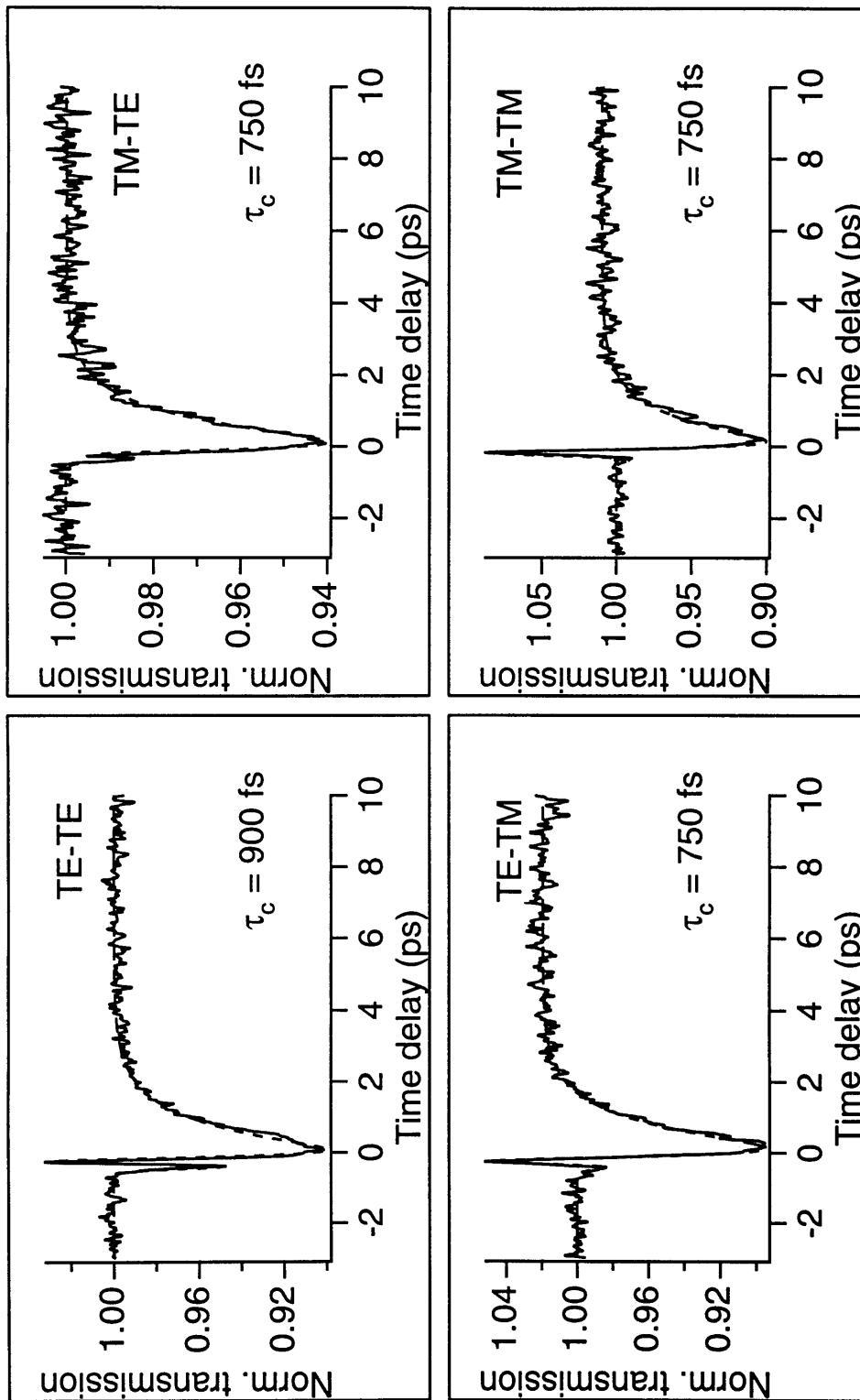
Figure 3.16:   Pump-probe data for transmission changes near the transparency point (I =
33 mA). The solid lines are the data and the dashed lines are the fits.
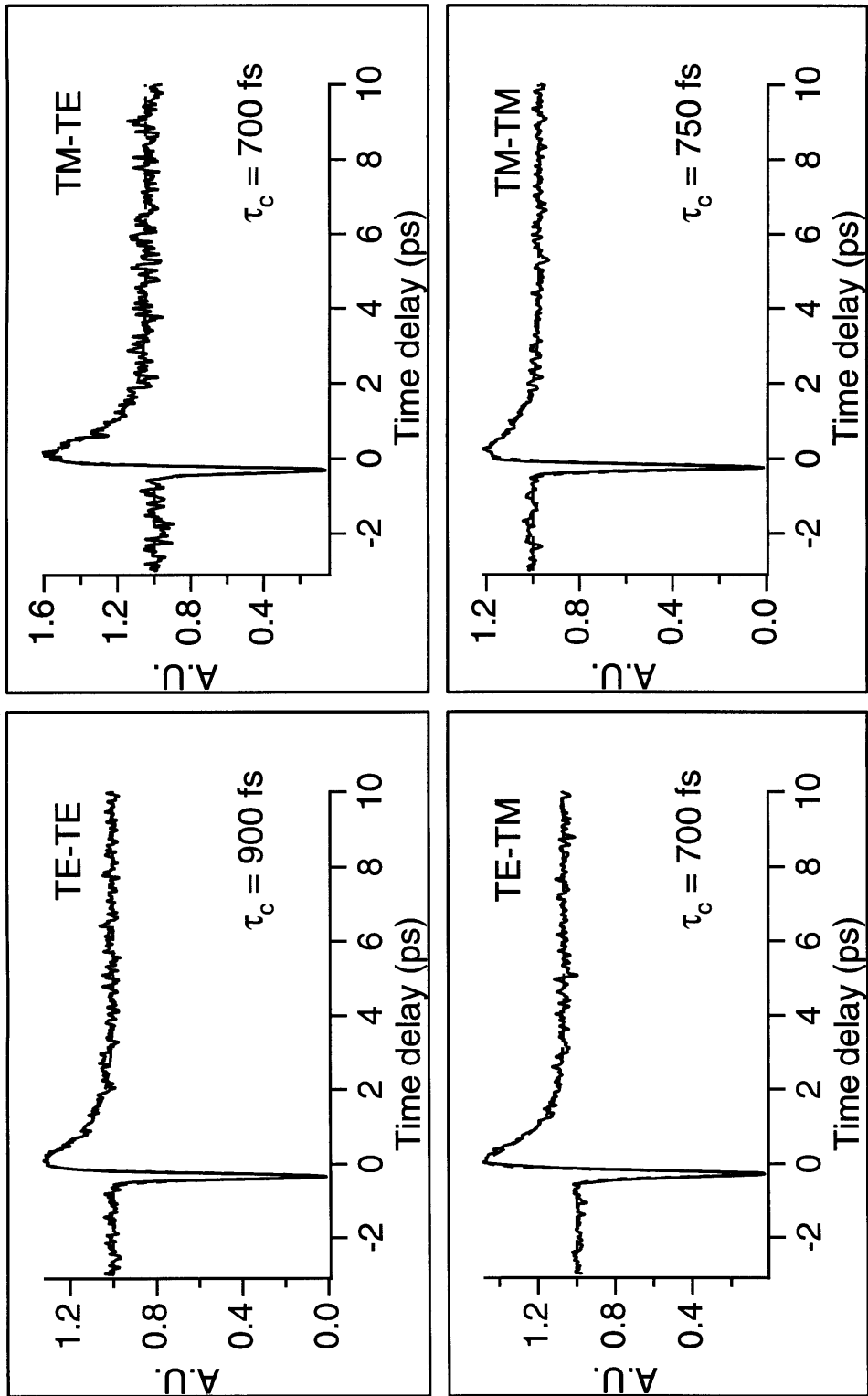
Figure 3.17:   Pump-probe data for index changes near the transparency   point (I = 33 mA). The solid lines are the data and the dashed lines are the fits.
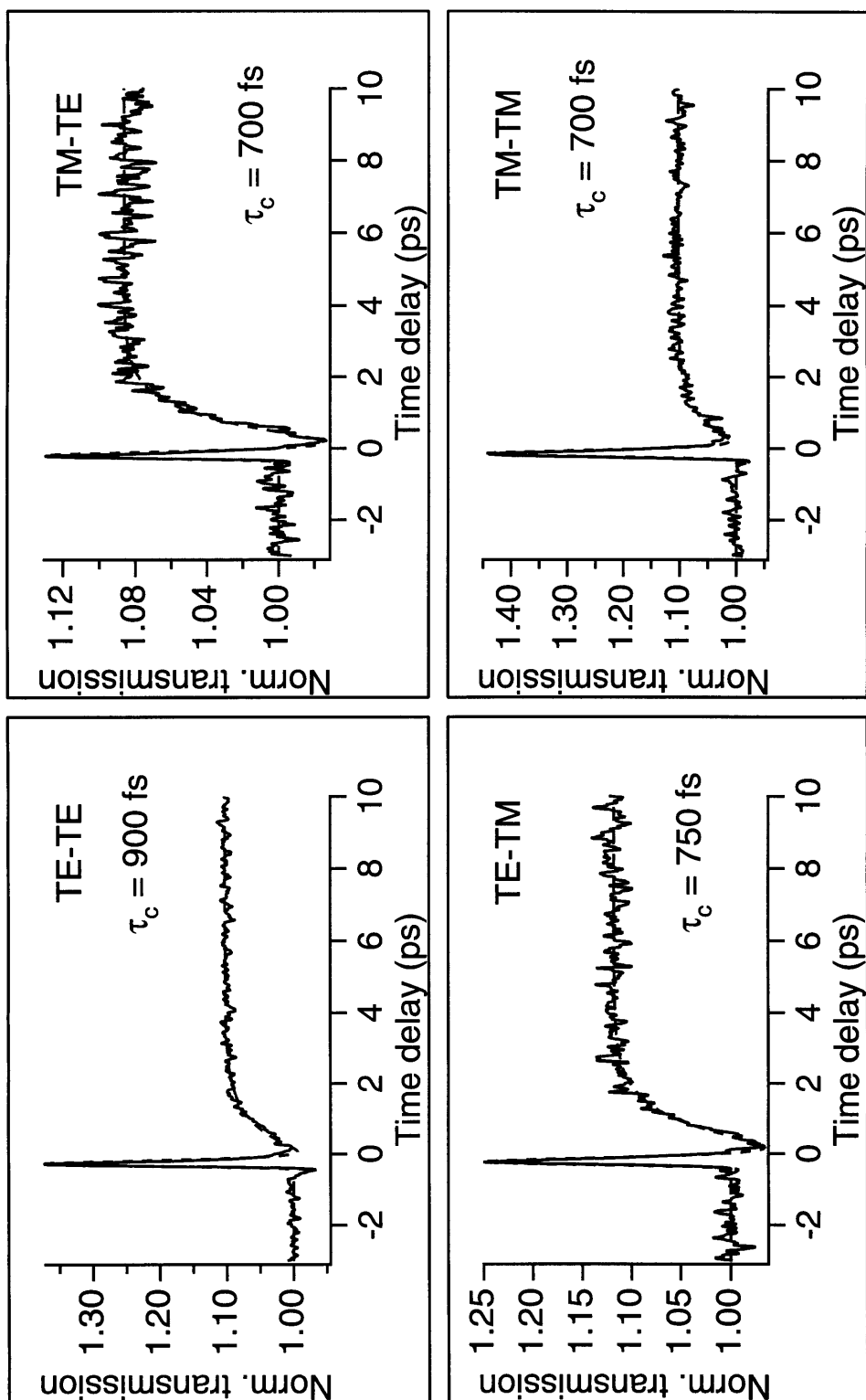
Figure 3.18: Pump-probe data for transmission changes in the absorption regime (I = 28
mA). The solid lines are the data and the dashed lines are the fits.
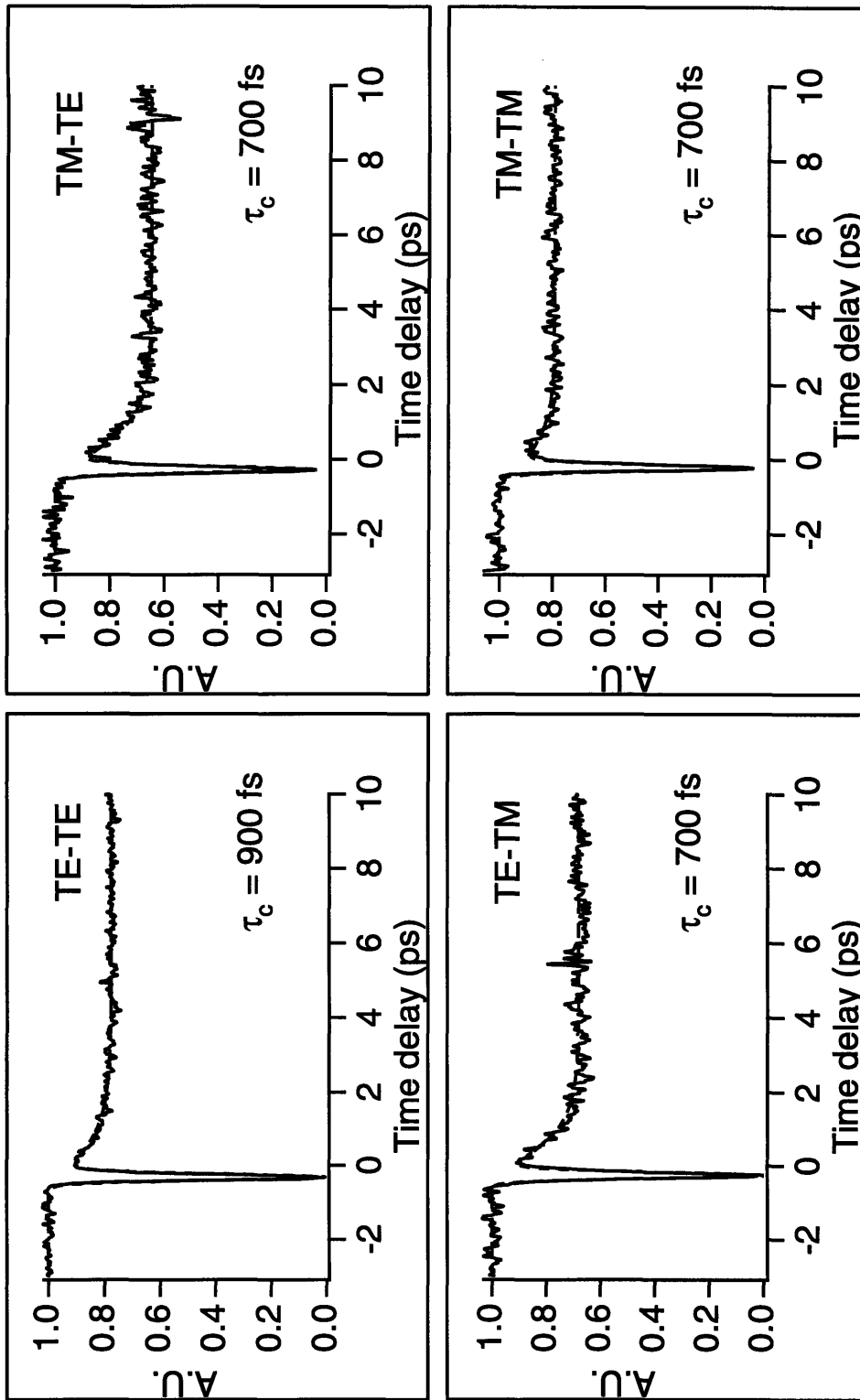
Figure 3.19: Pump-probe data for index changes in the absorption regime (I = 28 mA). The solid lines are the data and the dashed lines are the fits.

absorption regime: the pump gets absorbed and the probe sees an increase in gain for a time on the order of the radiative recombination time. Here also the cooling time exhibits the same behavior as the previous sets of data, and the spike near zero time delay becomes even more pronounced.

3.6.2 Interpretation of the results

A few features of the results are not specific to this device, and have been observed before in SOA's [75] [80]. The instantaneous part of the response in the transmission data is attributed mainly to two photon absorption (TPA) and any other process faster than the pulsewidth in the experiment. The instantaneous part of the response in the index data is attributed to the AC or optical Stark effect. This process involves virtual transitions that dynamically renormalize the bandgap, or "push" levels apart. Another contribution to the instantaneous index change is the index change associated with the TPA (through the Kramers-Kronig relation [81]). The net instantaneous part of the response in both transmission and index, shows a decrease of the signal. In contrast, the step function and exponential part of the response show opposite behavior in transmission and index response: a decrease in transmission leads to an increase in index.

Another important feature common to pump-probe experiments is the coherent coupling term [76] [77]. It arises from the coherent interaction between the pump and probe fields, when the pulses overlap in time. When pump and probe are copolarized the coherent coupling leads to a doubling of the total response at zero time delay (because both the coherent and the incoherent part of the signal arise from the same tensor element of the nonlinearity, $\chi^{(3)}_{xxxx}$). When the pulses are cross-polarized the coherent coupling adds only an instantaneous component at zero time delay to the response (because polarization memory in semiconductors is much shorter than our time resolution). In this case the coherent and incoherent parts of the signal arise from different tensor elements of the nonlinearity ($\chi^{(3)}_{xyyx} = \chi^{(3)}_{xyxy}$ and $\chi^{(3)}_{xxyy}$, respectively), and their relative magnitudes depend on the details of the material. Therefore, the apparent size of the response at zero time delay in the copolarized case is larger than in the cross-polarized case. It should also be noted that the part of the coherent coupling term due to the instantaneous part of the response follows the intensity autocorrelation, whereas the part due to the step part of the response follows the field autocorrelation squared. Finally, it should be noted that the group velocity of TE and TM polarized pulses traveling in a waveguide, is different [82]. This means that when the pump and probe are cross-polarized, they walk off each other (in time) as they travel through the waveguide. Effectively this is equivalent to pulse broadening and loss of time

87

resolution. However, in similar SOA's the walkoff was measured to be ~ 100 fs and led to an effective pulse broadening of less than 10 % [43].

The main and unique feature observed in this device is the longer cooling time, apparent only in the TE-TE configuration. As explained earlier, probing with TE-polarized light means probing mainly the compressive well. However, when probing with TE-polarized light, the cooling time constant depends further on the pump polarization, revealing a dynamic anisotropy in the device. When probing with TM-polarized light (i.e., mainly the tensile well), no such anisotropy is observed.

The longer 900 fs cooling time has been observed in a device consisting only of 4 compressive strained wells with very similar parameters to the device in the present experiment [78]. Keeping in mind that the experiment is mainly sensitive to hole dynamics and that the holes involved have very different effective masses in the two types of wells, the observed longer cooling time can be explained. The carrier cooling time is mostly mediated by the emission of LO phonons, and the carrier-LO phonon scattering time depends inversely on the effective mass of the carrier [83]. Therefore a longer cooling time in the compressive well, where the holes are lighter, is to be expected. This effect has recently been demonstrated theoretically [84]. Carriers can also be cooled by stimulated emission by removing hot carriers from the distribution. However, if this were the case here, the cooling time would change near the transparency point, where the net stimulated emission is zero. The data indicates that this is not the case since the cooling time does not change in the different operating regimes, and the contribution to the cooling through stimulated emission, is negligible.

The instantaneous part of the index response is seen to grow relative to the other parts of the response as the operating regime is changed from gain through transparency to absorption. This has been previously observed and explained [85]. This large instantaneous phase change leads to dynamic frequency shifts ($\omega(t) = d\phi(t)/dt$). The frequency of the probe therefore shifts on the transmission curve, and shows up as a derivative artifact near zero time delay in the transmission measurements. Obviously, the larger the index change the larger the transmission artifact. This sort of index-gain coupled artifact was recently investigated theoretically [79].

The final point of interest is the mechanism behind the anisotropy: what would make the excitation pump dependent? To the extent that the heating is due to free carrier absorption, it is clear that the heating will be different in the different wells. This is because the free carrier absorption cross-section is dependent on the effective mass [83]. However,

both wells will be excited for both polarizations and to explain the anisotropy would mean assuming the free hole absorption is anisotropic. On the other hand it is well known [86] that in the InP-based materials free hole absorption is dominated by intervalence band absorption (IVBA). This process can occur away from the center of the Brillouin zone and involves resonant transitions from the heavy and light hole bands to the split-off band.

As was explained earlier, such a transition is only possible when the momentum matrix element is of the form $\langle S|p_i|I\rangle$ where $i = x,\ y,\ z$ (see section 3.3.5). This means that the coupling of the conduction band to the valence bands can no longer be ignored. Terms linear in k, whether from the k•p theory [49] [87] or strain-induced [65], contribute to this coupling. Now it is reasonable to assume that these transitions, which in some sense resemble conduction to valence band transitions, will be polarization dependent for the same reasons. Specifically, heavy hole, light hole and split-off band states will consist of different linear combinations of the $|S\rangle$, $|X\rangle$, $|Y\rangle$, $|Z\rangle$. If, for example, the heavy hole band has a negligible $|Z\rangle$ function component, then TM induced excitation to the split-off band will be correspondingly negligible. This would explain the observed polarization dependent excitation, since the two different wells contain two different initial states for these transitions. This assumes that there is no interwell equilibration, while the carriers are in a high-energy, non-equilibrium state, from which they could easily scatter between wells (in this high-energy state they would be extended states and not subject to slower diffusive transport). To confirm the polarization dependence of IVBA, at least theoretically, would require a full 8×8 k•p calculation including all three valence bands and the conduction band, which was not undertaken here.

3.7 Direct measurement of the anisotropy

The anisotropy is basically the difference between 2 traces (e.g., between the results of the TE-TE data and the TM-TE data). However it is not clear how to weight the different traces correctly, and also small differences may be lost when subtracting 2 large quantities. It is therefore desirable to have a direct measurement of the anisotropy, which would also confirm its existence unambiguously. Such a technique was demonstrated for the measurement of anisotropic absorption saturation [88]. A conceptually similar technique based on the existing heterodyne pump-probe setup was used to measure the induced dichroism and induced birefringence in the present device.

89

3.7.1 Basic concept

Figure 3.20 introduces the basic idea behind the measurement. The probe beam is set at a linear 45° polarization state and the reference beam is set to the orthogonal polarization. A polarization controller after the device compensates for any linear birefringence or resid-
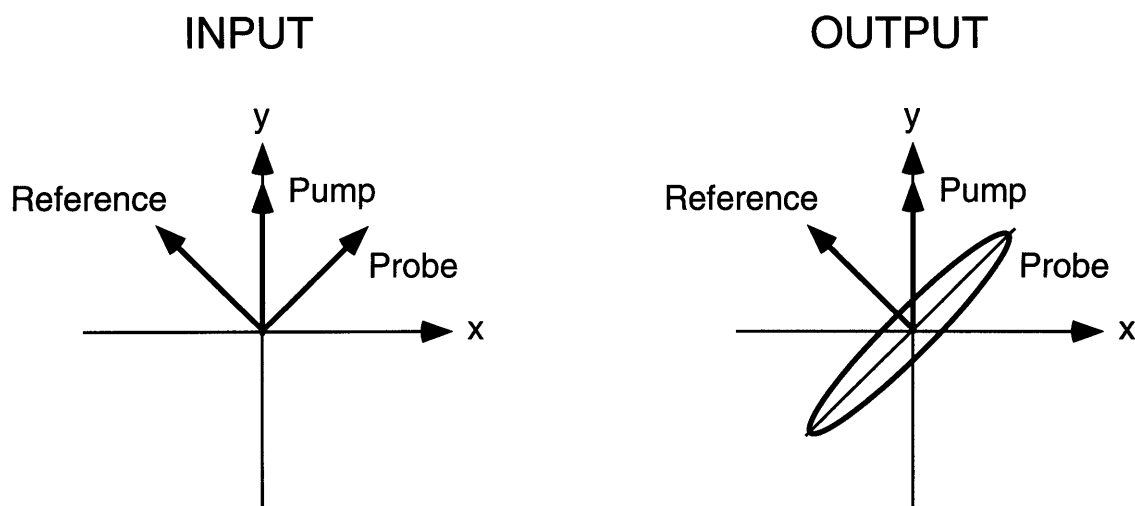
Figure 3.20: Basic idea of direct anisotropy measurement. In the absence of the pump, the probe and reference do not beat. The pump induces anisotropy, changing the probe polarization to have a component along the reference.

ual dichroism (which should be absent by design). This polarization controller (indicated as a dashed box in Figure 3.3) consists of a $\lambda/4$ waveplate followed by a $\lambda/2$ waveplate, which together can take an arbitrary elliptical polarization state and transform it to any specific linear polarization state, in this case 45° linear. When the pump is absent, probe and reference are orthogonal and do not beat, resulting in an absence of a heterodyne signal. When the pump is unblocked, it induces birefringence (which will turn the probe elliptical) and dichroism (which will tilt the state of polarization of the probe). This in turn gives the probe some component along the reference, which will result in a beat signal. This signal is a direct measure of the induced anisotropy.

3.7.2 Analytical expression for the measured signal

To make this more quantitative, we present a derivation for the measured signal (by the radio receiver). It is assumed that the probe is in some linear state of polarization, before and after the device (i.e., linear anisotropy is compensated). This will be a more general case since the probe can be in any linear state (not necessarily 45°). Since the detection

90

system is only sensitive to the beat signal of the probe and reference, it is only this term that will be examined. This beat signal arises from the sum of the two fields being squared by the detector, so that the beat signal may be written:

$$S \propto \mathrm{Re}\left\{\vec{E}_{ref} \bullet \vec{E}_{pr}^{*} \exp(i\omega_{b}t)\right\}$$

(3.10)

where ω_{b} is the beat frequency (1 MHz in the present experiment). The probe and reference fields may be written in Jones vector notation:

$$\vec{E}_{pr} = \frac{1}{\sqrt{a^{2}+b^{2}}}\binom{a}{b}$$

$$\vec{E}_{ref} = \frac{1}{\sqrt{a^{2}+b^{2}}}\binom{-b}{a}$$

(3.11)

where a and b are real numbers. If the pump induces anisotropy, the x and y components of the probe polarization will pick up different changes in amplitude and in phase. The probe can now be written as:

$$\vec{E}_{pr} = \frac{1}{\sqrt{a^{2}+b^{2}}}\binom{(a+\delta_{x})\exp(i\phi_{x})}{(b+\delta_{y})\exp(i\phi_{y})}$$

(3.12)

where the δ_{i} and ϕ_{i} are the amplitude and phase changes in the ith component of the polarization of the probe. The signal S can now be written as follows:

$$S \propto \mathrm{Re}\left\{\left[-b(a+\delta_{x})\exp(i\phi_{x}) + a(b+\delta_{y})\exp(i\phi_{y})\right]\exp(i\omega_{b}t)\right\} =$$
$$\left[-b(a+\delta_{x})\cos\phi_{x} + a(b+\delta_{y})\cos\phi_{y}\right]\cos(\omega_{b}t) -$$
$$\left[-b(a+\delta_{x})\sin\phi_{x} + a(b+\delta_{y})\sin\phi_{y}\right]\sin(\omega_{b}t)$$

(3.13)

When the radio is set to AM reception the radio takes the magnitude of the above signal, which means squaring each of the bracketed expressions above, adding the result, and then taking the square root. After some simplifications and using the trigonometric identities:

91

$$\cos^2 x + \sin^2 x = 1$$
$$\cos x \cos y + \sin x \sin y = \cos(x - y) \qquad (3.14)$$

we get:

$$S' \propto \sqrt{b^2(a+\delta_x)^2 + a^2(b+\delta_y)^2 - 2ab(a+\delta_x)(b+\delta_y)\cos(\phi_x - \phi_y)} \qquad (3.15)$$

Writing the induced birefringence ϕ_x-ϕ_y as $\Delta\phi$ and assuming it is small, so that the cosine term can be written as the two leading terms of a Taylor series expansion:

$$\cos(\Delta\phi) \cong 1 - \frac{(\Delta\phi)^2}{2} \qquad (3.16)$$

and making some further simplifications yields:

$$S' \propto \sqrt{(b\delta_x - a\delta_y)^2 + a^2 b^2 (\Delta\phi)^2} = ab\sqrt{(\delta_x/a - \delta_y/b)^2 + (\Delta\phi)^2} \qquad (3.17)$$

For the case of 45° linear polarization $a=b=1$, with the induced dichroism δ_x-δ_y written as $\Delta\delta$, the last expression simplifies to:

$$S' \propto \sqrt{(\Delta\delta)^2 + (\Delta\phi)^2} \qquad (3.18)$$

An interesting feature of the general expression is the fact that there is a unique linear polarization, satisfying the relation:

$$\frac{a}{b} = \frac{\delta_x}{\delta_y} \qquad (3.19)$$

where the measured signal is proportional to only the induced birefringence (how this polarization is determined experimentally, is described below). In any other case the signal contains a mix of the induced dichroism and the induced birefringence, with no way to

separate the contributions. It should be remembered that we are dealing with a dynamic anisotropy that changes in time and the above relation will only yield the induced birefringence at one particular instant. In the present experiment, the signal, as expected, measures the amount of total induced anisotropy containing contributions from both the induced dichroism and the induced birefringence.

The above derivation assumed AM reception on the radio. One might wonder what would be detected in the FM case. FM detection will give the phase of S and therefore the tangent of the phase angle is given by the ratio of the bracketed expressions in (3.13). Simplifying the expression and Taylor expanding to first order yields for the phase angle:

$$\Phi = \tan^{-1}\left(\frac{\delta_x/a - \delta_y/b}{\phi_x - \phi_y}\right) \qquad (3.20)$$

and again for the case of 45° linear polarization this reduces to:

$$\Phi = \tan^{-1}\left(\frac{\Delta\delta}{\Delta\phi}\right) \qquad (3.21)$$

The argument of the arctangent is reminiscent of the definition of the α parameter for semiconductor lasers, and so may be thought of as an anisotropy α parameter. The general expression (3.20) also gives an experimental way for determining the "magic" polarization orientation that nulls the induced dichroism part. This can be achieved by changing the probe's polarization until the FM signal vanishes. Again, this would be only at one fixed time delay between the pump and probe.

3.7.3 Measurement results

Figure 3.21 shows the results of this direct anisotropy measurement. The probe was oriented at 45° linear and the reference was made orthogonal to it by blocking the pump and minimizing the beat signal. The two traces shown are for TE polarized pump and TM polarized pump. Where, for example, in the case of TE polarized pump, the differences in transmission and index of the TE-TM and TE-TE configurations, are measured. The fact that the measurement shows a non-zero result, confirms the existence of pump-induced anisotropy. The data also show a longer time constant which was not apparent in the normal pump-probe measurements. Since Figure 3.21 does not show if the transmission levels

out, it is not clear if the response contains a step function or the anisotropy decays on a much shorter time scale than radiative recombination. Figure 3.22 shows the data similar
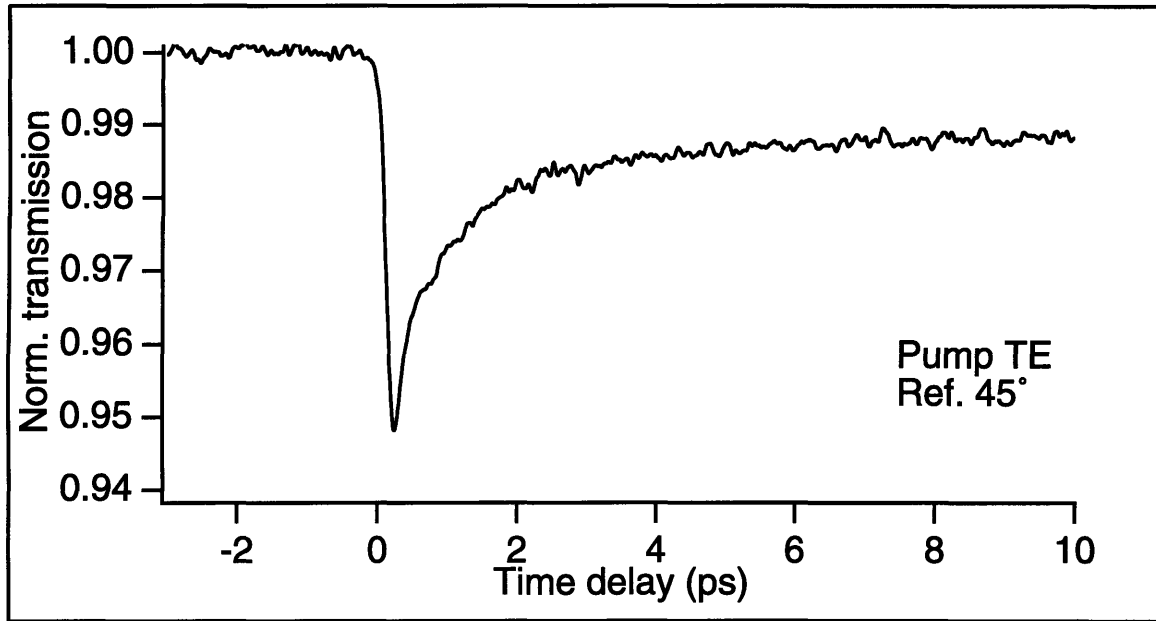
(a)
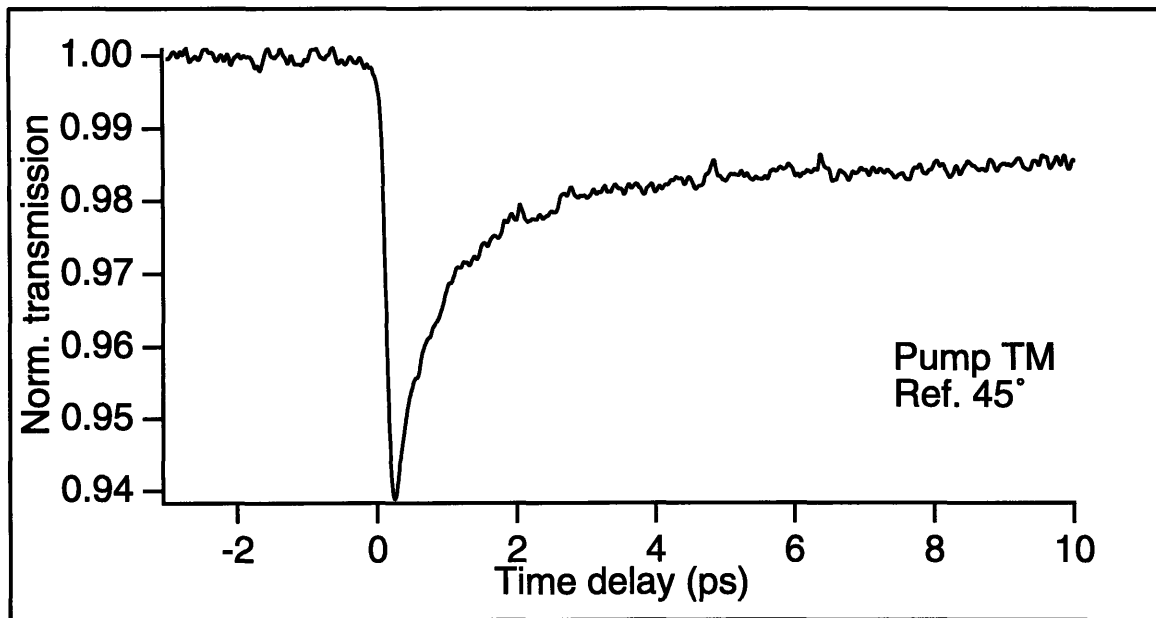
(b)

Figure 3.21: Results of direct anisotropy measurement. Probe is polarized at -45° linear, reference is polarized at +45° linear and pump is TE (a) or TM (b).

to Figure 3.21, but the scan extends to longer time delays between pump and probe. In this case the data shows that there is a step function component and the long time constant is fit with ~ 7 ps.

At this point it should be remembered that the initial motivation for this experiment was to extract interwell coupling dynamics. The expectation was to see such coupling in the normal pump-probe experiment, when the pump and the probe are cross-polarized: the pump exciting mainly one type of well and the probe probing mainly the other type. The signature of such a process would be something like a delayed step response. After excita-
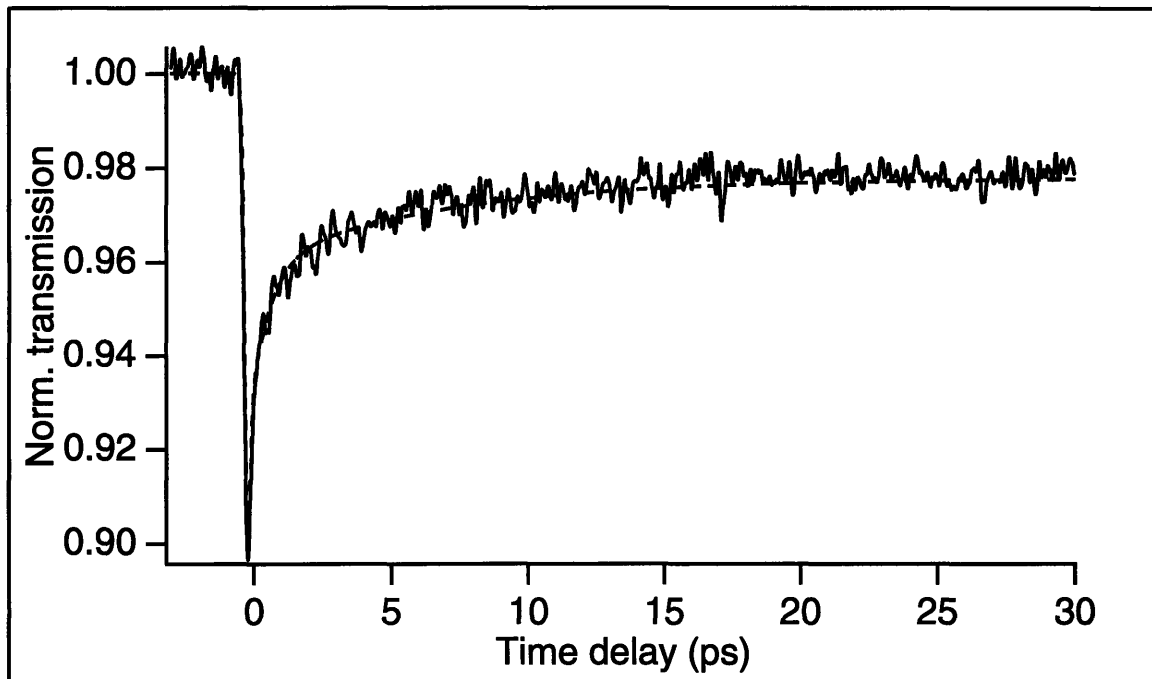
Figure 3.22: Direct anisotropy measurement with the pump TE polarized. The scan extends to 30 ps time delay between pump and probe to show the response flattening out. The solid line is the data and the dashed line is the fit.

tion interwell transfer would occur with some time constant and the recaptured carriers would stay in the new well until radiative recombination occurred. This behavior was not observed in the normal pump-probe measurement, but the direct anisotropy measurement is a much more sensitive differential measurement. It subtracts from the cross-polarized data the response due to "self-coupling" and so can bring out only the pure cross-coupling response.

In the above measurement, when the pump is TE polarized a new time constant may be observed, because of the difference between the two exponential responses. However, when the pump is TM polarized, the exponentials (of TM-TE and TM-TM) have the same time constant and therefore such a new time constant would not be expected. The fact that the data shows a long time constant even in the TM case in Figure 3.21, indicates that this new long time constant must, at least in part, be due to another mechanism. The difference of two exponentials may be written as a delayed exponential decay characterized by an effective risetime. This effective time constant which arises from the different time constants in the TE case is $\tau_{eff} = \left(1/\tau_1 - 1/\tau_2\right)^{-1} \approx 3$ ps where $\tau_1 = 700$ fs and $\tau_2 = 900$ fs, in contrast to the 7 ps time constant observed in the measurements. Also, as explained above, the 3 ps effective time constant is expected in the risetime and not the decaying part where the 7 ps time constant is observed. This is strong support for the possibility of inter-well transport.

A recent study [70] has shown that in QW's based on this material system, the interwell transfer time for barriers of 100 Å width (the barrier width in the present device) is 2-3 ps. Furthermore, it was shown that the interwell transfer time could not be easily separated into diffusion and capture processes. If that were the case, the transfer time would be much shorter. The diffusion time constant of a carrier across a barrier L_b is given by $\tau_{diff} = L_b^2/D$, where D is the ambipolar diffusion constant, which for InP is 7 cm^2/s. For a 100 Å barrier this would give a diffusion time constant of ~ 140 fs. It was also shown in ref. [70] that their measurements showed a linear scaling with barrier width rather than a quadratic dependence. They concluded that a model similar to that for the dynamics of a classical fluid containing diffusion, a weighted capture process and distribution cooling, explained their data well. It should be noted that the above study dealt with InGaAs/InP rather than InGaAs/InGaAsP as in the present device. In the present device the strain is high and the typical carrier densities are high, both of which may modify the capture dynamics and explain the observation of a longer transfer time in the present experiment.

The final point to be addressed is the presence of a step function component in the anisotropy data which indicates a residual long-lived anisotropy. A recent theoretical investigation mentioned earlier [73] supports this experimental observation. In that study the CW saturation is investigated, this is exactly the step function part of the pump-probe response: the long-term gain reduction that the probe experiences, due to a strong CW pump. They simulated a similar experiment, where the probe polarization at the output of the device was calculated for an input probe polarization of 45° linear, in the presence of a strong CW pump. The change in the polarization would indicate the magnitude of the induced anisot-

ropy. They found that the parameter governing the size of that change depended critically on the ratio, R, of the carrier escape rate to the carrier capture rate. For $R = 1$ there was almost no change in the probe polarization, but for small R significant changes are predicted indicating a large induced anisotropy.

To confirm the long time constant as one due to interwell transfer would require a similar device, identical in all ways except having thicker barriers. In ref. 70 it is shown that the interwell transfer time increases by a factor of 2 when going from a 100 Å barrier to a 300 Å barrier, which is planned for a future experiment.

Chapter 4

Conclusions and future work

4.1 The fiber laser-seeded color center amplifier

The MOPA-pumped SP-APM was found to be an excellent source for high-energy femtosecond pulses at 1.5 μm. The pulse energy was up to 3 times higher than with previous Ti:Sapphire pumping, and the amplitude jitter was remarkably low. This source has recently been used as a source for a WDM system, where the wide spectrum is sliced into many WDM channels of picosecond pulses [89]. Another application where the ultrashort character of the pulses is not important, involved having a tunable filter outside the cavity with a bandwidth of 6 nm tunable over almost 60 nm, with pulse widths of 0.5-1 ps [90]. Since there is plenty of power, the energy loss due to the filtering was tolerable. Finally, this source can provide bright enough SHG in the red spectral region to make it a viable alternative for seeding a Ti:Sapphire regenerative amplifier (rather than using an Argon-pumped Ti:Sapphire).

The amplifier system proved to have some great advantages over previous amplifier systems at 1.5 μm, but suffered from some disadvantages. The two main points in favor of using this system are: 1) The stability of the source and 2) the high small-signal single-pass gain of the amplifier. It is easy to get to the microjoule level within 2 passes, making the collinear arrangement possible, and the generated continuum is very stable. On the down side, the gain spectrum of the amplifier is not well-matched to the center wavelength of the fiber laser, leading to gain narrowing and to 200-250 fs long pulses (although some improvement is achieved by tweaking the dispersion in the spectral slicer).

A stable continuum may be generated in a variety of materials, but for really large continuum ZnSe was the best from all the investigated materials. Although fiber gave an even larger spectral extent, it was not a femtosecond continuum since the temporal profile across the spectrum was all scrambled. Finally, the zero-dispersion compressor made a very good spectral slicer and to some extent compensated some further dispersion.

Future work with the fiber laser should include using it as an alternative source for pump-probe experiments. There is certainly enough power and short enough pulses. In addition, the noise characteristics of this laser show that even a few kHz away from the harmonics of the repetition rate (i.e., by chopping at a few kHz), signals on the order of 10^{-4} may be measured with no averaging. This performance is significantly better than the color center laser. Another point worth investigating is whether compensation of the next order of dispersion (i.e., third order dispersion) would yield pulses closer to the transform-limit (which for sech pulses of 60 nm bandwidth is 43 fs). This would involve setting up an additional grating compressor, which together with the prisms would be able to compensate for the second and third order dispersion. However, it was shown recently, by exact ray tracing methods that second and third order dispersion may be balanced with one set of prisms, by choosing the right material [91].

In the amplifier system, future work should include trying to optimize the gain medium, possibly by trying a color center with high gain and gain spectrum matching the center wavelength of the fiber laser more closely. Such a color center crystal may be KBr, which is very similar to the KCl, but has its gain peak at a longer wavelength. Of course there is always the possibility of seeding the amplifier with an APM KCl laser, automatically matching it to the amplifier. However, the need for active stabilization and the large amplitude jitter are compelling reason to avoid this solution. If Kerr-lens modelocking were successful with color center lasers (and it should be since the nonlinear index is at least as large as the one for Ti:Sapphire), this may become a worthwhile solution.

The number of passes in the amplifier could easily be scaled up to 4 passes as follows: After the second pass the beam (now TM polarized) is reflected off a corner cube and is sent back through the system parallel to the original beam. Just before the fourth pass the polarization has been flipped back to TE and is going back in the direction of the laser (passing through the polarizing beamsplitter). However, this beam is spatially separated from the original beam, and may be picked off. It is not clear that a substantial improvement is to be expected. First, the gain narrowing may offset any gain in energy and second, the beam quality may degrade such that not all of it is usable. In addition, since after 2 passes the amplifier is already saturated, it may be necessary to blow up the beam for energy extraction. Any gain in average power is important, because the beam is brighter (although the pulses are at a microjoule level, the repetition rate is 1 kHz). To that end, improving on the losses in the prism compressor could give up to 30 % more energy. An increase of average power can be had by going to a 3 kHz repetition rate at the expense of

cutting down the pulse energy by a factor of 3, so if the output of the amplifier can be increased to about 20 μJ (by using a third pass), a good continuum could still be produced.

The continuum itself may still be optimized by investigating a few more materials. Namely, ZnS, which should have a much lower multiphoton absorption cross-section (but still a an n_2 on the order of 10^{-14} cm^2/W). SF57 glass is a widely available glass with a nonlinear of index second only to SF58 and SF59 (which are very difficult glasses to handle, are environmentally unstable and stain easily). Finally, a short enough fiber (on the order of 1 cm) may give broad, controllable continuum. By judiciously choosing the fiber length, the continuum generation in conjunction with the spectral slicer constitute an optimal fiber-grating compressor. In this way some very short pulses (possibly < 50 fs) may be generated. For this to work, dispersion in the continuum generating material is essential, since it contributes to linearizing the chirp over the generated spectrum.

The end goal of this project is to have a source for continuum pump-probe experiments. The standard configuration for such an experiment is shown in Figure 4.1. It consists of two spectral slicers (one for the pump and one for the probe), with a variable time delay in
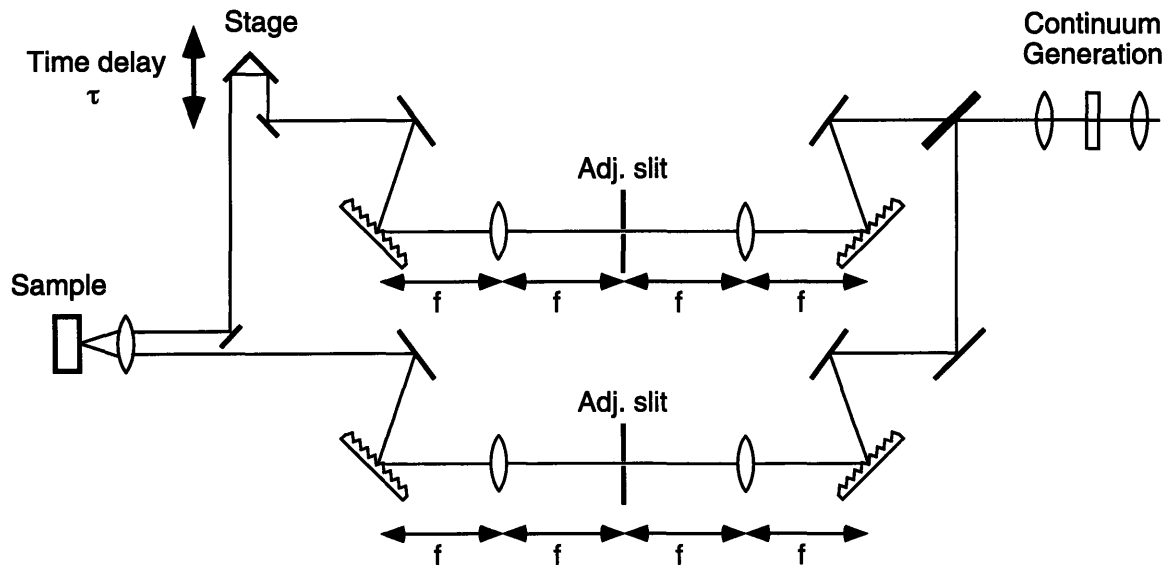
Figure 4.1: A continuum pump-probe setup with tunable pump and tunable probe, as well as bandwidth control for both.

one of the arms. In this way the most versatile system is realized, with tunable pump and tunable probe, and also variable bandwidth for pump and probe. This is ideal for two color pump-probe experiments. An alternative to this scheme would involve only one spectral

100

slicer for the probe, and the pump would be split off before the continuum generation. This would limit the pump pulse to 250 fs pulses centered at 1.52 μm. The main challenge in setting up this experiment, is the low average power available after spectral slicing. Since after continuum generation the total average power is 1-3 mW, after slicing it may well be under 100 μW, which would make lining up this experiment a non-trivial matter. However, good CCD IR viewers are available for the 1.5 μm spectral region, which will greatly reduce the difficulty of setting up this system.

A further improvement to the system would be changing it to a regenerative amplifier configuration, either a low repetition rate (~ 1 kHz) or a high repetition rate (~ 50 kHz) system. In this configuration, the amplifier crystal is inside a cavity. The seeding pulse is then switched in to go through the gain medium a controllable number of passes, after which it is switched out. This would involve replacing the pulse selection system with a switch-in switch-out system. The main advantage is the controllable number of passes such that a thin crystal may be used. A thin crystal, like a laser crystal, is much easier to make and to process. In the low repetition rate version, everything else would stay the same. However, in the high repetition rate version, recently introduced for Ti:Sapphire systems [92], The long lifetime of the gain is used in conjunction with CW pumping. At 10 W CW pumping with a Nd:YAG and a ~ 2 μs upper state lifetime of the KCl crystal, 20 μJ of energy may be stored in the gain medium for extraction. Even if only 10% of the energy is extracted, the amplified pulse would have 2 μJ of energy, certainly enough for continuum generation. Since the upper state lifetime is the only limitation on the repetition rate ($f < 1/2\pi\tau \approx 80$ kHz), a repetition rate of 20-50 kHz could easily be achieved. At 2 μJ and 50 kHz the average power would be 100 mW, much more practical for pump-probe experiments and signal averaging.

4.2 The dynamic anisotropy measurement on the PI-SOA

It should perhaps not be surprising that the isotropy in the small-signal characteristics of a device, is not preserved in the large-signal regime. This is exactly what was observed in the experiment: a device that by design has polarization independent gain, acquires a polarization dependence, when the optical excitation is large. Even in the CW regime this anisotropy is present. This behavior would probably be less surprising in a standard SOA, which is highly polarization dependent in the linear or small-signal regime.

Since the electrons fill up the QW's in the conduction band, all the observed femtosecond dynamics are due to the holes. The holes are very different in character in the two different QW's in the device: they are heavy hole states with a light in-plane mass in the

compressive well, and light hole states with a heavy in-plane mass in the tensile well. The anisotropic response can be traced back to this distinction. Different polarization selection rules govern the interband transitions (long-time dynamics), and mass dependent scattering processes govern the intraband transitions (ultrafast dynamics). In particular, the LO phonon-hole scattering cross-section is mass dependent and leads to longer cooling times in the compressive well. The free-hole absorption cross-section is also mass dependent and lead to different heating in the 2 types of wells. Finally, since the initial states for the holes in the different wells are different, hole tunneling is negligible and IVBA may be different depending on the exciting polarization. This last effect may be the reason for the observed anisotropy.

The direct anisotropy measurement brings out the interwell coupling more clearly, and indicates an intermediate time constant that may be attributed to interwell hole transfer. The measured time constant is within a factor of 2 from previous measurements on structures based on the same materials. Finally, there is a residual long-time anisotropy, which did not decay in the experiment even when scanned out to 30 ps time delays. This agrees with theoretical predictions regarding the anisotropy in the CW saturation of PI-SOA's.

To confirm the long time constant would require a device similar to the present one, but with barriers at least 2 to 3 times wider. In this case previous measurements have shown a corresponding increase in interwell transfer time. Changing other parameters is difficult, since some of them are "coupled". For example, changing the strain alone would modify the interband transition energy, so to keep it fixed would lead to changing the well widths. In this case the energy change due to quantum size effects would compensate for the strain-modified bandgap.

Another check on the results presented here, would be checking the dynamic anisotropy in a device which does not have mixed wells. Although the longer cooling time has been observed in a device where all the wells were compressively strained with very similar parameters, the direct anisotropy measurement was not performed on that device. An interesting comparison would be the TM-TM results measured here, with a device containing all tensile wells with the same parameters. When pump and probe are both TM polarized the interband transitions are confined to the tensile wells only. A comparison to a device containing only tensile wells would therefore indicate the extent to which the compressive wells contribute to the TM-TM response in the PI-SOA.

The theory indicates that for every fixed time delay there is a linear polarization for the probe, such that the gain anisotropy is nulled out in the direct anisotropy measurement.

For this polarization only the induced birefringence is measured. It would be interesting to perform this experiment, however, it may require very fine control on the probe and reference beam polarizations.

As far as constructing a fast optical polarization switch (as has been demonstrated with standard SOA's), it may be limited. The reason for this is the residual anisotropy which was observed in the direct anisotropy measurement. This would limit the rejection ratio, since at long time delays there would be leakage of the wrong polarization. This is similar to the requirement that an all-optical switch should operate near the transparency point, so that there is no long time residual index change.

Chapter 5

Appendix

The appendix will describe a few approaches to realizing a 1.5 μm intersubband transition in a QW. The potentially large and fast nonlinearity could lead to a practical all-optical switching component. Some of the issues and constraints associated with all-optical switching are discussed. Three specific structures and their limitations are then described for attaining such an intersubband transition

5.1 Design of microstructures for 1.5 μm intersubband non-linearities

All-optical switching is desirable in optical communication systems just as all-optical amplification was desirable: it eliminated the need for converting the optical signal into an electrical one and then back to an optical one. Additionally, all-optical switches could be potentially much faster than any electrical switch. Two basic schemes for optical switches can be envisioned: 1) an absorptive ("resistive") switch - a pump pulse would induce transmission changes (in fact close to 100% transmission changes), letting the signal through or absorbing it. 2) a dispersive ("reactive") switch - a pump pulse would induce index changes in one arm of a Mach-Zehnder interferometer, not affecting the signal or changing its phase by π radians. Since the carrier frequency should not be changed in the switching process, this implies a degenerate $\chi^{(3)}$ process: either nonlinear absorption (e.g., two-photon absorption) or nonlinear index (e.g., Kerr effect).

The constraints on these switches would be as follows: 1) The nonlinearity should be large enough, such that the switching energy required is not too large or alternatively the interaction length is not too large. Given $\chi^{(3)}$ at the frequency of interest will impose a lower limit on the product of pump peak power and interaction length (which in the case of a waveguiding device will be the device length). 2) The switching speed should be high enough, i.e., a fast recovering nonlinearity. The induced change in absorption or index should not persist longer than ~ 1 ps. This rules out any interband absorptive nonlinearity, which creates carriers that stay around for a time on the order of a radiative recombination time. It also implies a short pump pulse - shorter than the nonlinearity recovery time. 3)

The linear loss should be minimal so that in the case of no pump pulse the signal does not degrade. In fact, this imposes a constraint on the device length, namely it should not be much longer than one linear absorption length.

Finally, it should be noted that below-band dispersive switches have an advantage over the absorptive switches: they do not absorb the pump, and the constraints imposed by heat dissipation are much more relaxed. Potentially, dispersive switches operating below band could therefore go to higher repetition rates. It should be remembered that going away from resonances does reduce losses and absorption, however it also reduces the nonlinearity, which is enhanced closer to resonances of the material (such as the bandgap in semiconductors). Based on the above, a convenient figure of merit for such an optical switch could be defined as , where α is the linear absorption and τ is the speed of the switch or the recovery time of the nonlinearity.

To quantify some of these statements we note that , for example, in an index switch we are looking for a nonlinear phase shift of at least π radians:

$$\phi_{NL} = \frac{2\pi}{\lambda} n_2 I L \sim \pi$$

$$\frac{2}{\lambda} n_2 \frac{E}{\tau A_{\textit{eff}}} L \sim 1$$

(5.1)

where λ is the free-space wavelength, n_2 is the nonlinear index, I is the peak intensity, L is the interaction length, E is the pump pulse energy, τ is the pump pulsewidth and $A_{\textit{eff}}$ is the effective cross-sectional area of interaction. We now assume a waveguide structure so that L is the device length and we fix it at one linear absorption depth (if it is any longer the signal is seriously degraded or completely lost), i.e., $L = 1/\alpha$:

$$\frac{2}{\lambda} \frac{n_2}{\alpha\tau} \frac{E}{A_{\textit{eff}}} \sim 1$$

(5.2)

Since n_2 is proportional to $\text{Re}\{\chi^{(3)}\}$ and the pump pulsewidth is on the order of the speed of the nonlinearity (or faster), $n_2/\alpha\tau$ may be identified as the figure of merit defined earlier. $E/A_{\textit{eff}}$ is the energy fluence in the device, which should be at least on the order of the saturation fluence to utilize the nonlinearity effectively and we replace the energy fluence with the saturation fluence to get a lower limit:

$$\frac{2}{\lambda}\frac{n_2}{\alpha\tau}\frac{\hbar\omega}{\sigma} = \frac{2hc}{\lambda^2\sigma}\frac{n_2}{\alpha\tau} \sim 1 \qquad (5.3)$$

Here h is Planck's constant (and $\hbar$ is Planck's constant divided by 2π), c is the speed of light and σ is the transition cross-section (note that $\hbar\omega/\sigma\lambda$ can be viewed as a lower limit on the required energy density). Obviously, if higher pump energy will relax the constraints on the figure of merit. However, it should be remembered that increasing the energy will constrain the repetition rate of the system. This analysis applies to absorptive switches with the nonlinear absorption coefficient replacing $(2\pi/\lambda)n_2$ or equivalently $\text{Im}\{\chi^{(3)}\}$ replacing $\text{Re}\{\chi^{(3)}\}$.

5.1.1 Intersubband nonlinearities - advantages

It has been known for some time that quantum size effects tend to increase the nonlinear response in semiconductors [93] [94] and devices based on these enhanced nonlinearities have been demonstrated [95]. By going to lower dimensional microstructures (quantum wells, quantum wires and quantum dots), the wavefunctions of the bound carriers become localized in space. The increased overlap of the wavefunctions and 2D density of states leads to large dipole moments or oscillator strengths The oscillator strength is defined as [96]:

$$f = \frac{2m^*\omega|\langle k|\hat{\varepsilon}\bullet\vec{r}|i\rangle|^2}{\hbar} = \frac{2|\langle k|\hat{\varepsilon}\bullet\vec{p}|i\rangle|^2}{m^*\hbar\omega} \qquad (5.4)$$

where m^* is the effective mass, ω is the transition frequency, $\hbar$ is Planck's constant divided by 2π, $\langle k|\hat{\varepsilon}\bullet\vec{r}|i\rangle$ is the position matrix element between levels i and k and $\langle k|\hat{\varepsilon}\bullet\vec{p}|i\rangle$ is the corresponding momentum matrix element with $\hat{\varepsilon}$ the unit vector in the direction of the polarization. The position matrix element is proportional to the dipole moment (through the electric charge e).

In QW's under the envelope approximation, the allowed transitions are either interband or intraband transitions. In the first case (to lowest order) the allowed transitions are between states with the same quantum number in different bands (e.g., between the first heavy hole level and the first conduction level). Intraband transitions, better known as intersubband transitions, are between states with different parity within the same band (e.g., first conduction level to second conduction level).

106

The first observation of intersubband transitions was in GaAs QW's at 152 meV and 121 meV for a 65 Å and 82 Å well, respectively [97]. Since then a wealth of experiments have been reported on intersubband transitions for detectors [98] and nonlinearities such as SHG [99], four wave mixing [100], phase conjugation [101] and the optical Kerr effect [102]. Most of these experiments were performed around 10 μm and only recently has the wavelength range been extended first to around 4 μm [103] and then to around 2 μm [104]. The most spectacular result of recent years, involving intersubband transitions, is the quantum cascade laser [105]: a semiconductor laser based on intersubband transitions (the lasing transition takes place between subbands).

To get a better understanding of intersubband transitions some of their characteristics are now examined. It is desirable to use the 1→2 transition, since it results in the largest oscillator strength. This can be seen by comparing the oscillator strength of a 1→2 and a 1→m (m even). Transitions originating from higher subbands are usually not of practical interest. To get a simple analytic expression for the oscillator strength we follow ref. 97 and use the infinite well approximation. For an infinite well of width L the normalized wavefunctions are given by:

$$|1\rangle = \sqrt{\frac{2}{L}} \cos\left(\frac{\pi x}{L}\right)$$

$$|m\rangle = \sqrt{\frac{2}{L}} \sin\left(\frac{m\pi x}{L}\right)$$

(5.5)

To compute the momentum matrix element we use $p \to (\hbar/i)\partial/\partial x$ (here $i = \sqrt{-1}$). The result of the integration yields for the momentum matrix element:

$$\langle m|p|1\rangle = \frac{2\hbar}{iL} \frac{2m}{m^2 - 1}$$

(5.6)

this result can now be used to compute the oscillator strength to give:

$$f = \frac{2}{m^* \hbar \omega}\left(\frac{2\hbar}{L}\right)^2\left(\frac{2m}{m^2-1}\right)^2 = \frac{2}{m^*}\left(\frac{2\hbar}{L}\right)^2\left(\frac{2m}{m^2-1}\right)^2 \frac{2m^* L^2}{\hbar^2\pi^2\left(m^2-1\right)}$$

$$= \frac{64}{\pi^2}\frac{m^2}{\left(m^2-1\right)^3}$$

(5.7)

where we used the fact that $\hbar\omega$ is exactly the energy separation E_m-E_l. The oscillator strengths for the 1→2 transition and the 1→4 transition are:

$$f_{12} = \frac{64}{\pi^2}\frac{4}{27}$$
$$f_{14} = \frac{64}{\pi^2}\frac{16}{3375}$$

(5.8)

the ratio of these two oscillator strengths is ~31 (in general, for $m \geq 4$ the oscillator strength scales as m^{-4}). Since the nonlinearity scales with the oscillator strength squared, going from a 1→2 transition to a 1→4 transition means a decrease of almost 3 orders of magnitude in nonlinearity. It should also be pointed out f_{lm} obeys a sum rule:

$$\sum_{i=1}^{\infty} f_{1(2i-1)} = 1$$

(5.9)

It can now be appreciated why 1→2 intersubband transitions are important: since $f_{12} \approx 0.96$ it contains 96% of the total oscillator strength available to transitions originating in the first subband (by comparison f_{14} contains only 3%).

Additionally, since the curvature of the subbands is similar (at least for small energy separations), the resonant transition is a sharp one (compared to interband transitions): all participating carriers have approximately the same transition energy. This is why an intersubband system is very similar to an atomic two-level system. Both the large oscillator strength per carrier (discussed above) and the fact that all transitions are the same, leads to a "concentration" of the oscillator strength and very large optical effects.

A final note on intersubband transitions, is that to lowest order in the envelope approximation they are strictly forbidden for TE polarized light (polarization in the layer of the QW), as can be seen from the matrix element. This is an advantage for 1.5 μm light, since waveguiding TE as well as TM at this wavelength is not a problem. This is in contrast to 10.6 μm light, which required complicated zigzag geometries to achieve reasonable interaction length (see e.g., ref. 101).

5.1.2 Deep well requirement for 1.5 μm transitions

As mentioned earlier, the first intersubband demonstrations were shown for relatively small energy transitions, that can be probed with CO_2 lasers at 10.6 μm (corresponding to ~120 meV). QW's with energy separations of this magnitude are easily fabricated. However, 1.5 μm corresponds to an energy separation of ~830 meV and finding material combinations that will yield QW's which are about 1 eV "deep", is a challenging problem. Since the well is so deep it will tend to support many bound states and the basic transition might occur between the first and fourth or sixth level, instead of a first to second level transition. This leads to the requirement of very narrow wells, that support only 2 or 3 bound states.

Another aspect that needs to be considered in these widely separated subbands, is the departure from parabolic bands for the high-lying subbands. In other words strong nonparabolicity modifies the effective mass of the conduction band carriers. For intersubband transitions in the valence band the situation is even worse because of serious band mixing effects between the different valence bands, leading also to strong modifications of the band dispersion. In both cases the attractive feature of having the equivalent of an atomic two-level system is lost, because the subbands are no longer "parallel" and the intersubband transition is no longer a sharp one.

5.1.3 1→2 intersubband transitions

Recently a few approaches have been explored toward achieving the goal of an intersubband transition at 1.5 μm, one of these was verified experimentally [106] (after successfully demonstrating a 1.798 μm intersubband transition in a similar structure [107]. All of these structures would be designed as absorptive switches based on saturation: the pump pulse excites carriers from the doped lower level to the upper level, bleaching the absorption until the excited carriers relaxed back through various scattering mechanisms. The only 1.5 μm intersubband transition to be verified experimentally (by linear absorption measurements), is based on a structure containing several materials, engineered such that a well is formed between two very "high" and thin barriers. To get a 1→2 transition, the well was only 3 monolayers thick. The second subband strictly speaking is no longer a bound state and has a finite probability to tunnel through the thin barriers. The relaxation rate of the excited carriers has to be higher than the escape rate due to tunneling, to make this a useful high-speed switching device (because otherwise the excited carriers will be lost, and may take a long time to replenish the well). Another point of interest was the fact that TE polarized light was also absorbed in the intersubband transition, slightly shifted in

energy from the TM absorption. The reason for this is that the envelope approximation is not a good one in this case: the total wavefunctions of the first and second subbands belong to different symmetry groups [108]. The first subband has an S-like wavefunction (as in bulk), but the second subband is P-like (similar to the bulk valence bands). In this case both TE and TM transitions are allowed. Local crystal deformations and strain split the second subband, accounting for the energy separation between the 2 transitions.

5.1.4 1→4 intersubband transitions

Two other approaches to a 1.5 μm intersubband transitions are based on 1→4 transitions. Although the nonlinearity is reduced significantly (as discussed above), it may still be substantial enough to be useful. The first approach is based on a GaAs QW with ZnSe barriers and relies on recent advances in crystal growth that allow the growth of III-V materials on II-VI materials. The heavy hole well depth in this system is ~ 0.96 eV. The second approach is based on a GaSb well with AlSb barriers. This system is attractive since it is well understood and there is a lot of experience in growing it. The conduction band well depth is ~ 1.2 eV.

5.1.5 ZnSe/GaAs hole transitions

There is a large difference in bandgap energies between GaAs and ZnSe (~ 1.25 eV) and most of it is in the valence band. However, it is not quite enough to support a 1→2 transition. As the well is made narrower the first subband moves up in energy, and before the separation between it and the second subband is ~ 0.8 eV, the second subband is no longer a bound state. This is the case for both heavy and light holes. However, a 1→4 transition is possible. It should be noted that there is also a large difference in dielectric constants between the two materials, which leads to charge sheets at the interfaces and modifies the optical properties of the system. These are also called dielectric QW's and have been investigated theoretically [109].

A k•p calculation was performed to investigate the dispersion of these subbands, for a 1→4 heavy hole transition of ~ 1.49 μm in a 33 Å GaAs QW with ZnSe barriers. Although this calculation ignores the effects of the split-off band (treating it as parabolic and decoupled from the other two valence band), which is a bad approximation at least for the higher subbands, it still gives a qualitative picture of the band structure. The parameters used for the calculation are given in Table 5.1 and the results of the calculation are given in Figure 5.1. The calculation does not take into account strain and dielectric effects.

	Well	Barrier
Material	GaAs	ZnSe
Bandgap (eV)	1.424	2.67
VBO (%)	0.77	0.77
width (Å)	33	∞
Luttinger parameter γ_1	6.85	2.45
Luttinger parameter γ_2	2.1	0.61
Luttinger parameter γ_3	2.9	1

Table 5.1:   Parameters used for the k•p calculation of the GaAs/ZnSe valence band structure

The results show significant band mixing and warping, so that intersubband transitions would definitely have a large frequency spread (in contrast to small-energy separated subbands in the conduction band) and the oscillator strength is no longer strongly concentrated in a single transition. In fact, from these results it is doubtful that 1→4 will be favored, because of the inverted curvature (negative mass) of the fourth subband at k=0. To confirm these results a more rigorous band structure calculation must be performed, to include the split-off band (and maybe not using the envelope function approximation).

5.1.6 GaSb/AlSb electron transitions

The last approach towards a 1.5 μm intersubband transition involves a GaSb QW with AlSb barriers (this system has been used for intersubband transitions at 15 μm [110]). At the Γ point (Brillouin zone center) the discontinuity in the conduction band is ~ 1.2 eV. At first sight this might seem perfect to achieve a 1→2 transition. However, the serious problem with GaSb is that becomes indirect for well widths less than ~ 40 Å [111]: under quantum confinement, with decreasing well width, the first subband in the Γ valley moves up "faster" than the corresponding one in the L valley (because of the smaller effective mass in the Γ valley), and around a well width of 40 Å the first subbands in both valleys are at the same energy. Beyond that point there is a much shallower L valley QW, since the AlSb L valley gap is much smaller than the Γ valley gap. This means that the QW has to be wider than 40 Å, especially considering the fact that it needs to be doped, and we want to

111
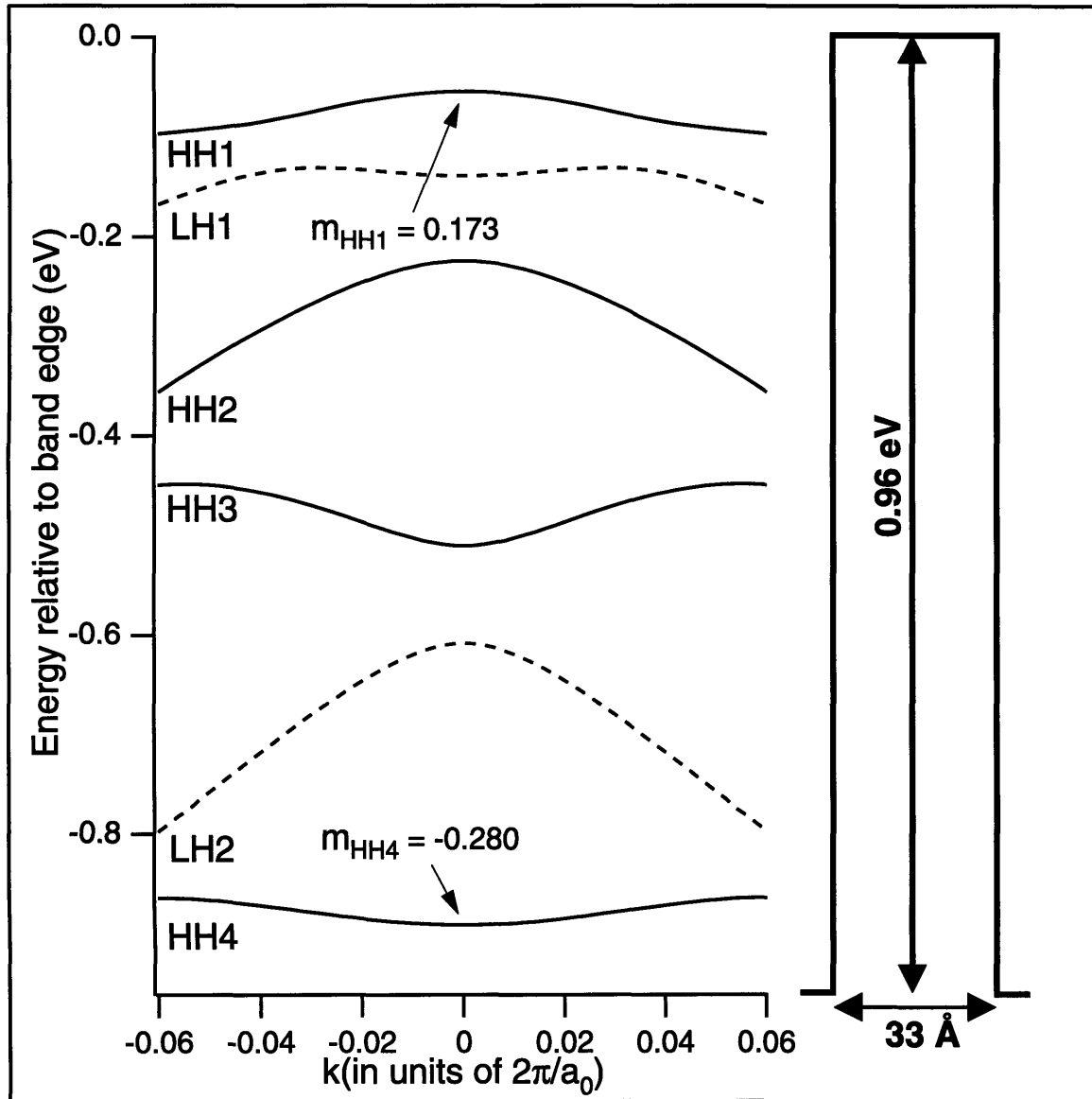
Figure 5.1:   Valence band structure of the GaAs QW with ZnSe barriers. The transition energy between the first and fourth heavy hole subbands corresponds to 1.49 μm.

avoid spill-over from the Γ valley to the L valley (with the higher density of states). However, 40 Å is still too wide to achieve a 1.5 μm transition. The problem is even more severe when the effects of nonparabolicity are included. Since the upper subband will be ~ 1 eV above the bottom of the conduction band, the energy dependence of the effective mass cannot be ignored.

This again leaves the 1→4 transition. To calculate the subband energies and curvatures at $k=0$, the finite potential well problem was solved, including the well depth modification due to strain and the energy dependence of the effective mass. This nonparabolicity is based on an empirical relationship between well width and effective mass [112]. Based on ref. 112 the unstrained well depth was taken as 1.17 eV. The strain in the barrier was ignored and the strain in the well was 0.65%, leading to a hydrostatic shift of the bandgap of 108 meV. If it is assumed that all of this shift is in the conduction band, the total well depth becomes 1.28 eV (the other standard ratio is 2/3 of the shift in the conduction band for a total well depth of 1.24 eV). The AlSb effective mass was taken as $0.11m_0$ and the GaSb bulk effective mass was $0.047m_0$. Based on the data in ref. 112, a curve of effective mass vs. energy above the bottom of the well was calculated and is shown in Figure 5.2.
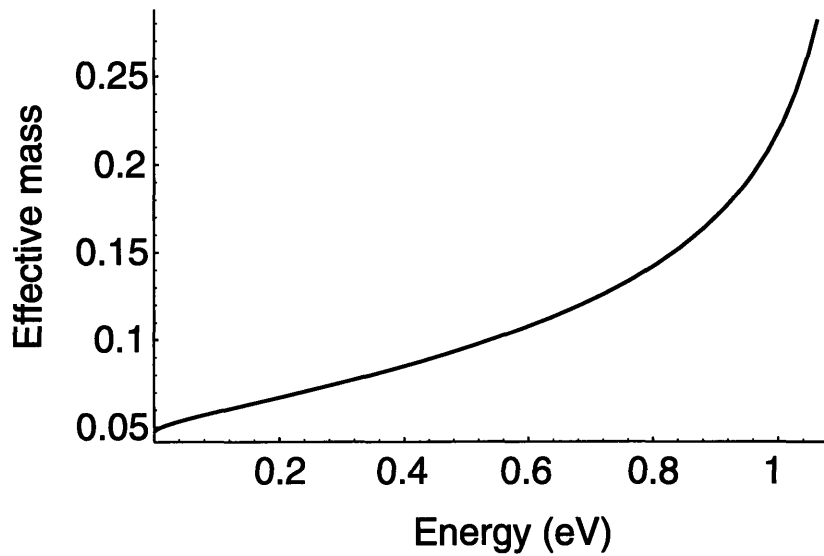
Figure 5.2:   Energy dependence of effective mass in the GaSb conduction band

Using all of these parameters shows that a 1.52 μm 1→4 transition can be achieved in a 50 Å QW. It should be pointed out that it is not clear if the empirical relation for the effective mass is accurate at very high energies, so the mass may not be as high as implied by the above figure. However, the mass in the fourth subband may be about 3 times higher than in the first subband. So in this case too the sharp resonance and concentrated oscillator strength typical of small-energy intersubband transitions, may be absent.

On the other hand, another nonlinearity may be used: the nonparabolicity nonlinearity. This nonlinearity is a well-known free-carrier nonlinearity [113] and is based on the fact

that after excitation the mass changes leading to a change in the plasma frequency, which in turn leads to a change in the dielectric constant or refractive index. This modified dielectric constant will last as long as the carriers are in the upper subband. It should be noted that exploiting the subband structure as an optical nonlinearity has been demonstrated in AlInSb/InSb [114]. Another enhancement in the nonlinearity is due to the photon energy being close to the bandgap energy. The enhancement factor scales like [113]:

$$\left(\frac{E_g^2}{E_g^2 - (\hbar\omega)^2} \right)^2 \tag{5.10}$$

which means that for light detuned about 75 nm (or 40 meV) from the band edge, an enhancement factor of 100 is possible. As always this enhancement cannot be pushed too far or else interband transitions will start to generate carriers in the conduction band. Finally, it should be noted that there is no problem in growing a large number of such wells and get an increase in signal, this is a big advantage over the first two approaches.

Based on some of the potential advantages of this system, it seems to be a promising candidate for a 1.5 μm intersubband transition, eventhough it would probably be a 1→4 transition. There may be a possibility of tailoring a 1→2 transition by making a relatively wide well surrounded by GaSb/AlSb superlattices engineered, such that only two bound states of the total system would exist. This approach needs to be investigated further.

Bibliography

[1]   G. P. Agrawal, *Nonlinear Fiber Optics*. Academic Press; San Diego, 1989.

[2]   P. N. Butcher and D. Cotter, *The Elements of Nonlinear Optics*. Cambridge University Press; Cambridge, 1991.

[3]   A. A. M. Saleh, "Optical WDM technology for networking and switching applications", in *Proceedings of OFC '92*, paper ThC1, 1992.

[4]   R. R. Alfano, ed., *The Supercontinuum Laser Source*. Springer Verlag; New York, 1989.

[5]   J. Mark, L. Y. Liu, K. L. Hall, H. A. Haus, and E. P. Ippen, "Femtosecond pulse generation in a laser with a nonlinear external resonator", *Opt. Lett.*, vol. 14, pp. 48-50, 1989.

[6]   P. N. Kean, X. Zhu, D. W. Crust, R. S. Grant, N. Langford, and W. Sibbett, "Enhanced mode-locking of color-center lasers", *Opt. Lett.*, vol. 14, pp. 39-41, 1989.

[7]   I. N. Duling, "Subpicosecond all-fibre erbium lasers", *Electron. Lett.*, vol. 27, pp. 544-545, 1991.

[8]   A. Sennaroglu, C. R. Pollock, and H. Nathel, "Continuous-wave self-mode-locked operation of a femtosecond Cr^{4+}:YAG laser", *Opt. Lett.*, vol. 19, pp. 390-392, 1994.

[9]   P. E. Powers, R. J. Ellingson, W. S. Pelouch, and C. L. Tang, "Recent advances of the Ti:Sapphire-pumped high-repetition-rate femtosecond optical parametric oscillator", *J. Opt. Soc. Am. B*, vol. 10, pp. 2162-2167, 1993.

[10]   R. J. Mears, L. Reekie, I. M. Jauncey, and D. N. Payne, "Low noise erbium-doped fibre amplifier operating at 1.54 µm", *Electron. Lett.*, vol. 23, p. 1026, 1987.

[11]   E. Desurvire, J. Simpson, and P. C. Becker, "High-gain erbium-doped traveling-wave fiber amplifier", *Opt. Lett.*, vol. 12, pp. 888-890, 1987.

[12]   K. Tamura, L. E. Nelson, H. A. Haus, and E. P. Ippen, "Soliton versus nonsoliton operation of fiber ring lasers", *Appl. Phys. Lett.*, vol. 64, pp. 149-151, 1994.

[13]   M. E. Fermann, K. Sugden, and I. Bennion, "Generation of 10 nJ picosecond pulses from a modelocked fibre laser", *Electron. Lett.*, vol. 31, pp. 194-195, 1995.

[14] K. Tamura, C. R. Doerr, L. E. Nelson, H. A. Haus, and E. P. Ippen, "Technique for obtaining high-energy ultrashort pulses from an additive-pulse mode-locked erbium-doped fiber ring laser", *Opt. Lett.*, vol. 19, pp. 46-48, 1994.

[15] K. M. Dzurko, R. A. Parke, J. S. Osinski, S. O'brien, J.-M. Verdiell, R. J. Lang, and D. F. Welch, "Operating Characteristics of High-Power, Diffraction-Limited MOPAs", in *LEOS '94 Conference Proceedings*, vol. 2, pp. 397-398, 1994.

[16] J. S. Osinski, K. M. Dzurko, J. S. Major, Jr., R. A. Parke, and D. F. Welch, "Electronically tunable 1-W CW, near-diffraction-limited monolithic flared amplifier-master oscillator power amplifier (MFA-MOPA)", *IEEE Photon. Technol. Lett.*, vol. 6, pp. 885-887, 1994.

[17] R. L. Fork, "Optical frequency filter for ultrashort pulses", *Opt. Lett.*, vol. 11, pp. 629-631, 1986

[18] E. D. Palik, ed., *Handbook of Optical Constants of Solids*, Academic Press; San Diego, 1985.

[19] R. L. Fork, C. H. Brito Cruz, P. C. Becker, and C. V. Shank, "Compression of optical pulses to six femtoseconds by using cubic phase compensation", *Opt. Lett.*, vol. 12, pp. 483-485, 1987.

[20] D. Von der Linde, "Characterization of the noise in continuously operating modelocked lasers", *Appl. Phys. B*, vol. 39, pp. 201-217, 1986.

[21] U. Keller, K. D. Li, M. Rodwell, and D. M. Bloom, "Noise characterization of femtosecond fiber Raman soliton lasers", *IEEE J. Quantum Electron.*, vol. 25, pp. 280-288, 1989.

[22] A. Finch, X. Zhu, P. N. Kean, and W. Sibbett, "Noise characterization of mode-locked color-center laser sources", *IEEE J. Quantum Electron.*, vol. 26, pp. 1115-1123, 1990.

[23] A. M. Weiner, "Effect of group velocity mismatch on the measurement of ultrashort optical pulses via second harmonic generation", *IEEE J. Quantum Electron.*, vol. 19, pp. 1276-1283, 1986.

[24] G. Sucha, S. R. Bolton, and D. S. Chemla, "Generation of high-power femtosecond pulses near 1.5 μm using a color-center laser system", *IEEE J. Quantum Electron.*, vol. 28, pp. 2163-2175, 1992.

[25] G. Sucha and D. S. Chemla, "Kilohertz-rate continuum generation by amplification of femtosecond pulses near 1.5 μm", *Opt. Lett.*, vol. 16, 1177-1179, 1991.

[26] E. Georgiou, J. F. Pinto, and C. R. Pollock, "Optical properties and formation of oxygen-perturbed F_2^+ color center in NaCl", *Phys. Rev. B*, vol. 35, pp. 7636-7645, 1987.

[27] G. Lenz, K. Tamura, H. A. Haus, and E. P. Ippen, "All-solid-state femtosecond source at 1.55 μm", *Opt. Lett.*, vol. 20, pp. 1289-1291, 1995.

116

[28] J. T. Manassah, M. A. Mustafa, R. R. Alfano, and P. P. Ho, "Spectral extent and pulse shape of the supercontinuum for ultrashort laser pulse", *IEEE J. Quantum Electron.*, vol. 22, pp. 197-204, 1986.

[29] G. Yang and Y. R. Shen, "Spectral broadening of ultrashort pulses in a nonlinear medium", *Opt. Lett.*, vol. 9, pp. 510-512, 1984.

[30] Y. R. Shen and M. M. T. Loy, "Theoretical interpretation of small-scale filaments of light originating from moving focal spots", *Phys. Rev. A*, vol. 3, pp. 2099-2105, 1971.

[31] M. M. T. Loy and Y. R. Shen, "Study of self-focusing and small-scale filaments of light in nonlinear media", *IEEE J. Quantum Electron.*, vol. 9, pp. 409-422, 1973.

[32] M. Sheik-Bahae, D. C. Hutchings, D. J. Hagan, and E. W. Van Stryland, "Dispersion of bound electronic nonlinear refraction in solids", *IEEE J. Quantum Electron.*, vol. 27, pp. 1296-1309, 1991.

[33] B. S. Wherrett, "Scaling rules for multiphoton interband absorption in semiconductors", *J. Opt. Soc. Am. B*, vol. 1, pp. 67-72, 1984.

[34] W. J. Tomlinson, R. H. Stolen, and C. V. Shank, "Compression of optical pulses chirped by self-phase modulation in fibres", *J. Opt. Soc. Am. B*, vol. 1, pp. 139-149, 1984.

[35] O. E. Martinez, "Matrix formalism for pulse compressors", *IEEE J. Quantum Electron.*, vol. 24, pp. 2530-2536, 1988.

[36] K. L. Hall, G. Lenz, E. P. Ippen, and G. Raybon, "Heterodyne pump-probe technique for time-domain studies of optical nonlinearities in waveguides", *Opt. Lett.*, vol. 17, pp. 874-876, 1992.

[37] L. F. Mollenauer, "Color center lasers", in *Laser Handbook*, pp. 143-228, Elsevier Science Publishers B.V., 1985.

[38] J. Mark, L. Y. Liu, K. L. Hall, H. A. Haus, and E. P. Ippen, "Femtosecond pulse generation in a laser with a nonlinear external resonator", *Opt. Lett.*, vol. 14, pp. 48-50, 1989.

[39] P. N. Kean, R. S. Grant, X. Zhu, D. W. Crust, D. Burns, and W. Sibbett, "Enhanced mode-locking of colour centre lasers by coupled-cavity feedback control", in *Conference on Lasers and Electro-optics Technical Digest 1988*, p. 468, 1988.

[40] K. S. Kim, R. H. Stolen, W. A. Reed, and K. W. Quoi, "Measurement of the nonlinear index of silica-core and dispersion-shifted fiber", *Opt. Lett.*, vol. 19, pp. 257-259, 1994.

[41] F. M. Mitschke and L. F. Mollenauer, "Stabilizing the soliton laser", *IEEE J. Quantum Electron.*, vol. 22, pp. 2242-2250, 1986.

[42] K. Naganuma, G. Lenz, and E. P. Ippen, "Variable bandwidth birefringent filter for tunable femtosecond pulses", *IEEE J. Quantum Electron.*, vol. 28, pp. 2142-2150, 1992.

[43] K. L. Hall, "Femtosecond nonlinearities in InGaAsP diode lasers". MIT Doctoral Thesis, May 1993.

[44] H. M. Presby and C. A. Edwards, "Near 100% efficient fibre microlenses", *Electron. Lett.*, vol. 28, pp. 582-584, 1992.

[45] A. Mathur and P. D. Dapkus, "Polarization insensitive strained quantum well gain medium for lasers and optical amplifiers", *Appl. Phys. Lett.*, vol. 61, pp. 2845-2847, 1992.

[46] L. F. Tiemeijer, P. J. A. Thijs, T. Van Dongen, R. W. M. Slootweg, J. M. M. van der Heijden, J. J. M. Binsma, and M. P. C. M. Krijn, "Polarization insensitive multiple quantum well laser amplifiers for the 1300 nm window", *Appl. Phys. Lett.*, vol. 62, pp. 826-828, 1993.

[47] M. A. Newkirk, B. I. Miller, U. Koren, M. G. Young, M. Chien, R. M. Jopson, and C. A. Burrus, "1.5 μm Multiquantum-Well Semiconductor Optical Amplifier with Tensile and Compressively Strained Wells for Polarization-Independent Gain", *IEEE Photon. Technol. Lett.*, vol. 5, 406-408, 1993.

[48] A. Godefroy, A. Le Corre, F. Clérot, S. Salaün, S. Loualiche, J. C. Simon, L. Henry, C. Vaudry, J. C. Kéromnès, G. Joulié, and P. Lamouler, "1.55 μm Polarization-Insensitive Optical Amplifier with Strain-Balanced Superlattice Active Layer", *IEEE Photon. Technol. Lett.*, vol. 7, 473-475, 1995.

[49] E. O. Kane, "Band structure of indium antimonide", *J. Phys. Chem. Solids*, vol. 1, pp. 249-261, 1957.

[50] M. Yamanishi and I. Suemune, "Comment on Polarization Dependent Momentum Matrix Elements in Quantum Well Lasers", *Japan J. Appl. Phys.*, vol. 23, pp. L35-L36, 1984.

[51] C. S. Chang and S. L. Chuang, "Universal curves for optical-matrix elements of strained quantum wells", *Appl. Phys. Lett.*, vol. 66, pp. 795-797, 1995.

[52] J. M. Wiesenfeld, S. Weiss, D. Botkin, and D. S. Chemla, "Carrier transport effects and dynamics in multiple quantum well optical amplifiers", *Opt. And Quantum Electron.*, vol. 26, pp. S731-S756, 1994.

[53] J. M. Wiesenfeld, private communication.

[54] J. M. Luttinger, "Quantum Theory of Cyclotron Resonance in Semiconductors: General Theory", *Phys. Rev.*, vol. 102, pp. 1030-1041, 1956.

[55] G. Bastard, *Wave Mechanics Applied to Semiconductor Heterostructures*. Halsted Press; New York, 1988.

[56] B. K. Ridley, "The in-plane effective mass in strained-layer quantum wells", *J. Appl. Phys.*, vol. 68, pp. 4667-4673, 1990.

[57] J. Lee and M. O. Vassell, "Effects of uniaxial stress on hole subbands in semiconductor quantum wells. I. Theory", *Phys. Rev. B.*, vol. 37, pp. 8855-8860, 1988.

[58] S. L. Chuang, "Efficient band-structure calculations of strained quantum wells", *Phys. Rev. B*, vol. 43, pp. 9649-9661, 1991.

[59] L. C. Andreani, A. Pasquarello, and F. Bassani, "Hole subbands in strained GaAs-$Ga_{1-x}Al_xAs$ quantum wells: Exact solutions of the effective-mass equation", *Phys Rev. B*, vol. 36, pp. 5887-5893, 1987.

[60] D. Gershoni, C. H. Henry, and G. A. Baraff, "Calculating the Optical Properties of Multidimensional Heterostructures: Application to the modeling of Quaternary Quantum Well Lasers", *IEEE J. Quantum Electron.*, vol. 29, pp. 2433-2450, 1993.

[61] M. Tinkham, *Group Theory and Quantum Mechanics*. McGraw-Hill; New York, 1964.

[62] G. E. Pikus and G. L. Bir, "Effect of Deformation on the Hole Energy Spectrum of Germanium and Silicon", *Fiz. Tverd. Tela*, vol. 1, pp. 1642-1658, 1959 [Sov. Phys. Solid State, vol. 1, 1502-1517, 1960].

[63] T. P. Pearsall, ed., *Strained-Layer Superlattices: Physics*, Semiconductors and Semimetals vol. 32. Academic Press; San Diego, 1990.

[64] C. Y. Chao and S. L. Chuang, "Spin-orbit-coupling effects on the valence-band structure of strained semiconductor quantum wells", *Phys. Rev. B*, vol. 46, pp. 4110-4122, 1992.

[65] T. B. Bahder, "Eight-band k•p model of strained zinc-blende crystals", *Phys. Rev. B*, vol. 41, pp. 11992-12001, 1990.

[66] *Numerical Data and Functional Relationships in Science and Technology*, Edited by K.-H. Hellwege, Landolt-Börnstein, New Series, vol. 17. Springer; Berlin, 1982.

[67] H. Kroemer, "Barrier control and measurements: Abrupt semiconductor heterojunctions", *J. Vac. Sci. Technol. B*, vol. 2, pp. 433-439, 1984.

[68] T. Ishikawa and J. E. Bowers, "Band lineup and in-plane effective mass of InGaAsP or InGaAlAs on InP strained-layer quantum well", *IEEE J. Quantum Electron.*, vol. 30, pp. 562-570, 1994.

[69] C. G. Van de Walle, "Band lineups and deformation potentials in the model-solid theory", *Phys. Rev. B*, vol. 39, pp. 1871-1883, 1989.

[70] R. Kersting, R. Schwedler, A. Kohl, K. Leo, and H. Kurz, "Ultrafast carrier dynamics in $In_{1-x}Ga_xAs/InP$ heterostructures", *Opt. Quantum Electron.*, vol. 26, pp. S705-S718, 1994.

[71] P. W. M. Blom, J. Claes, J. E. M. Haverkort, and J. H. Wolter, "Experimental and theoretical study of the carrier capture time", *Opt. And Quantum Electron.*, vol. 26, pp. S667-S677, 1994.

[72] J. Zhou, N. Park, K. J. Vahala, M. A. Newkirk, and B. I. Miller, "Study of interwell carrier transport by terahertz four-wave mixing in an optical amplifier with tensile and compressively strained quantum wells", *Appl. Phys. Lett.*, vol. 65, pp. 1897-1899, 1994.

[73] S. Dubovitsky, W. H. Steier, A. Mathus, and P. D. Dapkus, "Gain Saturation Properties of a Semiconductor Gain Medium with Tensile and Compressive Strain Quantum Wells", *IEEE J. Quantum Electron.*, vol. 30, pp. 380-391, 1994.

[74] P. D. Roberts, G. T. Kennedy, W. Sibbett, D. A. O. Davies, M. A. Fisher, M. J. Adams, and J. F. Allen, "Low power-polarization switching in InGaAsP semiconductor optical amplifiers", in *Conference on Lasers and Electro-optics Technical Digest 1995*, p. 377, 1995.

[75] K. L. Hall, A. M. Darwish, E. P. Ippen, U. Koren, and G. Raybon, "Femtosecond index nonlinearities in InGaAsP optical amplifiers", *Appl. Phys. Lett.*, vol. 62, pp. 1320-1322, 1993.

[76] E. P. Ippen and C. V. Shank, "Techniques for measurement", in *Ultrashort Light Pulses, Picosecond Techniques and Applications (S. L. Shapiro, ed.)*, Springer: New York, 1977.

[77] Z. Vardeny and J. Tauc, "Picosecond coherence coupling in the pump and probe technique", *Opt. Comm.*, vol. 39, pp. 396-400, 1981.

[78] K. L. Hall, G. Lenz, E. P. Ippen, U. Koren, and G. Raybon, "Carrier heating and spectral hole burning in strained-layer quantum-well laser amplifiers at 1.5 μm", *Appl. Phys. Lett.*, vol. 61, pp. 2512-2514, 1992.

[79] J. Mørk and A. Mecozzi, "Response function for gain and refractive index dynamics in active semiconductor waveguides", vol. 65, pp. 1736-1738, 1994.

[80] C. T. Hultgren and E. P. Ippen, "Ultrafast refractive index dynamics in AlGaAs diode laser amplifiers", *Appl. Phys. Lett.*, vol. 59, pp. 635-637, 1991.

[81] D. C. Hutchings, M. Sheik-Bahae, D. J. Hagan, and E. W. van Stryland, "Kramers-Kronig relations in nonlinear optics", *Opt. And Quantum Electron.*, vol. 24, pp. 1-30, 1992.

[82] K. L. Hall, G. Lenz, and E. P. Ippen, "Femtosecond time-domain measurements of group velocity dispersion in diode lasers at 1.5 μm", *J. Lightwave Technol.*, vol. 10, pp. 616-619, 1992.

[83] B. K. Ridley, *Quantum processes in semiconductors*. Second edition. Clarendon Press; Oxford, 1988.

[84] D. Ahn, "Calculations of hole-phonon scattering in strained-layer quantum wells", *J. Appl. Phys.*, vol. 78, pp. 4505-4509, 1995.

120

[85] C. T. Hultgren, "Femtosecond nonlinearities in AlGaAs diode laser amplifiers". MIT Doctoral Thesis, July 1994.

[86] A. R. Adams, M. Asada, Y. Suematsu, and S. Arai, "The temperature dependence of the efficiency and threshold current of $In_{1-x}Ga_xAs_yP_{1-y}$ lasers related to intervalence band absorption", *Japan. J. Appl. Phys.*, vol. 19, pp. L621-L624, 1980.

[87] C. H. Henry, R. A. Logan, F. R. Merritt, and J. P. Luongo, "The effect of intervalence band absorption on the thermal behavior of InGaAsP lasers", *IEEE J. Quantum Electron.*, vol. 19, pp. 947-952, 1983

[88] C. V. Shank and E. P. Ippen, "Anisotropic absorption saturation with picosecond pulses", *Appl. Phys. Lett.*, vol. 26, pp. 62-63, 1975.

[89] E. A. De Souza, M. C. Nuss, W. H. Knox, and D. A. B. Miller, "Wavelength division multiplexing with femtosecond pulses", *Opt. Lett.*, vol. 20, pp. 1166-1168, 1995.

[90] S. LePage, K. L. Hall, G. Lenz, and E. P. Ippen, "Widely tunable source generating subpicosecond pulses at 1550 nm", in *SPIE Photonics East Proceedings*. Philadelphia, PA, 1995 (to be published).

[91] B. E. Lemoff and C. P. J. Barty, "Cubic-phase-free dispersion compensation in solid-state ultrashort-pulse lasers", *Opt. Lett.*, vol. 18, pp. 57-59, 1993.

[92] T. B. Norris, "Femtosecond pulse amplification at 250 kHz with a Ti:Sapphire regenerative amplifier and application to continuum generation", *Opt. Lett.*, vol. 17, pp. 1009-1011, 1992.

[93] D. S. Chemla, "Nonlinear optics in quantum-confined structures", *Phys. Today*, vol. 46, pp. 46-52, 1993.

[94] S. Schmitt-Rink, D. S. Chemla, and D. A. B. Miller, "Linear and nonlinear optical properties of semiconductor quantum wells", *Adv. Phys.*, vol. 38, pp. 89-188, 1989.

[95] D. A. B. Miller, D. S. Chemla, T. C. Damen, A. C. Gossard, W. Wiegmann, T. Wood, and C. A. Burrus, "Novel hybrid optically bistable switch: the quantum well self-electro-optic effect device", *Appl. Phys. Lett.*, vol. 45, pp. 13-15, 1984.

[96] C. Weisbuch and B. Vinter, *Quantum Semiconductor Structures Fundamentals and Applications*. Academic Press; San Diego, 1991.

[97] L. C. West and S, J, Eglash, "First observation of an extremely large-dipole infrared transition within the conduction band of a GaAs quantum well", *Appl. Phys. Lett.*, vol. 46, pp. 1156-1158, 1985.

[98] B. F. Levine, K. K. Choi, C. G. Bethea, J. Walker, and R. J. Malik, "New 10 μm infrared detector using intersubband absorption in resonant tunneling GaAlAs superlattices", *Appl. Phys. Lett.*, vol. 50, pp. 1092-94, 1987.

[99]   M. M. Fejer, S. J. B. Yoo, R. L. Byer, A. Harwit, and J. S. Harris, Jr., "Observation of extremely large quadratic susceptibility at 9.6-10.8 μm in electric-field-biased AlGaAs quantum wells", *Phys. Rev. Lett.*, vol. 62, pp. 1041-1044, 1989.

[100] D. Walrod, S. Y. Auyang, P. A. Wolff, and M. Sugimoto, "Observation of third order optical nonlinearity due to intersubband transitions in AlGaAs/GaAs superlattices", *Appl. Phys. Lett.*, vol. 59, pp. 2932-2934, 1991.

[101] I. Gravé, M. Segev, and A. Yariv, "Observation of phase conjugation at 10.6 μm via intersubband third-order nonlinearities in a GaAs/AlGaAs multi-quantum-well structure", *Appl. Phys. Lett.*, vol. 60, pp. 2717-2719, 1992.

[102] M. Segev, I. Gravé, and A. Yariv, "Demonstration of the optical Kerr effect at 10.6 μm via intersubband nonlinearities in a multi-quantum well structure", *Appl. Phys. Lett.*, vol. 61, pp. 2403-2405, 1992.

[103] H. Asai and Y. Kawamura, "Intersubband absorption in $In_{0.53}Ga_{0.47}As/In_{0.52}Al_{0.48}As$ multiple quantum wells", *Phys. Rev. B*, vol. 43, pp. 4748-4759, 1991.

[104] L. H. Peng, J. H. Smet, T. P. E. Broekaert, and C. G. Fonstad, "Transverse electric and transverse magnetic polarization active intersubband transitions in narrow InGaAs quantum wells", *Appl. Phys. Lett.*, vol. 61, pp. 2078-2080, 1992.

[105] J. Faist, F. Capasso, D. L. Sivco, C. Sirtori, A. L. Hutchinson, and A. Y. Cho, "Quantum cascade laser", *Science*, vol. 264, pp. 553-556, 1994.

[106] J. H. Smet, L. H. Peng, Y. Hirayama, and C. G. Fonstad, "Electron intersubband transitions to 0.8 eV (1.55 μm) in InGaAs/AlAs single quantum wells", *Appl. Phys. Lett.*, vol. 64, pp. 986-987, 1994.

[107] Y. Hirayama, J. H. Smet, L. H. Peng, C. G. Fonstad, and E. P. Ippen, "Observation of 1.798 μm intersubband transition in InGaAs/AlAs pseudomorphic quantum well heterostructures", *Appl. Phys. Lett.*, vol. 63, pp. 1663-1665, 1993.

[108] L. H. Peng, J. H. Smet, T. P. E. Broekaert, and C. G. Fonstad, "Strain effects in the intersubband transitions of narrow InGaAs quantum wells", *Appl. Phys. Lett.*, vol. 62, pp. 2413-2415, 1993.

[109] M. Kumagai and T. Takagahara, "Excitonic and nonlinear-optical properties of dielectric quantum-well structures", *Phys. Rev. B*, vol. 40, pp. 12359-12381, 1989.

[110] L. A. Samoska, B. Brar, and H. Kroemer, "Strong far-infrared intersubband absorption under normal incidence in heavily n-type doped nonalloy GaSb-AlSb superlattices", *Appl. Phys. Lett.*, vol. 62, pp. 2539-2541, 1993.

[111] A. Forchel, U. Cebulla, G. Tränkle, H. Kroemer, S. Subbanna, and G. Griffiths, "Size-induced direct-to-indirect gap transition in GaSb/AlSb multiple quantum well structures", *Surf. Sci.*, vol. 174, pp. 143-147, 1986.

[112] U. Cebulla, G. Tränkle, U. Ziem, A. Forchel, G. Griffiths, H. Kroemer, and S. Subbanna, "Spectroscopic determination of the band discontinuity in GaSb/AlSb multiple-quantum-well structures", *Phys. Rev. B*, vol. 37, pp. 6278-6284, 1988.

[113] S. Y. Auyang and P. A. Wolff, "Free-carrier-induced third-order optical nonlinearities in semiconductors", *J. Opt. Soc. Am. B*, vol. 6, pp. 595-605, 1989.

[114] D. Walrod, S. Y. Auyang, P. A. Wolff, and T. Tsang, "Optical nonlinearities due to subband structures in $Al_{0.08}In_{0.92}Sb/InSb$ superlattices", *Appl. Phys. Lett.*, vol. 56, pp. 218-220, 1990.